Universidade Federal de Minas Gerais

Escola de Engenharia

Programa de Pós-Graduação em Engenharia Elétrica

Erick Matheus da Silveira Brito

Lifetime Evaluation of Photovoltaic Inverters with Capability of Reactive Power Support

Belo Horizonte
August, 2021.

Erick Matheus da Silveira Brito

Lifetime Evaluation of Photovoltaic Inverters with Capability of Reactive Power Support

Tese de doutorado submetida à banca examinadora designada pelo Colegiado do Programa de Pós-Graduação em Engenharia Elétrica da Universidade Federal de Minas Gerais, como parte dos requisitos necessários à obtenção do grau de Doutor em Engenharia Elétrica.

Orientador: Victor Flores Mendes
Co-orientadores: Heverton Augusto Pereira and Allan Fagner Cupertino

Belo Horizonte - MG
03 de Agosto de 2021.

"Lifetime Evaluation Of Photovoltaic Inverters With Capability Of Reactive Power Support"

Erick Matheus da Silveira Brito

Tese de Doutorado submetida à Banca Examinadora designada pelo Colegiado do Programa de Pós-Graduação em Engenharia Elétrica da Escola de Engenharia da Universidade Federal de Minas Gerais, como requisito para obtenção do grau de Doutor em Engenharia Elétrica.

Aprovada em 03 de agosto de 2021.

Por:

Victor Flores Mendes
01971014532

Prof. Dr. Victor Flores Mendes
DEE (UFMG) - Orientador

Prof. Dr. Heverton Augusto Pereira (coorientador)
Universidade Federal de Viçosa

ALLAN FAGNER CUPERTINO:
09897670602

Prof. Dr. Allan Fagner Cupertino (coorientador)
Centro Federal de Educação Tecnológica de Minas Gerais
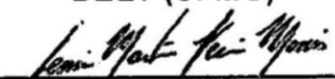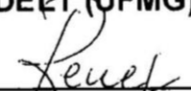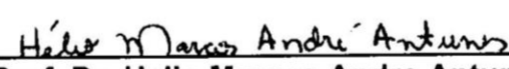
Tomas Perpetuo Correa:
05844733622

Prof. Dr. Tomas Perpetuo Correa
DELT (UFMG)

Prof. Dr. Lenin Martins Ferreira Morais
DELT (UFMG)

Prof. Dr. José Renes Pinheiro
Universidade Federal de Santa Maria

Prof. Dr. Helio Marcos Andre Antunes
Universidade Federal do Espírito Santo

Dra. Livia Maria de Rezende Raggi
Agência Nacional de Energia Elétrica (ANEEL)

À minha esposa Fernanda e meu filho Matheus.
À minha família, mentores e amigos.

Agradecimentos

Ao amor, paciência e dedicação durante todos os dias desta jornada, eu gostaria de agradecer imensamente à minha esposa Fernanda. Além de todo o suporte que você me deu para que esta tese pudesse ser finalizada, você me presenteou com o meu bem mais precioso, o nosso filho Matheus. Foi graças a vocês dois que eu tive forças e vontade para superar os desafios do doutorado, intensificados pela pandemia do COVID19. O meu muito obrigado, meus amores. Eu amo vocês.

Agradeço também o eterno e incondicional amor e apoio que recebi dos meus familiares, em especial os meus pais Everaudo e Denise e do meu irmão Laio, que me acompanham desde sempre (mesmo que à distância), me guiando pelos melhores caminhos, me ensinando o certo e corrigindo o errado. Sem vocês eu nada seria.

À oportunidade de ensino, agradeço primeiramente à Universidade Federal de Minas Gerais (UFMG) e ao Programa de Pós-Graduação em Engenharia Elétrica (PPGEE). Agradeço também à Universidade Federal de Viçosa - Campus Florestal (UFV-CAF), pelo suporte para execução deste trabalho e aos professores dos cursos técnicos em Eletrotécnica e Eletrônica, que apoiaram a minha saída de licença para a conclusão deste trabalho.

Destaco a importância do meu orientador, o prof. Victor Flores Mendes, nessa jornada. Obrigado, Victor, por todo o conhecimento compartilhado ao longo destes anos. Agradeço também os meus co-orientadores, os prof. Heverton Augusto Pereira e Allan Fagner Cupertino. Heverton, que já me

"Prediction is very difficult, especially if it's about the future."

Niels Bohr

Resumo

Devido às características intermitentes da irradiância solar, os inversores fotovoltaicos (FV) normalmente operam abaixo das condições nominais de potência. Neste cenário, inversores FV podem ser usados para realizar serviços ancilares, tais como compensação de potência reativa. Entretanto, isso afeta a confiabilidade do inversor. A relação entre a compensação de potência reativa e consumo de vida útil sob diferentes condições de fator de carregamento do inversor (FCI) ainda não foram abordadas na literatura. Portanto, esta tese de doutorado investiga a vida útil de inversores multifuncionais trifásicos de dois estágios com capacidade de suporte de potência reativa sob diferentes FCI. Os fundamentos de confiabilidade baseados em modelos empíricos de vida útil e análises estatísticas das simulações de Monte Carlo são fornecidos. A metodologia é aplicada a três perfis de missão, com diferentes condições meteorológicas. Quando o inversor FV multifuncional é usado para compensar um perfil de potência reativa, a sua vida útil é reduzida. Além disso, uma análise baseada no Custo Nivelado de Energia mostrou que o suporte de potência reativa aumenta os custos do sistema FV. Portanto, a compensação parcial pode ser uma estratégia interessante para melhorar a confiabilidade do inversor multifuncional. Finalmente, o inversor FV multifuncional é utilizado para regular o fator de potência (FP) de uma carga industrial. Para baixas condições de carga, o inversor consegue regular o FP sem sofrer relevantes reduções na sua vida útil. Entretanto, a medida que o tamanho da carga aumenta, mais potência reativa é requerida para regular o FP e, consequentemente, mais significativa é a redução de vida útil do inversor FV multifuncional.

Palavras-chave: Avaliação de vida útil, compensação de potência reativa, Custo Nivelado de Energia, fator de carregamento, sistemas fotovoltaicos.

Abstract

Due to the intermittent characteristic of the solar irradiance, photovoltaic (PV) inverters usually operate below rated power conditions. In this scenario, commercial PV inverters can be used to provide ancillary services, such as reactive power compensation. However, it affects the PV inverter reliability. The trade-off between reactive power compensation and lifetime consumption under different inverter sizing ratio (ISR) was not previously addressed in the literature. Hence, the present Ph.D thesis investigates the lifetime of a multifunctional three-phase two-stage PV inverter with capability of reactive power support under different ISR conditions. The fundamentals of reliability based on empirical lifetime models and statistic analysis using Monte Carlo simulations are provided. The methodology is applied to three mission profiles, with different meteorological conditions. When the multifunctional PV inverter compensates a reactive power profile, the lifetime is reduced. Furthermore, an economic analysis based on Levelized Cost of Electricity (LCOE) showed that the reactive power support increases the system costs. Therefore, partial reactive power compensation can be an interesting reliability-oriented strategy to improve the multifunctional PV inverter lifetime. Finally, multifunctional PV inverter is applied to an industry load profile to regulate its power factor (PF). For low load condition in comparison with the PV energy generation, the PV inverter can regulate the power factor without suffering relevant reductions on its lifetime. However, as the load increases, more reactive power is required to regulate the PF and consequently, more significant reductions on the PV inverter lifetime are observed.

Keywords: Inverter sizing ratio, lifetime evaluation, Levelized Cost of Electricity, photovoltaic systems, reactive power compensation.

List of Figures

List of Tables

List of Acronyms

ABNT	*Associação Brasileira de Normas Técnicas*
ABSolar	*Associação Brasileira de Energia Solar*
ac	Alternating current
Ag	Silver element
AGREE	Advisory Group on Reliability of Electronic Equipment
Al	Aluminum element
Al-Caps	Aluminum electrolytic capacitors
AM	*Ante meridiem*
ANEEL	*Agência Nacional de Energia Elétrica*
BESS	Battery Energy Storage System
CAF	*Campus Florestal*
CDF	Cumulative Density Function
CIPS	Intl. Conf. on Integrated Power Electronics Systems
CNET	*Centre National d'études des télécommunications*
COVID19	Coronavirus Disease 2019
CTE	Coefficient of thermal expansion
dc	Direct current
DCB	Direct bonded copper
DER	Distributed energy resource
DfR	Design for Reliability
DG	Distributed generation
DR	Discount rate
EMALS	Eletromagnetic Aircraft Launch Systems
EP	Energy produced
EPCI	Equity project cost investiment
EPS	Electric power system
ESL	Equivalent series inductor

ESR	Equivalent series resistance
EVA	Ethylene vinyl acetate
FCI	*Fator de Carregamento do Inversor*
FFT	Fast Fourier Transform
FP	*Fator de Potência*
FV	*Fotovoltaico*
GESEP	*Gerência de Especialistas em Sistemas Elétricos de Potência*
HCC	Harmonic current compensation
HRD	Handbook of Reliability Data
IEC	International Electrotechnical Commission
IEEE	Institute of Electrical and Electronic Engineers
IGBT	Insulated Gate Bipolar Transistor
ISR	Inverter sizing ratio
IRI	Inverter replacement investiment
IR	Inverter replacement
LCL	Inductance Capacitance Inductance filter
LCOE	Levelized Cost of Electricity
LVRT	Low voltage ride-through
MATLAB	Matrix Laboratory
MBB	Multi bus bars
MG	*Minas Gerais*
MLC-Caps	Multi-layer ceramic capacitors
MP	Mission profile
MPP	Maximum power point
MPPT	Maximum power point tracking
MPPF-Caps	Metallized polypropylene film capacitors
MOSFET	Metal Oxide Semiconductor Field Effect Transistor
NBR	*Norma Técnica Brasileira*
NOCT	Nominal operating cell temperature
OM	Operational maintenance
P&O	Pertub and Observe
PCC	Point of common coupling
PDF	Probability distribution function
PE	Power electric
PERC	Passivated emitter rear cell
PF	Power factor
Ph.D	*Philosophiae Doctor*

PI	Proportional integral
PLECS	Piecewise Linear Electrical Circuit Simulation
PM	*Post meridiem*
PoF	Physisc-of-Failure
PPGEE	*Programa de Pós-Graduação em Engenharia Elétrica*
pu	Per unit
PV	Photovoltaic
PWM	Pulse width modulation
RC	Resistance and Capacitance
REN	Renewables Now!
RMS	Root mean square
RPP	Reliability Prediction Procedure
SAM	Scanning acoustic microscope
SC	Synchronous condenser
SDR	System degradation rate
SG	Component strength
SPWM	Sinusoidal pulse width modulation
SRF-PLL	Synchronous Reference Frame Phase-Locked Loop
ST	Component stress
STATCOM	Static Synchronous Compensator
STC	Standard test condition
SVC	Static var compensator
SVPWM	Space vector pulse width modulation
TDK	Tokyo Denki Kagaku
THD	Total harmonic distortion
TIM	Thermal interface material
TR	Technical Report
UFMG	*Universidade Federal de Minas Gerais*
UFV	*Universidade Federal de Viçosa*

List of Symbols

α	Curve fitting coefficient (IGBT lifetime model)
β	Curve fitting coefficient (IGBT lifetime model)
γ	Curve fitting coefficient (IGBT lifetime model)
γ_p	PV module power temperature coefficient
$\Delta\alpha_s$	Mismatched CTE between solder joint layers
ΔC	Capacitance variation
$\Delta G\%$	Percent solar irradiance variation
Δi_L	Inductor ripple current
Δp_K	Rated peak difference between load and PV active power
$\Delta Q_{AAL,max}$	Max. int. of comp. reactive power over time for Aalborg
$\Delta Q_{GOI,max}$	Max. int. of comp. reactive power over time for Goiânia
$\Delta Q_{IZA,max}$	Max. int. of comp. reactive power over time for Izaña
$\Delta T\%$	Percent ambient temperature variation
$\Delta T'_j$	Static junction temperature variation
ΔT_j	Junction temperature variation (swing)
η	Weibull PDF scale parameter
θ	Inverter displacing angle
μ	Weibull PDF shape parameter
ξ	Damping ratio
ρ	Grid voltage space vector angle
τ_{th}	Thermal time constant
ω_0	Grid fundamental frequency in rad/s
ω_n	Natural frequency in rad/s

A	Technology factor coefficient (IGBT lifetime model)
ar	Aspect ratio
B_{10}	Time when 10% of the population failed
B_x	Time when x% of the population failed
c_s	Fatigue exponent (IGBT lifetime model)
C	Capacitance
C_b	Boost converter input capacitor
C_d	Curve fitting coefficient (IGBT lifetime model)
C_{dc}	Dc-link capacitor
C_f	LCL filter capacitor
C_{th}	Thermal capacitance
d	Duty cycle
d^*	Duty cycle reference
D	Bondwire diameter
D_b	Boost converter diode
DF	Dissipation factor
E_a	Activation energy
E_{pv}	Annual energy produced by the PV system
$E_{load,pu}$	Annual consumed energy by the load in pu
E_{off}	IGBT Turn-off energy
E_{on}	IGBT Turn-on energy
E_{rec}	Diode reverse recovery energy
Ek_L	Scale factor between PV energy and load consumption
f	Frequency
$f(x)$	Weibull Probability Density Function (PDF)
f_0	Grid fundamental (line) frequency in Hz
f_b	Boost converter switching frequency
f_c	Cyclic frequency
f_{ci}	Cut-off frequency of dc-ac stage inner loop PI controller
f_{cib}	Cut-off frequency of dc-dc stage inner loop PI controller
f_{cp}	Cut-off frequency of dc-ac stage Q outer loop PI controller
f_{cv1}	Cut-off frequency 1 of dc-ac stage P outer loop PI controller
f_{cv2}	Cut-off frequency 2 of dc-ac stage P outer loop PI controller
f_{cvb}	Cut-off frequency of dc-dc stage outer loop PI controller
f_d	Diode parameter (IGBT lifetime model)
f_i	Inverter switching frequency
f_{sw}	Switching frequency

$F_{comp}(x)$	Component unreliability function
$F_{sys}(x)$	System unreliability function
G	Solar irradiance
G_b	Solar irradiance from base case
G_{NOCT}	Solar irradince at NOCT
$G_{x\%}$	Varied solar irradiance
h	Harmonic order of the fundamental frequency
H_{ar}	Bondwire height
i_b	Boost converter inductor current
i_b^*	Boost converter inductor reference current
i_c	IGBT collector current
$i_{c,avg}$	IGBT average collector current
$i_{c,rms}$	IGBT RMS collector current
$i_{cap,rms}$	Capacitor RMS current
i_{Cb}	Boost converter input capacitor current
i_{Db}	Boost converter diode current
i_{dc}	Dc-link capacitor current
i_f	Diode forward current
i_g	Grid current
$i_{g,abc}$	Grid current in natural reference frame
$i_{g,d}$	Grid current in direct axis
$i_{g,d}^*$	Grid reference current in direct axis
$i_{g,dq}$	Grid current in rotating reference frame
$i_{g,q}$	Grid current in quadrature axis
$i_{g,q}^*$	Grid reference current in quadrature axis
i_{inv}	Invert input current
i_{pv}	Photovoltaic module/array current
i_s	Inverter output current
i_{Sb}	Boost converter IGBT current
I	Current
I_{cap}	Capacitor current
$I_{cap,rms}$	Capacitor RMS current
I_b	Current per bondfoot
$\hat{I}_f$	Amplitude of grid phase voltage
k	Number os samples in Monte Carlo simulations
k_b	Boltzmann constant
k_i	Integral gain

k_p	Proportional gain
L	Capacitor number of hours
L_0	Capacitor number of hours under rated conditions
L_{ar}	Bondwire length
L_b	Boost converter inductor
L_f	Inverter-side LCL filter inductor
L_g	Grid-side LCL filter inductor
L_m	Mission profile sample time in hours
L_s	Lateral size of solder joint
L_t	Sum of LCL inverter and grid inductance
LC	Lifetime consumption
LC_c	Capacitor lifetime consumption
LC_s	IGBT lifetime consumption
M	Modulation index
n	Voltage coefficient (capacitor lifetime model)
N	PV system expected useful life
N_b	Number of parallel boost converters
N_f	Number of cycles to failure
P	Active power
P^*	Active power reference
P_c	Conduction power loss
$P_{c,diode}$	Diode conduction power loss
$P_{c,IGBT}$	IGBT conduction power loss
P_{grid}	Active power delivered to the grid
P_{load}	Load Active power
P_{loss}	Power loss
$P_{loss,cap}$	Capacitor power loss
$P_{loss,dev}$	Device power loss
$P_{loss,diode}$	Diode power loss
$P_{loss,IGBT}$	IGBT power loss
$P_{loss,tot}$	Total power loss
P_{pv}	Active power generated by the PV modules
$P_{pv,max}$	Maximum active power generated by the PV modules
$P_{pv,MPPT}$	Active power generated by the PV modules at MPP point
$P_{pv,tot}$	Total active power generated by the PV array
P_{sw}	Switching power loss
$P_{sw,diode}$	Diode switching power loss

$P_{sw,IGBT}$	IGBT switching power loss
Q	Reactive power
Q^*	Reactive power reference
Q_{load}	Load reactive power
Q_{max}	Maximum reactive power
Q_R	Reactive power derating factor
s	Complex frequency
S	Apparent power
S_G	Grid apparent power
S_I	Inverter apparent power
S_L	Load apparent power
S_n	Rated apparent power
S_{1-6}	Inverter IGBTs
S_1	Inverter upper IGBT from phase A
S_2	Inverter lower IGBT from phase A
S_3	Inverter upper IGBT from phase B
S_4	Inverter lower IGBT from phase B
S_5	Inverter upper IGBT from phase C
S_6	Inverter lower IGBT from phase C
S_b	Boost converter IGBT
t	Instant of time
t_0	Start time of the signal period
t'_{on}	Static load pulse duration
t_{on}	Load pulse duration
T	Signal period
T_0	Capacitor rated temperature
T_{amb}	Ambient temperature
$T_{amb,b}$	Ambient temperature from base case
$T_{amb,NOCT}$	Ambient temperature at NOCT
$T_{amb,x\%}$	Varied ambient temperature
T_c	Case temperature
T_j	Junction temperature
$T_{j,diode}$	Diode junction temperature
$T_{j,IGBT}$	IGBT junction temperature
T'_{jm}	Static mean junction temperature
T_{jm}	Mean junction temperature
$T_{j,max}$	Maximum junction temperature

T_h'	Static hot-spot temperature
T_h	Hot-spot temperature
T_m	Photovoltaic module operating temperature
T_m^*	Photovoltaic reference module operating temperature
$T_{m,NOCT}$	Photovoltaic module operating temperature at NOCT
T_s	Sample time
R_b	Boost converter inductor resistance
R_d	Passive damping resistor
r_g	IGBT gate resistance
R_{mp}	Equivalent resistance at maximum power point
R_p	Parallel resistance
R_t	Sum of LCL inverter and grid inductors resistance
R_{th}	Thermal resistance
$R_{th,b}$	Boost converter input capacitor thermal resistance
R_{th_c-h}	Case-to-heatsink thermal resistance
R_{th_cap}	Capacitor thermal resistance
$R_{th,dc}$	Dc-link capacitor thermal resistance
R_{th_h-a}	Heatsink-to-ambient thermal resistance
$R_{th_h-a,max}$	Maximum heatsink-to-ambient thermal resistance
R_{th_j-c}	Junction-to-case thermal resistance
$R_{th_j-c,d}$	Diode junction-to-case thermal resistance
$R_{th_j-c,i}$	IGBT junction-to-case thermal resistance
$U(x)$	Unreliability function
$U_1(x)$	Unreliability equal to 1% at specified time
$U_{10}(x)$	Unreliability equal to 10% at specified time
v_{ce}	IGBT collector-emitter voltage
$v_{ce,on}$	IGBT on-state collector-emitter voltage
v_{dc}	Dc-link capacitor voltage
v_{dc}^*	Dc-link capacitor reference voltage
v_f	Diode forward voltage
v_g	Grid voltage
$v_{g,abc}$	Grid voltage in natural reference frame
$v_{g,abc}^*$	Grid reference voltage in natural reference frame
$v_{g,d}$	Grid voltage in direct axis
$v_{g,d}^*$	Grid reference voltage in direct axis
$v_{g,dq}$	Grid voltage in rotating reference frame
$v_{g,q}$	Grid voltage in quadrature axis

$v_{g,q}^*$	Grid reference voltage in quadrature axis
v_{ge}	IGBT gate-emitter voltage
v_{PCC}	Voltage at the point of common coupling
v_{pv}	Photovoltaic module/array voltage
v_{pv}^*	Photovoltaic module/array reference voltage
v_s	Inverter output voltage
V	Voltage
V_0	Capacitor rated voltage
V_c'	Static capacitor voltage
V_c	Capacitor voltage
$\hat{V}_f$	Amplitude of grid phase voltage
$\hat{V}_s$	Amplitude of inverter output phase voltage
x	Weibull PDF operating time
x_s	Thickness of the solder joint
y_s	Ductility factor of the solder joint
Z_{cap}	Capacitor impedance
Z_{th}	Thermal impedance
$Z_{th,j-c}$	Junction-to-case thermal impedance

Contents

Introduction

In this introduction chapter, the advantages of multifunctional operation of photovoltaic inverters with capability of reactive power support are stated. In addition, the reliability history and state-of-art are presented, based on Physics-of-Failure and Design for Reliability approaches. Then, the thesis motivation and contributions are defined, followed by the thesis outline, organization, and list of publications.

1.1 Context and relevance

Photovoltaic (PV) systems have been widely installed worldwide in recent decades, and the penetration level is still increasing. In 2019, the solar PV market grew 12% (around 115 GW) in relation to the previous year, totalizing 627 GW installed around the world. The last decade (2010-2019) ended up with strong and increasing demand, as can be seen in Fig. 1.1. (REN21, 2020).

The continuous cost decrease of the energy produced by photovoltaic plants makes this generation more economically attractive. Globally, the PV module price fell around 12% in 2019, averaging 0.36 U$/W, with significant variations depending on the country (MINTS, 2020). Brazil figures among the countries with lowest bid prices. During the A-4 auction, occurred in 2019, the average electricity price of PV systems (67.48 R$/MWh or 17.62 U$/MWh) were recorded as the lowest price among the competing technologies (wind power and natural gas) (ABSOLAR, 2019).
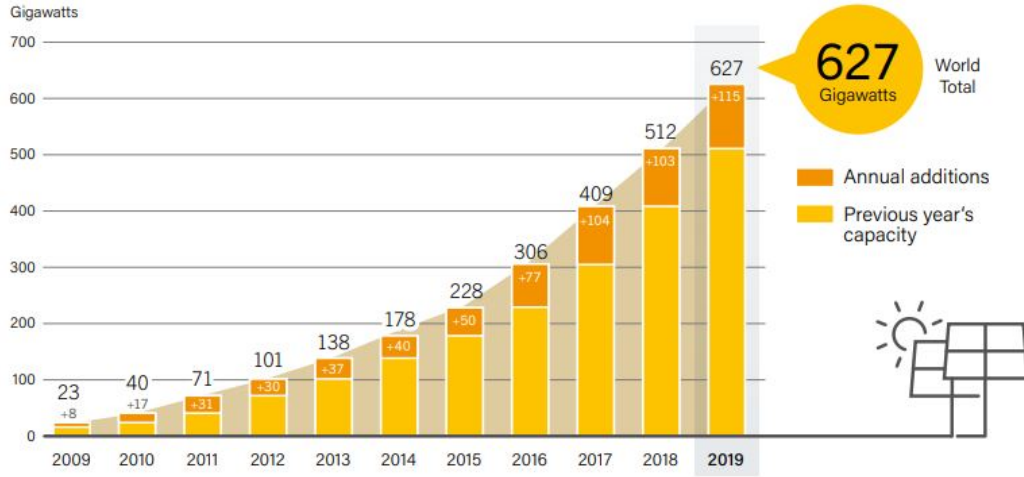
Figure 1.1: Solar photovoltaic global capacity and annual additions from the last decade. Data and chart extracted from REN21 (2020).

According to ANEEL (2017), more than 99% of the distributed generation (DG) in Brazil are represented by photovoltaic systems. The ABNT NBR 16149 standard provides technical support to the interconnection of PV inverters with the electrical grid (ABNT, 2013). Additionally, IEEE 1547 also defines the ancillary services to improve the utility grid power quality, such as voltage regulation, harmonic current compensation and reactive power support (IEEE, 2018). Therefore, aside from the main role of injecting active power to the grid, PV inverters can perform ancillary services to improve grid power quality, being named as multifunctional PV inverters.

1.1.1 Multifunctional PV inverters

The high penetration of grid-tied PV systems interfaced by power electronic converters can severally affect the power system. In this scenario, conventional PV systems can be used to provide ancillary services, such as reactive power support and harmonic current compensation, becoming a multifunctional PV inverter. These extra services can be used to improve grid quality and avoid penalties from the power distribution company (Pinto; Zilles, 2014).

With the high penetration of PV power plants, grid-code requirements have been developed to deal with issues like fault ride-through, reactive power management and voltage control. The reactive power control strategies in accordance with different grid-code requirements are described in Yang, Wang e Blaabjerg (2014) and Sarkar, Meegahapola e Datta (2018). Besides reactive power injection, multifunctional PV inverters can also support the grid with harmonic current compensation (HCC) (Wang et al., 2020; Mantilla; Petit; Ordóñez, 2021). The impacts of HCC on the inverter lifetime are addressed in Lledó-Ponsati et al. (2019) and Barros et al. (2021).

In the distribution stage of the power system, the PV inverters can develop an important role injecting reactive power to the electrical grid. Classical techniques are still applied, such as static var compensators (SVC) and synchronous condensers (SC), as shown in Fig. 1.2 (Dixon et al., 2005). SVC are composed of capacitors and inductor banks controlled by thyristors to compensate both lead and lag reactive power. However, the switching operation of thyristors generates low-order harmonic currents to the grid, which requires large use of passive filters (Tanaka, 2018). On the other hand, SC are synchronous machines used to generate or absorb reactive power. SC presents high losses and cost when compared to other technologies, but they are still widely used due to additional capacity to provide inertia and regulate the grid frequency (Igbinovia et al., 2015). Modern topologies such as STATCOM (Static Synchronous Compensators) and BESS (Battery Energy Storage Systems) are also used as solutions to provide reactive power support to the point of common coupling (PCC) (SANDIA, 2015; Cupertino, 2019). Finally, PV inverters can be an interesting solution to provide reactive power support (Gusman et al., 2020). In this sense, multifunctional PV inverters with reactive power capability can be used as:

- Power factor regulation in industrial applications;

- Voltage regulation at the point of common coupling;

- Grid support under transient fault occurrences, providing low voltage ride through capability.
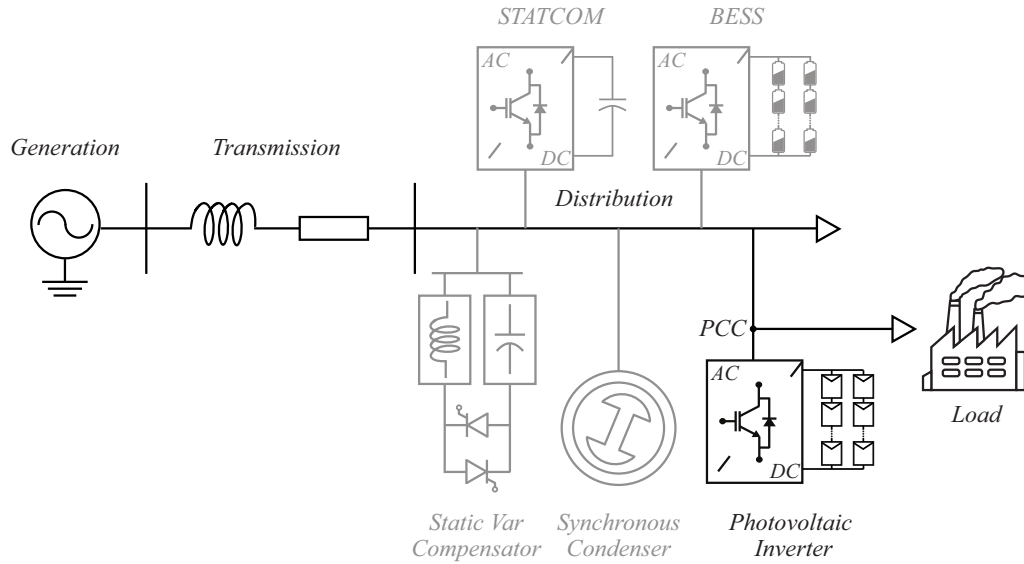
Figure 1.2: Reactive power compensators in distribution stage of electrical power system.

1.2   State-of-art of power electronics reliability

In power electronics, the expression lifetime or end-of-life refers to the time which a specific object (mechanism, component, converter or system) reaches its failure criteria. Increase of series resistance, maximum variation of capacitance, increase in the voltage drop, stage of being economically unviable are examples of failure criteria (Chung et al., 2015). The object not necessarily explodes, gets destroyed or instantly stop working when the failure criteria are achieved. It just means that it becomes inappropriate to continue operating under such conditions. Therefore, it is important to study Physics-of-Failure (PoF) and Design for Reliability (DfR) methodologies to identify the failure mechanisms and define reliability targets to improve power electronic components reliability.

1.2.1   History of lifetime prediction

After the Second World War, between 1943-1950, the United States started to collected data from military environment electronic systems. The

first concerns about frequency of failure were related to communication and navigation. The Reliability Engineering as a distinct discipline was born in 1957 after the Advisory Group on Reliability of Electronic Equipment (AGREE) report was published. This report contained specifications and tests regarding reliability of electronic components, such as integrated circuits, transistors, diodes, resistors, capacitors, relays, switches, connectors, etc (AGREE, 1957).

After that, quantitative reliability prediction based on empirical data and various handbooks were released by military and industry (Pecht; Nash, 1994). The first handbook containing failure rates expressed as function of working hours and the standardization of reliability calculation was released in 1959. This handbook is known as Procedure and Data for Estimating Reliability and Maintainability, or just Martin Titan Handbook (Martin, 1959). In 1965, the American Department of Defense released the first version of the handbook-based constant failure rate model, known as Military Handbook 217A (Military Handbook, 1965). Around 1962, the first concept of Physics-of-Failure (PoF) were presented to investigate the root cause of failure mechanism analysis and the impact of materials, defects, and stresses on product reliability (Pecht; Dasgupta, 1995). Despite the initial efforts with PoF, the most predominant method to evaluate lifetime of electronic components was based on the military handbook approach.

The Military Handbook 217 received several data and proceedings updates, reaching series F1 in 1991 and F2 in 1995 (Military Handbook, 1991; Military Handbook, 1995). Besides it, other handbooks and reliability manuals were developed in the field of telecommunications. Among these are RPP manual published by Bell Core, HRD manual published by British Telecom and the Italtel IRPH93 manual, with the collaboration of both the French CNET and British Telecom (Lazzaroni et al., 2011).

After 1990, with the advance in power electronic systems and its complexity, evidences suggested that constant failure rate were inadequate (White; Bernstein, 2008). Companies and organizations have updated the Military-Handbook-217 data and methodology, such as Telcordia SR-322, Siemens SN29500 and RDF-2000. However, all these approaches carried the same shortcomings of not being effectively applied to the emerging new

technologies (Peyghami; Wang; Blaabjerg, 2020). In that scenario, PoF starts to gain space and its approach became widespread.

In 2004, the International Electrotechnical Commission (IEC) provided a Technical Report (TR 62380), which includes the procedures for reliability prediction of electronic components considering mission profile as inputs (IEC TR 62380, 2006). The IEC TR 62380 was replaced by IEC 61709 in 2017 providing guidance of the use of failure rate data for reliability prediction of electric components used in equipment under mission profile operation (IEC 61709, 2017). It is worth mentioning FIDES, a French armament industry supervision agency study conducted by an European consortium formed by eight industries from the fields of aeronautics and military. FIDES Methodology is based on the physics of failures and supported by the analysis of test data, field returns and existing modeling (FIDES, 2018). The last FIDES Guide was released in 2010. A summary of the time evolution of lifetime proceedings over the years is illustrated in Fig. 1.3.
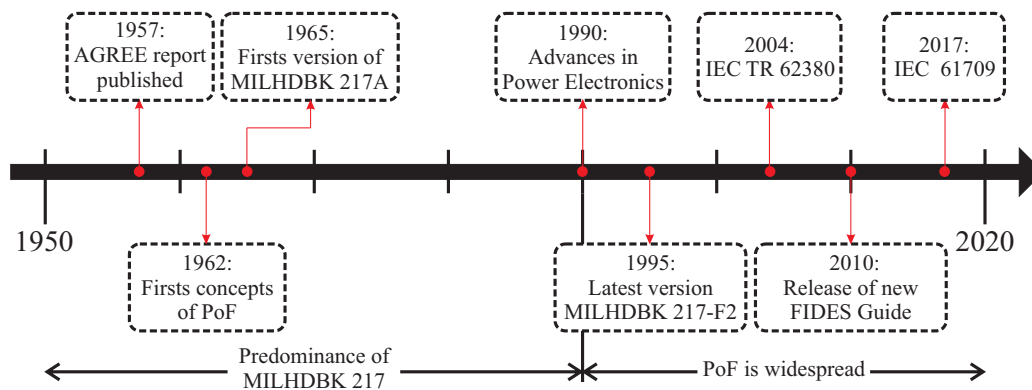
Figure 1.3: Lifetime proceedings evolution over the years. Adapted from Chung et al. (2015)

1.2.2   Classification of failure types

A typical electronic system reliability can be affected by different types of failures, as shown in Fig. 1.4 (Peyghami; Wang; Blaabjerg, 2020). The software failures occur due to miss-operation or programming error. In a certain way, the software failures are related to human errors, due to lack

of training or inadequate testing. The software reliability can be predicted according to IEEE Standard 1633 (IEEE, 2017). Other types of human errors are summarized in Fig. 1.4, such as ergonomic issues or non-routine operation. Hardware failures are the object of study of this thesis.
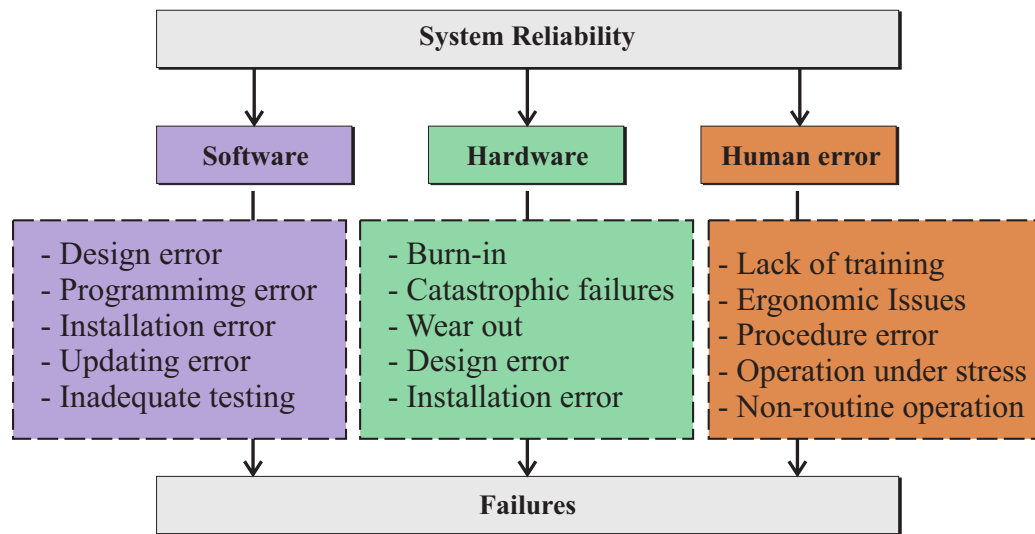
Figure 1.4: The classification of failure types in the power electronic system reliability. Adapted from Christen, Stojadinovic e Biela (2017).

A typical hardware hazard function (failure rate) is shown in Fig. 1.5 with steep sides and a flat bottom. Due to its format, this curve is usually known as "bath tub curve". The total failure rate over the operating time is the sum of three regions: "infant mortality" or early failures, catastrophic failures and aging failures (or wear out) (Ross, 2018). The early failures usually occurr on the start-of-life, caused by defects and weakness in design of manufacturing phase. The catastrophic failures are complex to predict, since they derive from random and unexpected single events, such as overcurrent, overvoltage or instabilities (Wu et al., 2013). Thus, during the long operation time of the component, the catastrophic failures are modeled as constant. On the other hand, aging failures takes place in the end-of-life, and can be predicted based on lifetime models.
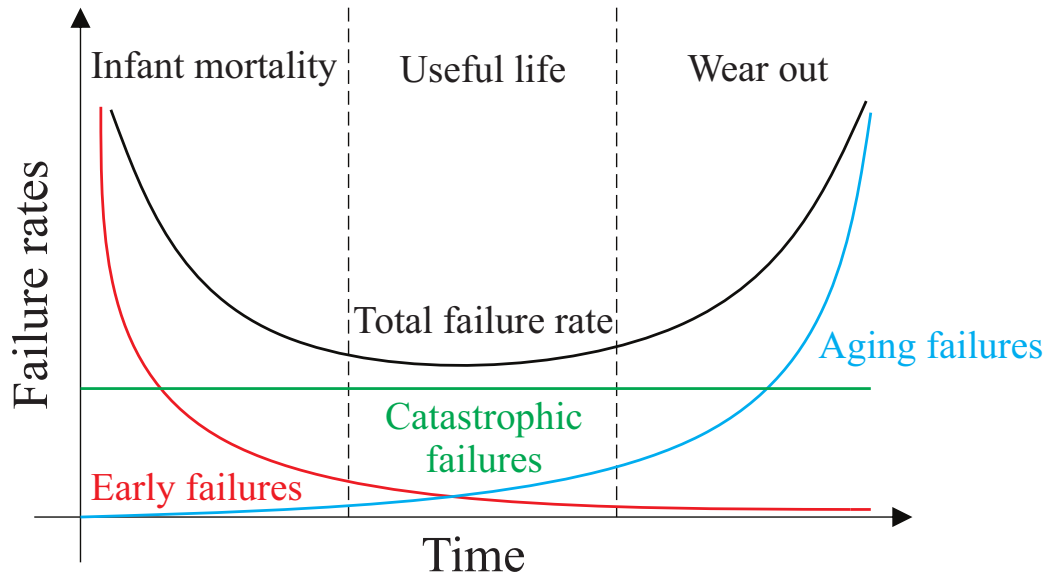
Figure 1.5: Hazard function of conventional bath tub curve. Adapted from Ross (2018).

1.2.3   Physics-of-Failure methodology

The Physics-of-Failure approach aims to identify the root-cause failure mechanisms in the component level (Pecht; Dasgupta, 1995). Compared to traditional handbook-based methodology, PoF does not consider components with constant failure rates in the system level. Instead, PoF can provide different reliability models based on the strength and stress in which the component is submitted. The component stress (ST) refers to current or voltage levels, thermal loading cycles, mechanical vibration, humidity, etc. In the same way, the component strength (SG) is related to physical property, such as hardness, soldering, melting point, adhesion, etc. (O'Connor; Kleyner, 2012). Fig. 1.6 illustrates the PoF applied to stress-strength frequency of occurrence.

At the beginning of the operation, component stress and strength probability distribution functions (PDF) are not interfaced. However, overstresses and degradation processes over time increases the stress and decreases the strength of the component, respectively. At a certain point, defined by failure criteria and reliability metrics, the PDF are interfaced and the failure occurs. This analysis suggests the component service life can
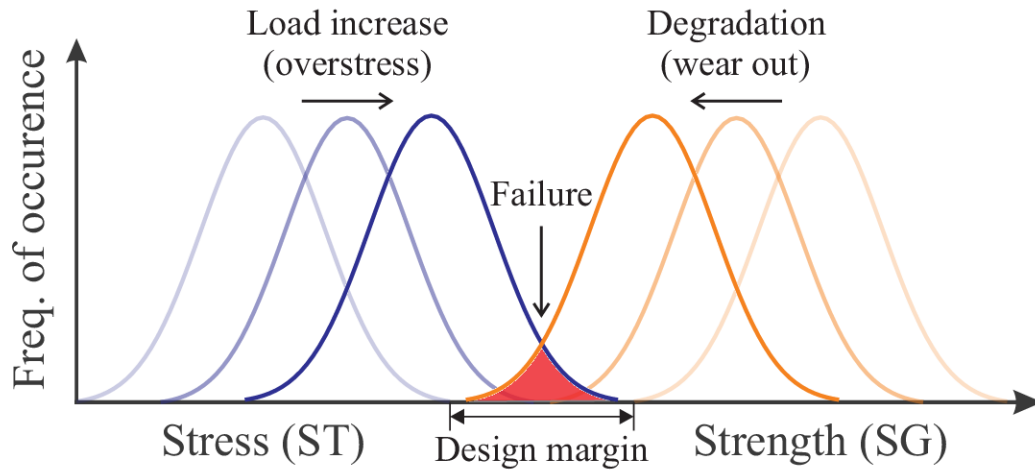
Figure 1.6: Stress-strength frequency of occurrence with failure over time due to overstress and wear out. Adapted from Sintamarean et al. (2015) and Cupertino (2019)

be improved by either increasing the strength or reducing the stresses (Chung et al., 2015). Therefore, there is a design margin where reliability engineering can act to reduce components failure and increases its lifetime.

1.2.4   Design for Reliability approach

The engineering industry in power applications have shown interest in designing electronic systems with longer lifetime and more accurate and reliable components (Musallam et al., 2015). Design for reliability is a modern concept wherein the system lifetime is taken into account at the design stage, reducing the high costs of preventive and emergency maintenance (Yang et al., 2015). The DfR based on mission profiles (MP) can be used to address the most reliable components for a specific power electronic system, enhancing energy conversion efficiency and reducing costs with unscheduled maintenance and system downtime (Sintamarean et al., 2015). The mission profile are a set of conditions that defines the system operation and the load stresses. In the case of PV systems, the mission profiles are measured data of solar irradiance and the ambient temperature, used as input of the PV inverter electrical simulation. A flowchart of DfR approach applied to a generic system is presented in Fig. 1.7.
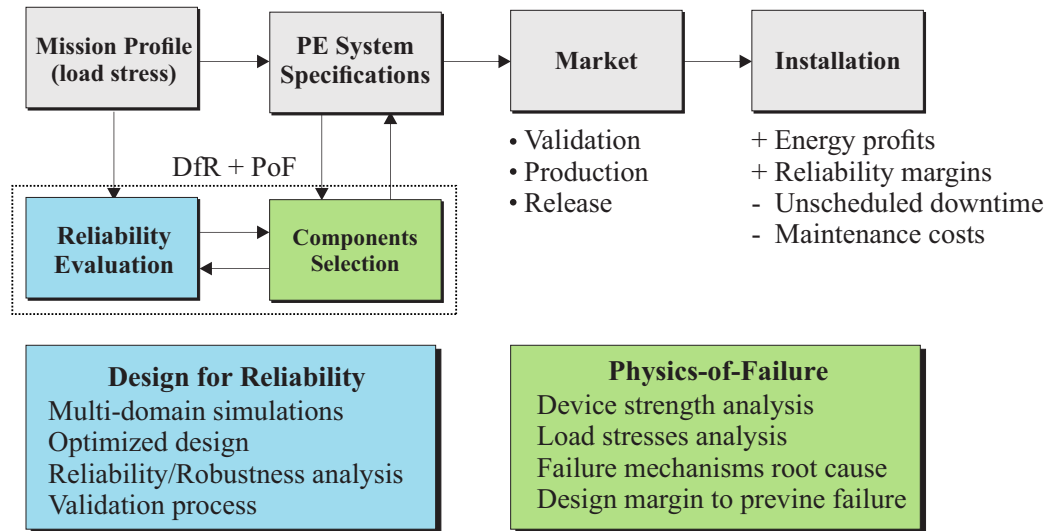
Figure 1.7: Design for Reliability flowchart for mission profile based PV system
reliability analysis.

The initial power electronic system is designed with conventional
specifications (e.g., minimum dc-link capacitance, switching frequency,
power semiconductor ratings, etc.) (Wang et al., 2013). However, the
conventional design can be replaced by components with a more reliable
operation after the DfR and PoF analysis. As a consequence, the power
electronic system will have energy profits, increased lifetime and reduced
costs with maintenance and downtime.

Considering PV applications, the DfR approach can be an important
tool to evaluate the multifunctional operation of the PV inverter
(Sangwongwanich et al., 2018a). Ancillary services such as reactive power
compensation can affect the PV inverter components reliability (Anurag;
Yang; Blaabjerg, 2015; Gandhi et al., 2019; Zhou; Wang; Blaabjerg, 2020).
In this context, the Physics-of-Failure theory is used to identify possible
failures mechanisms caused by electro-thermal-mechanical stresses in the
PV inverter components (Shao et al., 2014; Wang et al., 2014).

According to a survey presented in Moore e Post (2008), the PV
inverter is the main cause of unscheduled maintenance and accounts for
almost 60% of the total system installation cost. Electrolytic capacitors and
switching semiconductors are the most fragile components of the PV

inverter and accounts for 34% and 31% of failure rates, respectively (Yang et al., 2011). In addition, a recent survey reported that power semiconductors devices and capacitors are the most desired components to be investigated in future researches, according to the industry perspective (Falck et al., 2018). Therefore, the next chapters will address the stressor parameters, failure mechanisms and reliability analysis of these two components.

1.3   Purposes and contributions

1.3.1   Motivations

Several works in the literature have focused their efforts on the reliability analysis of PV inverters. In Sangwongwanich et al. (2018b), the authors analyze the effects of PV array oversizing in the inverter reliability. Additionally, in Shen et al. (2019) the authors propose a wear out failure analysis of an impedance source PV microinverter. In Bouguerra et al. (2020), the impacts of PV module positioning and degradation are evaluated in terms of the converter lifetime. Recently, Sangwongwanich et al. (2020) stated a mission profile-oriented control to enhance PV inverter lifetime performing active power curtailments. Also, Lenz et al. (2019) compared capacitor power losses calculation methods for wear out failure prediction in PV inverters.

The impacts of reactive power injection on the thermal loading of PV inverters are stated in Sreechithra, Jirutitijaroen e Rathore (2013). Additionally, these thermal loadings are translated to a reliability analysis with reactive power injection outside feed-in operation hours in Anurag, Yang e Blaabjerg (2015). Besides, Zhang et al. (2014) proposes a thermal control technique to improve the power device reliability in wind power converters. Moreover, Gandhi et al. (2019) formulates the cost of reactive power from PV inverters considering the inverter degradation caused by the reactive power provision. Recently, Callegari et al. (2021) proposed a minimum dc-link voltage control for efficiency and reliability improvements in PV inverter with reactive power capability.

Despite the high research efforts focused on the reliability of PV systems, there are yet unexplored fields with lack of studies evolving lifetime prediction. Usually, the same PV inverter part number can be employed at different sites, being submitted to different inverter sizing ratio (ISR). Therefore, the inverter components would suffer different stress levels. Additionally, the increase of ISR impacts on the reactive power margin, reducing the PV inverter capability to injection reactive power. Currently, relevant works matching ISR with reactive power capability are still missing in the literature.

As the main contribution, this work presents a reliability-based trade-off analysis of a PV inverter with reactive power compensation under different ISR conditions. To strengthen the results, an economic analysis based on the Levelized Cost of Electricity (LCOE) is performed to compare the PV inverter operation under different sizing ratio and reactive power conditions.

1.3.2   Objectives

In view of the general motivation and to achieve the main contribution discussed above, the following topics will be addressed in this Ph.D thesis:

1. *Sensitivity analysis of the impact of meteorological variables on the PV inverter reliability*: Since the same PV inverter part number can be employed at different locations, the mission profile-based reliability analysis is an important tool to evaluate the system lifetime for a specific installation site. From the first time in the literature, the thermal dynamics of the PV modules are considered in the process. Therefore, this topic proposes a reliability analysis of the lifetime evaluation when some variations are inserted in the solar irradiance and ambient temperature profiles, simulating meteorological changes and climatic randomness.

2. *Lifetime prediction of multifunctional PV inverter with reactive power capability*: When injecting reactive power to compensate a load requirement and to improve the local power factor, the PV inverter can be used to replace other capacitor banks. However, the PV inverter is submitted to higher thermal loadings, impacting on its

components lifetime. Therefore, this topic aims to evaluate the wear out of both dc-dc and dc-ac stage components caused by the reactive power injection. Moreover, the most stressed components are reported.

3. *Trade-off analysis of reactive power compensation under different inverter sizing ratio*: It is well known that the reactive power compensation shorten the inverter lifetime. As a consequence, a full load reactive power compensation may lead the system to fail prematurely and make this ancillary service economically unfeasible, as a trade-off. Therefore, if a desired lifetime is defined, there is a maximum reactive power specification which the PV inverter can compensate in agreement with the reliability requirements. In addition, this maximum reactive power value is also function of ISR, since its affects the margin of the PV inverter to compensate reactive power.

4. *Economic analysis of multifunctional PV inverter with reactive power capability*: Although some researchers assume the use of ancillary services in a multifunctional PV inverter can be performed at no cost, there is a trade-off related to the inverter lifetime consumption. As a consequence, the reactive power capability may increase the system overall costs due to inverter replacement investments. Therefore, an economic analysis based on LCOE is performed to compare the PV inverter operation under different sizing ratios and reactive power conditions.

The presented research has been developed in the Laboratório de Conversão e Controle de Energia (LCCE) at the Universidade Federal de Minas Gerais (UFMG). This research has cooperation with the Gerência de Especialistas em Sistemas Elétricos de Potência (GESEP) from Universidade Federal de Viçosa. Also, the Department of Energy Technology of Aalborg University has contributed with this research sharing useful know-how and background on reliability assessment. The author would like to thank Eng. Paula Diaz Reigosa from ABB and prof. Yongheng Yang from Aalborg University for sharing Aalborg mission profiles data. The author also would like to thank prof. João Manoel Lenz from Universidade Regional do Noroeste do Estado do Rio Grande do Sul

and prof. Enes Gonçalves Marra from Universidade Federal de Goiás for sharing Goiânia and Izaña mission profiles data.

To achieve the proposed contributions, this Ph.D thesis makes use of electrical and thermal simulations on PLECS and MATLAB environments. This simulations are responsible for generating look-up tables for a set of input conditions, i.e., solar irradiance, ambient temperature and reactive power profiles. The look-ups are then used to compute power losses and convert them in thermal loading. Finally, the Monte Carlo simulations are used to statistically predict the PV inverter lifetime under such simulated conditions.

The results presented in this thesis are based on statistical analysis to include manufacturing process uncertainties and parameters tolerance. The values of lifetime prediction are figure of merit, which can be used to compare different conditions of the PV inverter operation. Therefore, the simulation results are analyzed in a comparative way, evaluating the different operation scenarios. The failure mechanisms are combined in a single index, allowing the comparison between different designs and conditions. Experimental validation of the lifetime prediction are challenging and not addressed in this thesis, due to the following reasons:

- The statistical analysis cannot be based on a single of a few converter samples;

- In practical applications, more than one failure mechanisms can take place;

- In real field, the root cause or failure mechanism that lead the component/converter to failure is seldom identified.

1.4   Organization of this Ph.D thesis

This Ph.D thesis is organized in six chapters. Chapter 1 concerns the introduction of the thesis, with context and relevance of the problem, motivations and the objectives to be addressed. Chapter 2 presents a review of power electronic devices reliability state-of-art, evidencing the

mechanisms of failure, failure criteria and lifetime models of the most stressed components of the investigated converter. Chapter 3 presents a sensitivity analysis of the mission profiles in the inverter components taking into account the PV module thermal dynamics. Chapter 4 describes the issues of inserting a PV system in the distribution grid, in terms of local power factor for different load profiles. Chapter 5 evaluates the lifetime of a multifunctional PV inverter while injecting reactive power to regulate the power factor. Chapter 6 states the conclusions obtained from this research and a proposal of future development works.

1.5   List of publications

The findings of this thesis have resulted in the publication of three journal papers as follows, in chronological order:

- E.M.S. Brito, A.F. Cupertino, P.D. Reigosa, Y. Yang, V.F. Mendes, H.A. Pereira, "Impact of meteorological variations on the lifetime of grid-connected PV inverters", in Microelectronics Reliability Journal, vol. 88-90, pp. 1019-1024, 2018.

- R.C. Barros, E.M.S. Brito, G.G. Rodrigues, V.F. Mendes, A.F. Cupertino, H.A. Pereira, "Lifetime evaluation of a multifunctional PV single-phase inverter during harmonic current compensation", in Microelectronics Reliability Journal, vol. 88-90, pp. 1071-1076, 2018.

- J.M.S Callegari, M.P. Silva, R.C. de Barros, E.M.S. Brito, A.F. Cupertino, H.A. Pereira, "Lifetime evaluation of three-phase multifunctional PV inverters with reactive power compensation", in Electric Power System Research, vol. 175, 2019.

The author has also contributed to the publication of five journal papers, presented as follows in chronological order:

- A.F. Cupertino, L.S. Xavier, E.M.S. Brito, H.A. Pereira, V.F. Mendes, "Benchmarking of power control strategies for photovoltaic systems under unbalanced conditions", in International Journal of Electrical Power & Energy Systems, vol. 106, pp. 335-345, 2019.

- J.M.S Callegari, A.F. Cupertino, V.N. Ferreira, E.M.S. Brito, V.F. Mendes, H.A. Pereira, "Adaptive dc-link voltage control strategy to increase PV inverter lifetime", in Microelectronics Reliability Journal, vol. 100-101, pp. 113439, 2019.

- A.F. Cupertino, J.M. Lenz, E.M.S. Brito, H.A. Pereira, J.R. Pinheiro, S.I. Seleme Jr., "Impact of the mission profile length on lifetime prediction of PV inverters", in Microelectronics Reliability Journal, vol. 100-101, pp. 113427, 2019.

- R.P. Silva, R.C. Barros, E.M.S. Brito, W.C. Boaventura, A.F. Cupertino, H.A. Pereira, "Pursuing computationally efficient wear-out prediction of PV inverters: The role of the mission profile resolution", in Microelectronics Reliability Journal, vol. 110, pp. 113679, 2020.

- R.C. Barros, E.M.S. Brito, W.C. Boaventura, H.A. Pereira, A.F. Cupertino, "Methodology for bondwire lifetime evaluation of multifunctional PV inverter during harmonic current compensation", in International Journal of Electrical Power & Energy Systems, vol. 128, pp. 106711, 2021.

Theory of lifetime prediction

In modern industry, the production and operation of more reliable and sustainable power converters are very important. For such, great efforts have been focused on more accurate lifetime models to estimate the system end-of-life. This chapter introduces the theory, metrics and procedures of lifetime prediction. The state-of-art of power semiconductor devices and capacitors lifetime models are provided. Moreover, the main failure mechanisms and their stressor parameters on the PV inverter components are investigated. Finally, the most used lifetime models applied to power semiconductors and capacitors are presented.

2.1   Power semiconductors reliability analysis

With the advance and fast growth of power electronic systems, power semiconductor devices are required to operate with high power density, low power losses and prolonged lifetime. These requirements drive reliability challenging while designing part numbers with high efficiency and low volume. Wide bandgap power semiconductors can operate with higher switching frequencies as well as high-temperature. Packaging researches aims to reduce thermo-mechanical strains and stresses to improve the device reliability. Thus, emerging power semiconductor devices are expected to operate under higher junction temperature, faster switching frequencies and significantly improved reliability ratings (Chung et al., 2015).

For field applications, power semiconductor devices are expected to last

5 up 30 years (Wang et al., 2014). Thus, it is impracticable to wait for real experience data to provide lifetime expectations for new technologies. Moreover, manufacturers must provide warranties before new products launch. Therefore, accelerated power cycling and temperature cycling tests are a common practice among manufacturers to predict components lifetime. These tests are performed to accelerate wear out process and identify the most common failures and theirs stressors. In addition, significant data from accelerated tests can be used to trigger wear out mechanisms and develop lifetime models (Choi; Jørgensen; Blaabjerg, 2016; Zeng et al., 2019). The IEC 60747-9 and IEC 60747-34 define endurance and reliability test setups for semiconductor devices (IEC 60747-34, 2004; IEC 60747-9, 2019).

2.1.1 Most dominant failure mechanisms in power semiconductor devices

The most used power semiconductor devices in power electronic converters employed in photovoltaic systems are MOSFETs (Metal Oxide Semiconductor Field Effect Transistor), IGBT (Insulated-Gate Bipolar Transistor) and diodes. Fig. 2.1 shows the internal structure of a discrete IGBT component with freewheeling diode, connected through bond wires. $R_{th,j-c}$, $R_{th,c-h}$ and $R_{th,h-a}$ are the thermal resistances from junction to case, case to heatsink and heatsink to ambient (Callegari et al., 2019). These thermal resistances describe how the heat flow from each layer of the component and they are crucial in thermal loading assessments.

Generally, in power semiconductor modules, the silicon chip is soldered to a direct-bonded-copper (DBC) ceramic substrate and it is soldered to a metal baseplate (cooper). The baseplate is attached to the heatsink by means of a thermal grease to improve the thermal contact and heat flow. In discrete components, the silicon chips are usually soldered directly to the cooper (often connected to collector pin). In this case, a thermal interface material (TIM) is used to provide better thermal performance, such as mica sheets. In both packages, the internal connections are made of bond wires (IGBT to diode, substrate to silicon chip and output connections). Usually, soft solders such as tin-silver, indium or tin-lead are employed. In addition,
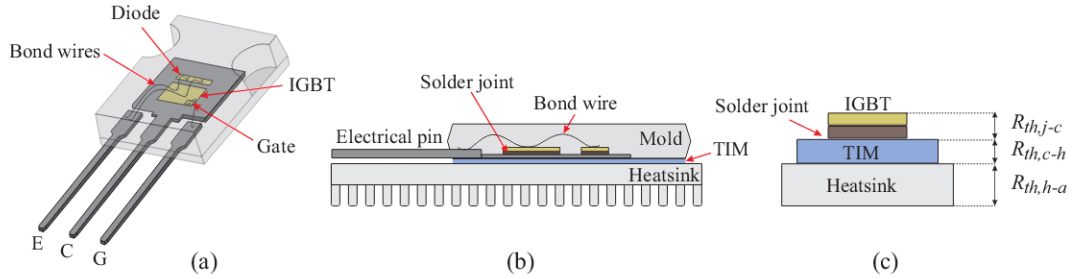
Figure 2.1: Internal structure of a TO-247 package IGBT with freewheeling diode: (a) 3D image showing the internal bond wire connections, (b) cross-sectional view of the chip layers and (c) thermal resistances from each internal layer.

the bond wires are commonly made of aluminum (Pedersen; Pedersen, 2012). Fig. 2.2 shows the internal structure of one module IGBT(Fig. 2.2(a)) and a TO-247 discrete IGBT (Fig. 2.2(b)). The internal structure of the power semiconductor device is composed of materials with different coefficients of thermal expansion (CTE). Therefore, the most predominant failures are related to thermo-mechanical stresses between layers with mismatched CTE (Chung et al., 2015).
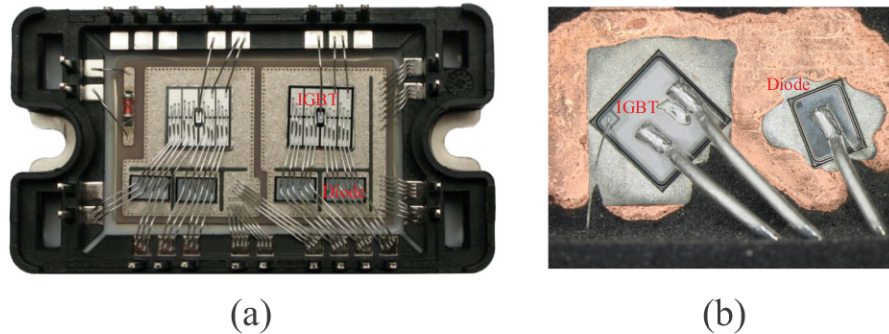
Figure 2.2: Internal structure of power semiconductor device: (a) Half-bridge IGBT module, available on Rashed et al. (2013) and (b) TO-247 discrete IGBT with freewheeling diode, available on Zeng et al. (2018a).

The failures in the power semiconductor devices can be classified in two categories: catastrophic failures, due to a single-event overstress such as overvoltage, overcurrent or overheat; and wear out failures, related to thermo-mechanical stresses, causing accumulated degradation with the time

(Wu et al., 2013). The two most dominant failure mechanisms due to wear out are solder joint fatigue and bond wire fatigue.

The solder joint fatigue root-cause is the formation and accumulation of microdefects (fractures, delamination and voids) in the solder alloy (Huang; Mawby, 2013; Hartmann et al., 2010). The microfissures are caused by CTE mismatch between the layers (silicon chips and DBC or DBC and baseplate). The solder joint fatigue increases the power semiconductor junction-to-case thermal resistance, triggering other thermo-mechanical failure mechanisms and leading the device to failure (Hu; Du; Wei, 2017).

Under PV applications, the device junction temperature ΔT_j swings at relatively low level ($\Delta T_j < 40$ °C). In this temperature cycling range, the solder joint fatigue may not represent relevant impacts on the device if compared to bond wire fatigues (Choi; Blaabjerg, 2018). However, during catastrophic events, the power semiconductor device may experience high junction temperature variations, leading to solder joint fatigues. Moreover, in high-power density electronic applications, such as solid-state circuit breakers and Electromagnetic Aircraft Launch Systems (EMALS), the power semiconductor device is submitted to high junction temperature in a short time (tens of milliseconds). Under such conditions, the analysis of solder joint fatigue related to the thermal resistance is mandatory in reliability analysis (Sommer et al., 2006). Fig. 2.3 shows an IGBT chip solder edge delamination and cracks taken by scanning acoustic microscope (SAM).

(a)   (b)
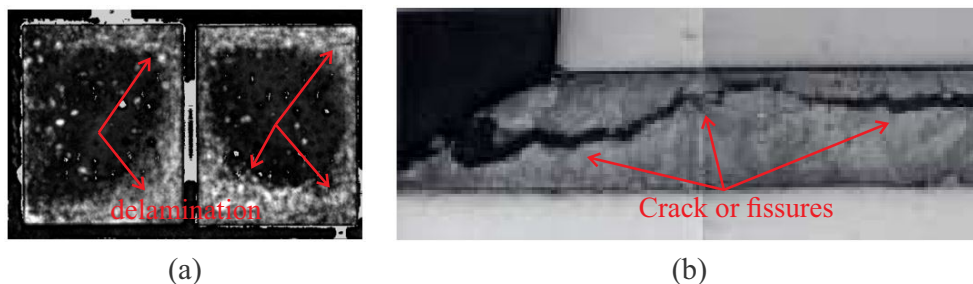
Figure 2.3: SAM images of an IGBT chip solder: (a) upper view of chip solder edge delamination, available on Schilling et al. (2012) and (b) cross section of the solder crack propagation, available on Morozumi et al. (2001).

Similarly to solder joint, the bond wire fatigues are also induced by thermo-mechanical stresses. The primary mechanisms are bond wire lift-off and heel cracking (Ramminger; Türkes; Wachutka, 1998). Highest stress are normally observed in the bonding pad, where the wire is inflexible and suffer higher strain. Due to CTE mismatch, the bond wire is constantly submitted to plastic deformation during power cycling. The cumulative degradation on the bond wires causes an increase in the on-state chip voltage $v_{ce,on}$. Fig. 2.4 presents a scanning acoustic microscope photo of bond wire indicating the lift-off and heel crack.

(a)   (b)
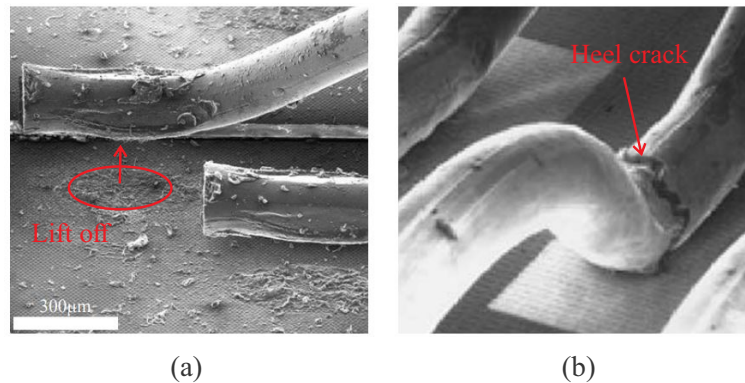
Figure 2.4: SAM images of an IGBT: (a) bond wire lift-off and (b) bond wire heel crack, both available on Ciappa (2002).

Several packaging strategies have been carried out during the past years to reduce bond wire fatigues. Different assembly methods such press pack designs and integrated systems have been tested (Takao; Kyogoku, 2015; Guth et al., 2010). Likewise, different material wires are proposed to replace aluminum, such as cooper, gold and silver (Hu, 2012). However, issues related with design, cost and assembly procedures still makes aluminum most commonly used.

References Choi e Blaabjerg (2018) and Choi, Blaabjerg e Jørgensen (2018) propose methods for separately monitoring and evaluating bond wire and solder joint fatigues in power semiconductor devices during power cycling tests. During these tests, failure criteria are defined to decouple different failure modes and generate distinct data for lifetime models. In PoF-based reliability analysis, it is very important to have separately lifetime models for each failure mechanisms. Thus, it is possible to identify the critical and

weak points of a component and how to address improvements to increase their reliability. Typically, the failure criteria applied to bond wire fatigues are detected by the increase of 5-20% of the drop in the on-state voltage $v_{ce,on}$. Likewise, an increase in 20-50% of junction-to-case thermal resistance are used as indicator of solder joint failure criterion (Chung et al., 2015).

2.1.2   Power semiconductor thermal modeling

The main fatigues of power semiconductor devices are driven by thermo-mechanical stresses and the junction temperature is one of the most dominant stressor. Thereby, the first step to evaluate power semiconductor lifetime is to convert the field operation power losses into thermal loading by means of an electro-thermal circuit. The IGBT power losses can be calculated as follows:

$$P_{loss,IGBT} = P_{c,IGBT} + P_{sw,IGBT}, \qquad (2.1)$$

$$P_{c,IGBT} = \frac{1}{T} \int_{t_0}^{t_0+T} v_{ce} i_c(t) dt, \qquad (2.2)$$

$$P_{sw,IGBT} = f_{sw} \left(E_{on} + E_{off} \right), \qquad (2.3)$$

where $P_{c,IGBT}$ and $P_{sw,IGBT}$ are conduction and switching power losses, respectively; t_0 is a given start time and T is the period of the signal, v_{ce} and i_c are the collector-emitter voltage and collector current, respectively, f_{sw} is the switching frequency, E_{on} and E_{off} are the turn-on and turn-off energies, respectively. Similarly, the diode power losses can be determined as follows:

$$P_{loss,diode} = P_{c,diode} + P_{sw,diode}, \qquad (2.4)$$

$$P_{c,diode} = \frac{1}{T} \int_{t_0}^{t_0+T} v_f i_f(t) dt, \qquad (2.5)$$

$$P_{sw,diode} = f_{sw}E_{rec}, \tag{2.6}$$

where v_f and i_f are the forward voltage and current, respectively and E_{rec} is the reverse recovery energy. The turn-on energy can be neglected in the diode.

It is important to remark that v_{ce} is function of the IGBT collector current i_c, gate-emitter voltage v_{ge} and chip junction temperature $T_{j,IGBT}$. Similarly, v_f is function of the diode forward current i_f and chip junction temperature $T_{j,diode}$. On the other hand, the IGBT switching energies E_{on} and E_{off} are function of the IGBT collector current i_c, gate resistor r_g, collector-emitter blocking voltage v_{ce} and chip junction temperature $T_{j,IGBT}$. Finally, the diode reverse recovery energy E_{rec} is function of the IGBT diode forward current i_f and chip junction temperature $T_{j,diode}$.

The semiconductor junction temperature can be estimated from the the power losses. For such, thermal simulations are of special interest since direct junction temperature measurements inside the chips during operation are still hard to obtain. Fig. 2.5 shows an electro-thermal circuit proposed by Ma et al. (2015). The multi-layer Foster and Cauer thermal networks are used to model the transient response until steady-state condition. Both thermal models return the junction-to-case temperature thermal impedance Z_{th}. Despite representing the same transient, Cauer model has physical interpretation and its pair of thermal resistance R_{th} and capacitance C_{th} can be directly associated with the power semiconductor internal layers. On the other hand, Foster model corresponds to a curve fitting of the thermal transient response in time. The advantage of using Foster model is to provide a straightforward analytical expression of Z_{th} as (Drofenik; Kolar, 2003):

$$Z_{th}(t) = \sum_i R_{th,i}\left[1 - exp\left(\frac{-t}{\tau_{th,i}}\right)\right], \tag{2.7}$$

where $\tau_{th} = R_{th}C_{th}$ and i is the number of nodes in the Foster network. The thermal impedance can be found in device part number datasheet, usually given in Foster format.
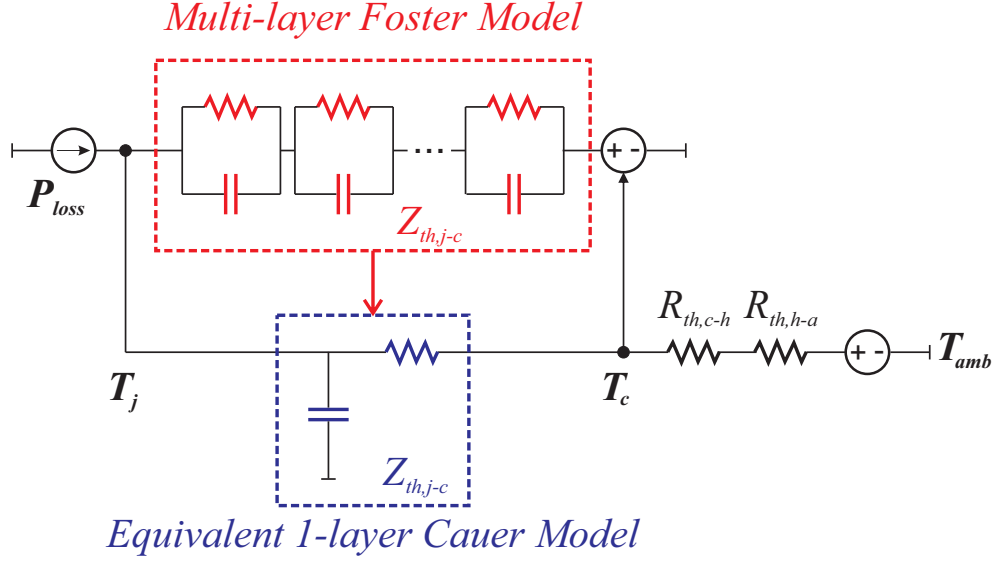
Figure 2.5: Electro-thermal circuit to estimate junction temperature in function of Foster and Cauer networks. *Adapted from Ma et al. (2015).*

In the PV inverter applications, the power semiconductor devices are submitted to different thermal cycling caused by the fundamental frequency (short-cycles) and ambient temperature variations (long-cycles) (Tseng; Wu, 2013). In both cases, the junction temperature variation ΔT_j, also called as cycling temperature, is responsible for strains and stresses in the power semiconductor devices. For short-cycles, data acquisition with sample rates in the range of fundamental frequency would be needed and an enormous amount of data would be collected for long-time operation profiles (such as one-year mission profiles). Alternatively, Ma e Blaabjerg (2012) proposes an analytical equation to find ΔT_j for one fundamental cycle of the fundamental frequency f_0, as given by:

$$\Delta T_j = P_{loss} \left[Z_{th} \left(\frac{1}{8f_0} \right) + 2 Z_{th} \left(\frac{1}{4f_0} \right) \right], \tag{2.8}$$

where P_{loss} are the power losses dissipated on the power semiconductor device. This methodology considers the short-cycle is ΔT_j constant and repeats $f_0 T_s$ times during the mission profile sample period T_s. Due to mission profile irregularity, the thermal loading long-cycles are also irregular and they are not directly applicable to lifetime models. Therefore, counting

algorithms such as Rainflow must be applied to find regular cycles before computing the lifetime evaluation (Mainka; Thoben; Schilling, 2011; GopiReddy et al., 2015; ASTM, 2017).

The thermal design of the heatsink is also of interest. In power electronic converters, the power semiconductors can have one separated heatsink for each component or they can be arranged in the same heatsink, sharing a common thermal network. In this work, there will be only one heatsink for all power semiconductor devices. Under steady-state conditions, the maximum heatsink thermal resistance $R_{th,h-a,max}$ can be defined from Fig. 2.5 as (Christen; Stojadinovic; Biela, 2017):

$$R_{th,h-a,max} = \frac{T_{j,max} - P_{loss,dev}(R_{th,j-c} - R_{th,c-h}) - T_{amb}}{P_{loss,tot}}, \qquad (2.9)$$

where $P_{loss,dev}$ and $P_{loss,tot}$ are the power losses dissipated in the individual device and total in the heatsink, respectively. The heatsink is designed to keep the maximum junction temperature under 120 °C, a safety approach considering long-operation mission profiles.

2.1.3   Power semiconductor lifetime models

There are two types of lifetime models in the literature: empirical and physics-based lifetime models (Yang; Agyakwa; Johnson, 2013). Empirical models derive from accelerated power cycling tests and statistical analysis of a large database and experience obtained over many years. The drawback of empirical models is the need of separated models for each failure mechanisms (i.e., bond wire fatigue and solder joint fatigue) and the imprecision to extrapolate predictions out of the parameters range (Schmidt; Zeyss; Scheuermann, 2013). On the other hand, physics-based lifetime models computes multi-domain failure mechanisms and provide a more realistic lifetime prediction. However, complex implementation and the lack of physics-based lifetime modeling in the literature makes empirical models most commonly used among reliability engineers (Chung et al., 2015). More information about physics-based lifetime models can be found in Kovačević, Drofenik e Kolar (2010), Steinhorst, Poller e Lutz (2013).

The empirical models for lifetime evaluation are expressed in terms of number of cycles to failure N_f. Accelerated power cycling tests are performed to correlate the N_f dependence with lifetime parameters, such as junction temperature, heating periods, voltage, current and chip technology. The most used empirical models for bond wire lift-off lifetime analysis in the literature are stated below:

- *Coffin-Mason model*: The simplest lifetime model is based on Coffin-Mason strain law under plastic regime. In this model, only the junction temperature variation ΔT_j is taken in account:

$$N_f = A(\Delta T_j)^{\beta}, \qquad (2.10)$$

  where A and β are curving fitting parameters, estimated either by numerical simulations or provided by experimental measurements of real devices (Ciappa, 2002). Despite being simple, Coffin-Mason lifetime model is the basis of almost every empirical lifetime models avaiable in the literature:

- *Arrhenius model*: The Coffin-Mason model is improved with the influence of the mean junction temperature T_{jm} (Cui, 2005). Thus, the Arrhenius function is added to Eq. (2.10):

$$N_f = A(\Delta T_j)^{\beta} exp\left(\frac{E_a}{k_b T_{jm}}\right), \qquad (2.11)$$

  where E_a is the activation energy and k_b is the Boltzmann constant.

- *Norris-Landzberg model*: Another extension of Coffin-Mason model, Norris e Landzberg (1969) introduced the dependence of N_f with the thermal cycling frequencies f_c:

$$N_f = A(\Delta T_j)^{\beta_1} f_c^{\beta_2} exp\left(\frac{E_a}{k_b T_{jm}}\right). \qquad (2.12)$$

  Again, β_1 and β_2 are fitting parameters. This model was frequently used in the industry field to determine acceleration factors between different stress conditions (Syed, 2010).

- *Bayerer model*: Bayerer et al. (2008) developed a purely statistical lifetime model based on more than 150 accelerated power cycling tests, covering several different Infineon package designs. Thus, Bayerer model added chip technology information to previous lifetime models, such as current per bondfoot I_b, blocking voltage class V and bond wire diameter D:

$$N_f = A(\Delta T_j)^{\beta_1} exp \left(\frac{\beta_2}{T_{jm} + 273} \right) (t_{on})^{\beta_3} I_b^{\beta_4} V^{\beta_5} D^{\beta_6}, \qquad (2.13)$$

where β_i, $i = 1$ to 6, are curve fitting parameters. Also, t_{on} is the load pulse duration. The Bayerer model is widespread in the literature, also known as CIPS08, referring to the 5th International Conference on Integrated Power Electronics Systems in which it was published.

- *Scheuermann model*: Similarly to Bayerer model, Scheuermann, Schmidt e Newman (2014) proposed a lifetime model based on power cycling tests performed on Semikron SKiM63 power module family. The SKiM63 are 1200 V solder free chips, where a diffusion silver (Ag) sinter technology is applied for die attachment. Moreover, the bond wires are made of aluminum (Al) with 300 μm diameter (Scheuermann; Beckedahl, 2008):

$$N_f = A(\Delta T_j)^{\alpha} exp \left(\frac{E_a}{k_b T_{jm}} \right) (ar)^{\beta_0 + \beta_1 \Delta T_j} \left(\frac{C_d + (t_{on})^{\gamma}}{C_d + 1} \right) f_d, \quad (2.14)$$

where A, α, β_0, β_1, γ and C_d are curve fitting parameters. Additionally, this model includes the influence of bond wire aspect ratio ar in the lifetime estimation. Moveover, one of the greatest advantages of Scheuermann model is the possibility to evaluate both IGBT and diode lifetime using the same equation. For such, the parameter f_d must be 1 for IGBT and 0.6204 for diodes.

Apart from bond wire lift off lifetime models, there is also a very common model for large solder joint fatigue evaluation on power semiconductors, also based on Coffin-Mason power law, defined as :

$$N_f = \frac{1}{2} \left(\frac{\Delta\alpha_s \Delta T_j L_s}{\gamma_s x_s} \right)^{c_s^{-1}}, \qquad\qquad (2.15)$$

where L_s is the lateral size of the solder joint, $\Delta\alpha_s$ is the mismatched CTE between upper and lower layer, ΔT_j is the temperature cycling, c_s is the fatigue exponent, x_s and γ_s are the thickness and the ductility factor of the solder, respectively (Ciappa, 2002). The analysis of Eq. (2.15) implies that fatigue on solder joint can be minimized from device design, e.g., reducing the size of solder joint or applying materials with closer CTE.

Scheuermann and Bayerer are the most complete and widespread employed empirical lifetime models for bond wire lift off in the literature. However, the applicability of these equations is not straightforward, since the thermal loading are not the only information required. Both models are dependent on the chip internal structure, such as number of bondfeet or bond wire aspect ratio, as shown in Fig. 2.6. Moreover, power module manufactures usually do not provide these information, since they are confidential and restrict. Therefore, it is important to ensure these parameters do not deviate from the range of values in which the accelerated power cycling tests were performed. Tab. 2.1 and 2.2 present Scheuermann and Bayerer lifetime model parameter and its range of values, respectively.

(a)   (b)
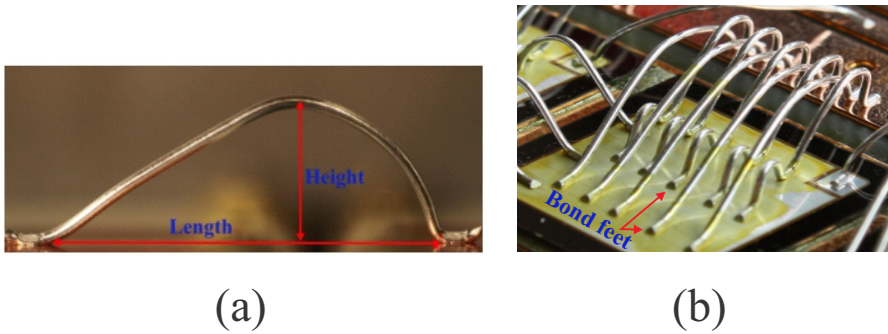
Figure 2.6: Lifetime models required chip information: (a) Scheuermann lifetime model requires bond wire aspect ratio, defined as $ar = H_{ar}/L_{ar}$; (b) Bayerer lifetime model requires number of bond wires, number of bondfeet and bond wire diameter. Images available on Dagdelen, Abdel-Rahman e Yavuz (2018) and Johnson e Hartmann (2015).

For the sake of comparison, Fig. 2.7 shows the number of cycles to

Table 2.1: Parameters of Scheuermann lifetime model for power semiconductors (Scheuermann; Schmidt; Newman, 2014).

Parameter	Value	Experimental Condition
A	2.4368×10^{14}	-
α	-4.923	$64K \leq \Delta T_j \leq 113K$
β_1	-9.012×10^{-3}	-
β_0	1.942	$0.19 \leq ar \leq 0.42$
C_d	1.434	-
γ	-1.208	$0.07s \leq t_{on} \leq 63s$
f_d	0.6204	-

Table 2.2: Parameters of Bayerer lifetime model for power semiconductors (Bayerer et al., 2008).

Parameter	Value	Experimental Condition
A	9.34×10^{14}	-
β_1	-4.416	$45K \leq \Delta T_j \leq 150K$
β_2	1285	$20°C \leq T_{jm} \leq 120°C$
β_3	-0.463	$1s \leq t_{on} \leq 15s$
β_4	-0.716	$3A \leq I_b \leq 23A$
β_5	-0.761	$6V \leq V/100 \leq 33V$
β_6	-0.5	$75\mu m \leq D \leq 500\mu m$

failure of an Infineon discrete IGBT with freewheeling diode (part number IKW40N60DTP), rated at 40 A and 600 V. The N_f is calculated using both Bayerer and Scheuermann lifetime models, for a constant thermal loading, i.e., $T_{jm} = 100 °C$, $\Delta T_j = 80 °C$ and $t_{on} = 10$ s. These values are within the parameters range that the models were tested, defined in Tab. 2.1 and 2.2.

For Bayerer model, as the number of bond wires or bondfoot increases, the current per bondfoot is reduced, reflecting in higher N_f. The bond wire diameter also impacts the lifetime, since thicker wires are submitted to higher strains in the solder interface. However, the dependence of N_f with D cannot be decoupled from the rated current, since higher power modules should have thicker bond wires. On the other hand, Scheuermann lifetime model may seems to be simpler, since only the aspect ratio is required, apart from thermal loading parameters. As ar increases, the number of cycles to failure in the Scheuermann model also increases, since more mechanical strain is
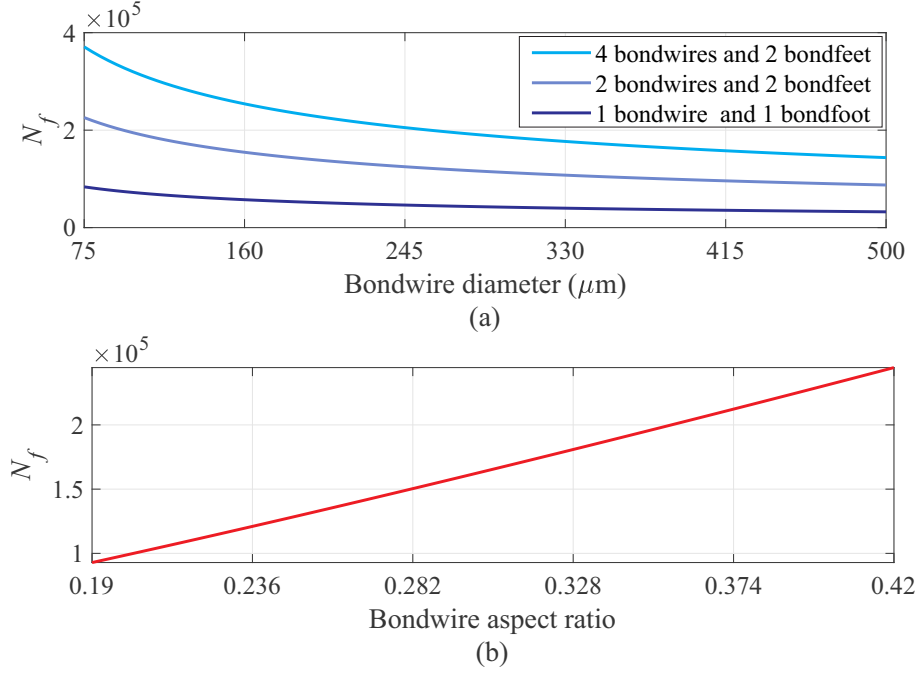
Figure 2.7: Required chip information by lifetime models, using thermal loading
parameters of $T_{jm} = 100\,°C$, $\Delta T_j = 80\,°C$ and $t_{on} = 10$ s.: (a) Bayerer
lifetime model requires number of bond wires, number of bondfeet and
bond wire diameter, (b) Scheuermann lifetime model requires bond
wire aspect ratio, defined as $ar = H_{ar}/L_{ar}$.

needed to lift off the bond wire.

The thermal loading parameters used to calculate the number of cycles to
failure in Fig. 2.7 derive from accelerated power cycling tests. This condition
does not represent a common PV inverter thermal loading caused by the
fundamental frequency variation. Therefore, Fig. 2.8 shows the same IGBT
part number, submitted to a thermal loading of $T_{jm} = 100\,°C$, $\Delta T_j = 20\,°C$
and $t_{on} = 1/120$ s.

Note that the used thermal loading parameters are now extrapolated
from the model parameter range defined in Tab. 2.1 and 2.2. Under such
condition, the models output different values of number of cycles to failure
when submitted to the extrapolated thermal loading. Despite being
different, both models can be applied to a power semiconductor device
when it is submitted to a specific condition and compared to traditional
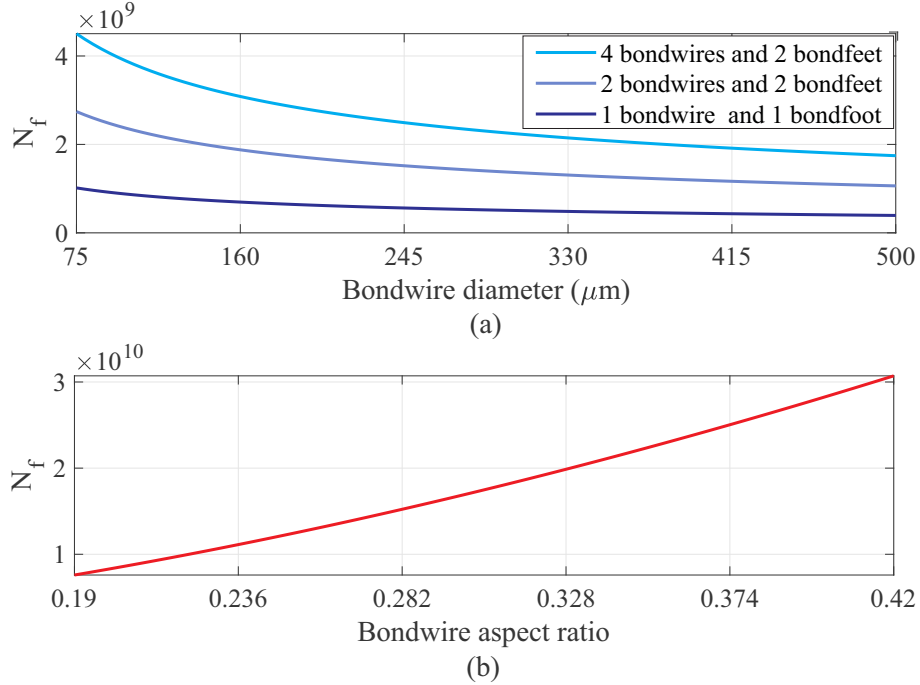
Figure 2.8: Required chip information by lifetime models, using thermal loading parameters of $T_{jm} = 100\ °C$, $\Delta T_j = 20\ °C$ and $t_{on} = 1/120$ s: (a) Bayerer lifetime model requires number of bond wires, number of bondfeet and bond wire diameter, (b) Scheuermann lifetime model requires bond wire aspect ratio, defined as $ar = H_{ar}/L_{ar}$.

operation. Therefore, the main goal of using lifetime models in this thesis is not to exactly predict the lifetime, but to evaluate the effects of reactive power compensation in the case study, when comparing it to conventional PV inverter operation.

In the following analysis, the lifetime evaluation of power electronic devices will be carried out using Bayerer's bond wire lift off lifetime model. The reason of choosing this instead of Scheuermann's model is the wider range of power devices used in the power cycling tests for the model development. In addition, since the selected IGBT used in the case study are manufactured by Infineon, it is reasonable to choose Bayerer's model as well. The drawback of using Bayerer's model is the unavailability of evaluating the diode lifetime, since this model was only tested for IGBTs. However, previous studies in the literature already demonstrated that the

damage on the diode is way lower than damage on the IGBTs, even during reactive power compensation (Anurag; Yang; Blaabjerg, 2015; Callegari et al., 2019). Therefore, it is reasonable to assume that the IGBT fails earlier and the PV inverter lifetime is not limited by the diodes failures.

Recent studies have demonstrated that the Bayerer lifetime parameters, obtained from accelerated power tests, may not be valid for real applications. Zeng et al. (2019) proposes experimental results to obtain the lifetime parameters using accelerated tests with load pulse duration in the range of 10 ms. Lutz et al. (2020) provides first experimental validation of accelerated power tests with temperature swing below 30 K. In addition, Zeng et al. (2018b) developed a new lifetime model for discrete power devices, since the Bayerer lifetime model was obtained from tests with power modules only. Despite the efforts of these authors to improve the lifetime model for a wider range of device applications, the results are still premature. Therefore, this thesis will use the original Bayerer lifetime model.

Finally, the Palmgren-Miner's rule of linear cumulative damage can be used to compute the power semiconductor lifetime consumption, given by (Palmgren, 1924; Miner, 1945):

$$LC_s = \sum_i^m \frac{1}{N_{fi}}, \qquad (2.16)$$

where LC_s is the IGBT lifetime consumption evaluated over m mission profile points (Huang; Mawby, 2013).

The linear cumulative damage proposed by Palmgren and popularized by Miner was initially developed for mechanical applications. Recently Zeng et al. (2019) validated this theory with experimental investigation to compute power semiconductor damage due to electro-thermo-mechanical stresses. According to them, the linear cumulative damage is a very conservative approach that works fine when the same heating time t_{on} is considered. Otherwise, it might lead to slightly different thermo-mechanical stresses regarding impact scale inside the power semiconductors. Additionally, Edwards (1969) showed that the Palmgren-Miner's rule can give an inaccurate estimate of the lifetime of aluminum alloy under variable

junction temperature variation. Therefore, the literature presents some non-linear accumulative damage models (Zhang et al., 2018; Zhu et al., 2019). Howeve, in PV inverter applications, the most relevant thermal cycles are the short-cycles, which contain well-defined heating time equal to $1/2f_0$. Thereby, this thesis considers Palmgren-Miner's rule to compute the PV inverter components damage.

2.2 Capacitors reliability analysis

Capacitors are widely used in PV inverter dc-links to balance the power difference between the input source and output load. In the case of a two-stage PV inverter, capacitor banks are also used as an interface between the PV modules and the dc-dc boost converter (Wang; Blaabjerg, 2014). Besides being a major contributor in terms of converter overall cost and volume, capacitors are also one of the most failure-prone elements in the PV inverter (Wang; Zhou; Blaabjerg, 2013; Wang et al., 2016).

Nowadays there are three main types of capacitors used for dc-link applications: aluminum electrolytic capacitors (Al-Caps), metallized polypropylene film capacitors (MPPF-Caps) and high capacitance multi-layer ceramic capacitors (MLC-Caps). Each type of capacitors has specific advantages and shortcomings, detailed in Wang e Blaabjerg (2014). Aluminum electrolytic capacitors can achieve higher capacitance and energy density with the lowest cost per joule. However, it suffers with wear out issues under electro-thermal stresses. Multi-layer ceramic capacitors have smaller size and can be used in a wider range of frequency at higher operating temperatures. However, they have the highest cost and suffer with mechanical sensitivity. Finally, the film capacitors presents high voltage capability and lowest ESR (Equivalent Series Resistance), at the cost of larger volume and lower operating temperature. Tab. 2.3, provided by Chung et al. (2015), summarizes the performance comparison of the three types of capacitors used for dc-link applications.

In terms of reliability, the design of capacitors applied to dc-link applications faces some challenges, such as operation under minimum design margin due to cost reduction and exposition to more harsh

Table 2.3: Performance comparison of three types of capacitors for dc-link applications. Symbol +++ means good, ++ medium and + bad (Chung et al., 2015).

Parameter	Al-Caps	MPPF-Caps	MLC-Caps
Capacitance	+++	++	+
Voltage	++	+++	+
Volume	++	+	+++
Ripple current	+	+++	+++
ESR	+	+++	+++
Frequency range	+	++	+++
Capacitance stability	++	+++	+
Overvoltage capability	++	+++	+
Temperature range	++	+	+++
Energy density	+++	+	++
Useful life	+	+++	+++
Cost per joule	+++	++	+

environments. To overcome these constraints, the academia and industry focus on improving capacitor technology, designing optimal dc-link solutions and implementing monitoring conditions to ensure reliable operation (Chung et al., 2015).

2.2.1   Most dominant failure mechanisms in dc-link capacitors

In general, due to cost benefit, the electrolytic capacitors are the most used in PV inverter dc-link applications. Average temperature, operating voltage and current levels are the most critical stress factors that accelerate wear out degradation in these components. The electrolyte vaporization and electrochemical reaction are the dominant failure mechanisms of aluminum electrolytic capacitors, reducing the capacitance, increasing the leakage current and ESR (Wang; Blaabjerg, 2014; Xue et al., 2016). Several monitoring methods based on the value of ESR and capacitance are proposed in order to predict possible failure events in the capacitors (Ahmad; Agarwal; Anand, 2016; Agarwal et al., 2016).

In MPPF-caps, mechanical vibration is one of the most dominant failure mechanisms. After a dielectric breakdown (e.g., due to overvoltage), the

local weak point is isolated from the electrode surface and the capacitor continues to work normally thereafter, due to self-healing process (Sun et al., 2013). As a consequence, the isolated weak points gradually reduce the capacitance until reach the end-of-life criteria. In addition, MPPF-caps suffer with atmospheric humidity, which may lead to the corrosion and degradation of metalized layers (Brown, 2006).

In the case of MLC-caps, the reliability is not often considered as an issue, since these kind of capacitors can operate during thousand of hours without significant wear out (Liu; Sampson, 2012). However, mechanical vibration is an important failure stressor, which can be a problem in embedded systems. Additionally, the catastrophic failures in MLC-caps can be very dangerous once the component fails in short-circuit mode. The most dominant failures in MLC-caps are insulation degradation and flex cracking.

Wang e Blaabjerg (2014) provide a summarized table with the dominant failures mechanisms and most critical stressors, shown in Tab. (2.4). It is possible to note that T_{amb} and the operating voltage V_c are common stressors in all three kind of capacitors. In addition, the failure criteria often used to determine the capacitor end-of-life is given. These information are usually provided by the capacitors manufacturers in the component datasheet, aside with the number of hours under rated conditions L_0. For the sake of comparison, TDK aluminum electrolytic snap-in capacitors (part number B43630) has 2,000 hours of useful life under rated conditions. Likewise, TDK metallized polypropylene film capacitors (part number B32674) has 200,000 hours for the same conditions. In this sense, MPPF-caps have 1 hundred times more the reliability of Al-caps. Nowadays, it is possible to find long-life series of electrolytic capacitors, with useful life ranging from 5,000 to 10,000 hours. Even though, MLC-caps are still more reliable in terms of useful life.

2.2.2 Capacitors thermal modeling

A simple capacitor electrical model is composed of the primary capacitance C, the equivalent series resistance ESR and equivalent series inductance ESL, as shown in Fig. 2.9. ESR represents the power losses of the capacitor (resistance of the dielectric material, connection pins and lead

Table 2.4: Comparison of failure types and critical stressors of three types of capacitors (Wang; Blaabjerg, 2014).

Capacitor type	Dominant failure mechanisms	Most critical stressors	Failure criteria
Al-Caps	electrolyte vaporization, electrochemical reaction	T_{amb}, V_c, I_c	C: 20% reduction ESR: 2 times
MPPF-Caps	moisture corrosion, dieletric loss	T_{amb}, V_c, humidity	C: 5% reduction DF: 3 times
MLC-Caps	insulation degradation, flex cracking	T_{amb}, V_c, vibration	C: 10% reduction DF: 2 times $R_P < 10^7 \Omega$

terminals). Similarly, ESL represents the capacitor inductance of the winding layers and connected power terminals (Wang et al., 2020). Both ESR and ESL are function of the primary capacitance and operating frequency. Thereby, for a given C, the capacitor equivalent impedance in function of frequency can be determined as:

$$Z_{cap}(f) = ESR(f) + j\left(2\pi f ESL - \frac{1}{2\pi f C}\right). \qquad (2.17)$$
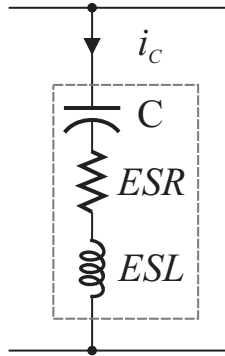
Figure 2.9: Capacitor equivalent electrical circuit model, composed of the primary capacitance C, equivalent series resistance ESR and equivalent series inductance ESL.

The analysis of Z_{cap} in frequency domain has three characteristic regions, as shown in Fig. 2.10: low-frequency region, where there is a predominance

of the capacitive reactance; medium-frequency region at resonant-frequency where the inductance and capacitive reactance cancel themselves and $Z_{cap} = ESR$; and high-frequency region where the capacitor behavior is inductive.
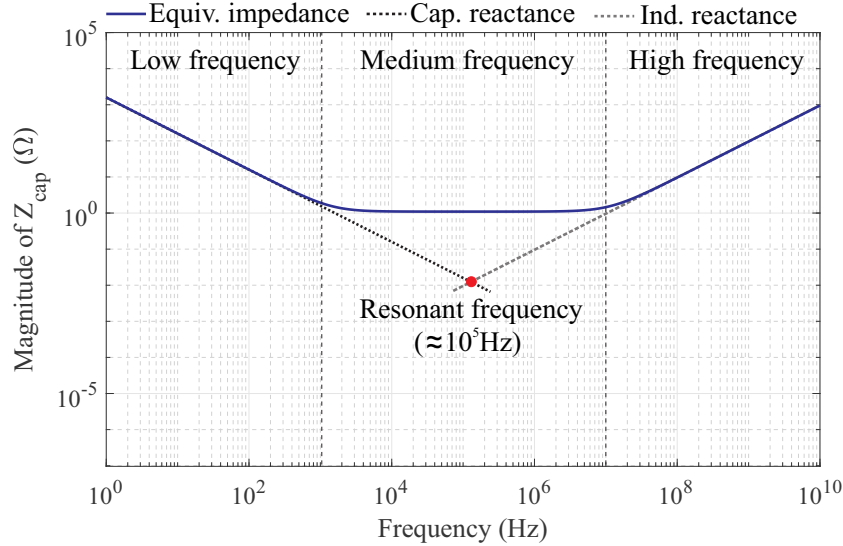
Figure 2.10: Characteristic regions of an 100 μF / 450 V (part number TDK B4360) Al-Cap equivalent impedance curve in function of frequency. Adapted from Wang et al. (2020).

Moreover, capacitor types have different Z_{cap} curves, as shown in Fig. 2.11. In low-frequency region, film capacitors have higher ESR compared to electrolytic capacitors. However, there is a predominance of the capacitive reactance, which makes Z_{cap} almost the same for both curves. In the medium-frequency region (in the range of switching frequency harmonics), film capacitors have lower Z_{cap} when compared to electrolytic capacitors. Therefore, one possibility to minimize power losses on dc-link banks and improve its reliability is to use hybrid solutions, mixing electrolytic with film capacitors (Wang et al., 2020).

Most degradation processes in the capacitors are driven by the increase of internal temperature, also called as hot-spots, due to the power dissipation on ESR. Thus, a thermal model can be derived from the electrical model in which the power losses and capacitor thermal resistance are the main factors. Fig. 2.12 shows the translation from electrical to thermal model. Since ESR is dependent on the frequency, different losses contributions are
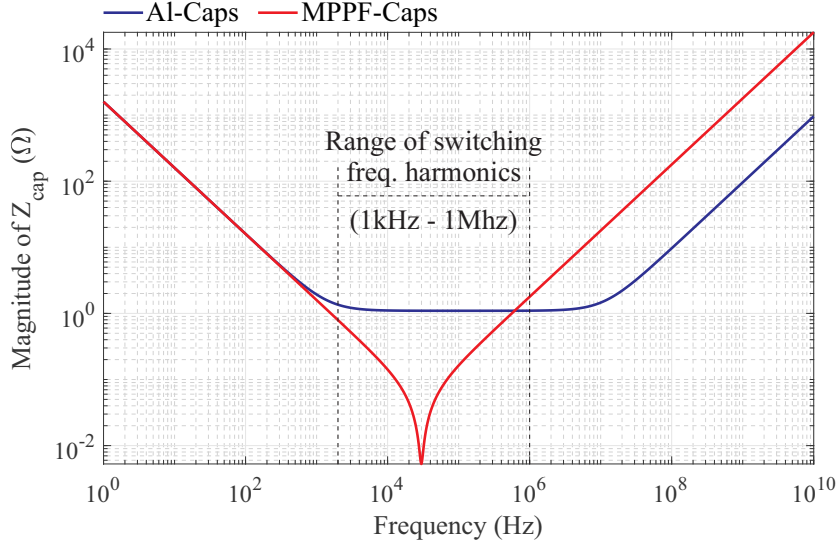
Figure 2.11: Equivalent magnitude impedance comparison of an Al-Cap and MPPF-Cap in function of frequency. In these curves, the Al-Cap is a 100 μF / 450 V (part number TDK B4360) and the MPPF-Cap is a 100 μF / 450 V (part number TDK B32674).

observed for double fundamental frequency (in single-phase PV converters) and switching components. Therefore, an analysis in frequency domain using Fast Fourier Transform (FFT) must be applied to compute the power losses on the capacitor (Yang et al., 2015).
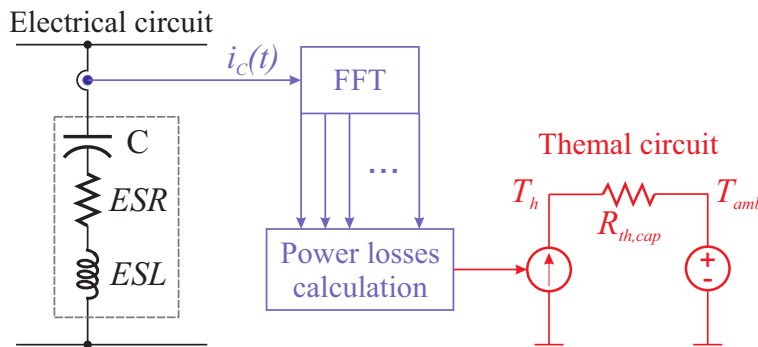
Figure 2.12: Capacitor bank electrical model converted into thermal model through power losses computation using Fast Fourier Transform (FFT).

The capacitor power losses $P_{loss,cap}$ and the hot-spot temperature T_h can

be described as:

$$P_{loss,cap} = \sum_{i}^{h} ESR(T_h, hf) I_{cap,rms}(hf)^2, \qquad (2.18)$$

$$T_h = P_{loss,cap} R_{th,cap} + T_{amb}, \qquad (2.19)$$

where h is the harmonic order of the fundamental frequency f_0 and $R_{th,cap}$ is the capacitor thermal resistance, defined in function of the capacitor dimensions (Wang et al., 2020). The ESR is also function of the hot-spot temperature. Therefore, there is a feedback loop in the calculation of $P_{loss,cap}$ and T_h. The dependence of ESR with frequency and temperature is usually provided by the manufacturers, as shown in Fig. 2.13 for an aluminum electrolytic capacitor manufactured by TDK (part number B43630).

The electro-thermal circuit in Fig. 2.12 describes well the power losses on electrolytic and film capacitors. However, for certain ceramic capacitors, i.e., class II ceramic capacitors, this model is inadequate. These capacitors can have ultra-high dielectric constants at the cost of non-linear voltage-dependent capacitance value. Therefore, high low-frequency large-signal excitation can cause substantial device heating, which is not computed through the circuit in Fig. 2.12. For this type of capacitors, Menzi, Heller e Kolar (2021) proposes a new normalized Steinmetz model to predict more accurately the power losses on ceramic capacitors.

2.2.3 Capacitors lifetime models

A widely and general used lifetime model for capacitors is described as follows (Wang; Blaabjerg, 2014):

$$L = L_0 \left(\frac{V_c}{V_0}\right)^{-n} exp\left[\left(\frac{E_a}{k_b}\right)\left(\frac{1}{T_h} - \frac{1}{T_0}\right)\right], \qquad (2.20)$$

where L is the capacitor lifetime under the hot-spot temperature T_h and operating voltage V_c. The subscript index 0 denotes the rated values provided
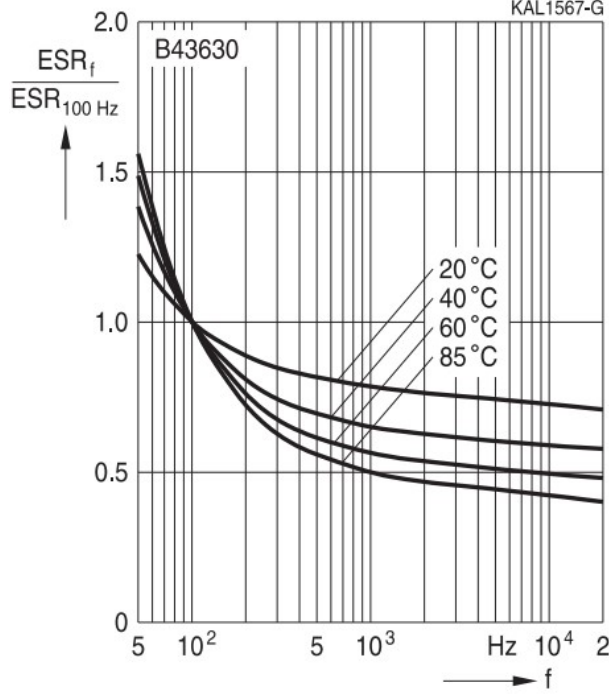
Figure 2.13: Frequency and temperature characteristics of ESR from aluminum electrolytic capacitor part number TDK B43630 (TDK, 2016).

by manufactures. The values of E_a and n are different for each type of capacitors. MLC-caps usually have more dependence with E_a and n, varying from ceramic materials and dielectric layer thickness (Minford, 1982). On the other hand, Al-caps and MPPF-caps lifetime models can be simplified to:

$$L = L_0 \left(\frac{V_c}{V_0} \right)^{-n} 2^{\left(\frac{T_0 - T_h}{10} \right)}, \qquad (2.21)$$

where n ranges from 7 to 9.4 for MPPF-caps and 3 to 5 in Al-caps (Wang; Blaabjerg, 2014). This simplified model assumes a medium voltage stress. For low voltage stress, n can be assumed to 1 and for high-voltage stress, a generic model is proposed in (Wang; Ma; Blaabjerg, 2012). In this work, the simplified model, presented in Eq. (2.21) will be used.

It is noteworthy that the presented lifetime model for dc-link capacitors

only takes into account the stresses caused by temperature and voltage. For Al-caps, the influence of I_{cap} is also accounted in the power losses and hot-spot temperature calculation. However, for MPPF-caps and MLC-caps, other critical stressors such as humidity and vibration are also relevant and not considered in the presented lifetime model.

Finally, the Palmgren-Miner's rule of linear cumulative damage can be used to compute the capacitor lifetime consumption, given by:

$$LC_c = \sum_i^m \frac{L_{m,i}}{L_i},\qquad(2.22)$$

where LC_c is the capacitor lifetime consumption evaluated over m mission profile points (Shao et al., 2014). $L_{m,i}$ is the mission profile sample time in hours, representing the capacitor number of hours in operation between two mission profile consecutive points.

Just like power semiconductors, capacitors also have been investigated for non linear cumulative fatigues due to degradation process (Gupta et al., 2018). There are several degradation models in the literature, mainly related to the aging of ESR or increase in the leakage current (Wang et al., 2019; Chunlin et al., 2020). However, a conservative approach is considered in this thesis, using Palmgren-Miner's rule for linear cumulative damage.

2.3 Mission profile-based reliability analysis with Monte Carlo simulation

The flowchart of the PV inverter reliability is presented in Fig. 2.14. The lifetime consumption of the power semiconductor and capacitor are evaluated separately and then combined to find the system-level reliability by using Monte Carlo simulations.

Initially, to compute IGBT lifetime consumption, the mission profiles are used as inputs of the PV inverter electrical model and the power losses are computed. Then, the power losses are translated to thermal loading by means of the equivalent electro-thermal circuit presented in Fig. 2.5.
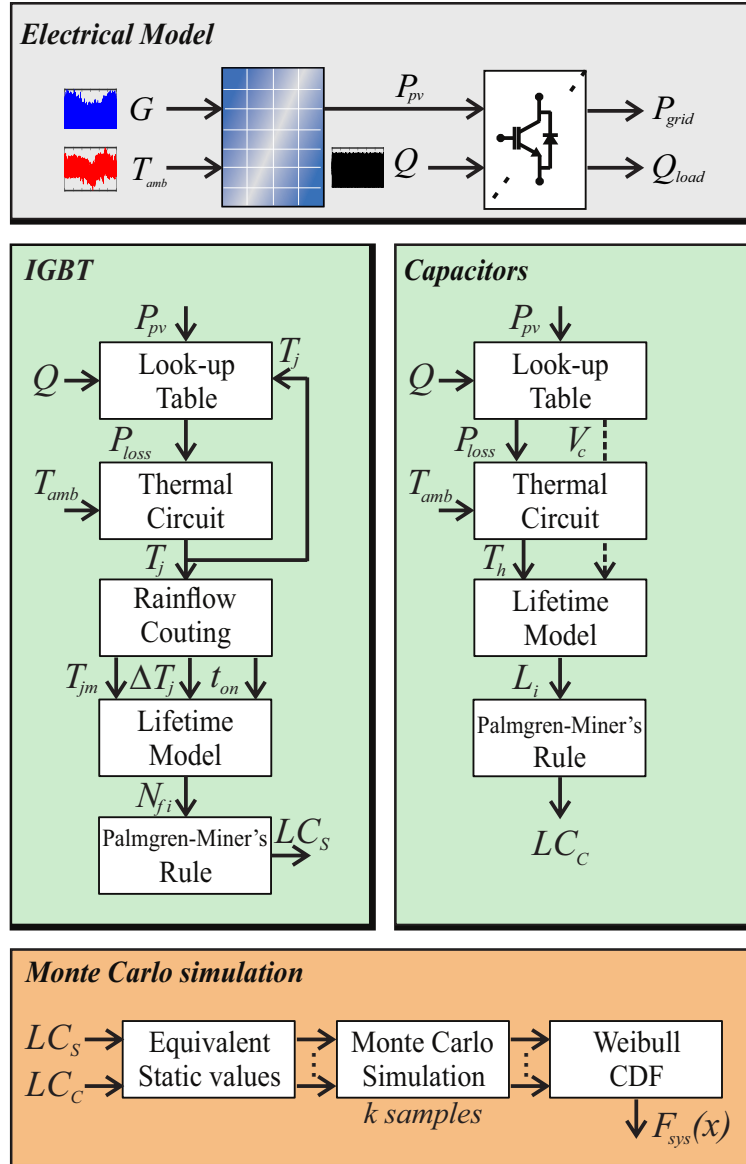
Figure 2.14: Mission profile-based reliability evaluation flowchart:(a) power
            semiconductor lifetime, (b) capacitor lifetime and (c) Monte Carlo
            simulations.

Notably, the translation from the mission profiles into thermal loading is
performed through a look-up table procedure in order to handle long-term
simulations with a set of solar irradiance, ambient temperature and reactive
power conditions. Then, the irregular thermal loading profile must be

converted into regular cycles before being used in the Bayerer lifetime model. The regular cycles are characterized as the mean junction temperature T_{jm}, cycling temperature ΔT_j and cycling period t_{on}. The rainflow algorithm is employed and the parameters are used as inputs of the power semiconductor lifetime. Finally, LC_s is computed under each point of the mission profile.

In the sequence, the capacitor lifetime consumption follows almost the same procedure described above. The power losses are extracted from the electrical model of the PV inverter, via simulations and then used as input of the thermal circuit model. The hot-spot temperature and operating voltage are used as input of the capacitor lifetime model and LC_c is evaluated for each point of the mission profile.

The power semiconductors and capacitors lifetime consumption, given by Eq. (2.16) and (2.22) consider that all similar components in the PV inverter would fail at the same time. In fact, there are parameters variations that should be introduced in the lifetime computing. Therefore, a statistical analysis based on Monte Carlo simulation is performed in order to include the manufacturing process uncertainties and thermal variations in the lifetime consumption evaluation (Reigosa et al., 2016).

The inputs of the Monte Carlo simulation must be arranged in a well-defined probability function, i.e., in a normal distribution. For such, the irregular thermal loading values must be converted into equivalent static values that generate the same lifetime consumption. Thus, the Monte Carlo simulation can be performed with a population of k samples, inserting a specific parameter variation for each component.

Regarding the power devices, the static mean junction temperature T_{jm}' is taken as the mean value of the thermal loading profile. Additionally, the static heating cycle period t_{on}' is fixed as the heating time of the fundamental frequency ($1/120s$), since it is the most stressful cycle in the power device. Finally, $\Delta T_j'$ can be determined, ensuring the same lifetime consumption computed in Eq.(2.16). With respect to the capacitors, the static value of the operating voltage V_c' is fixed as the mean value of the operating voltage long-term profile. This allows the static value of the hot-spot temperature T_h' to be determined ensuring the same lifetime consumption computed in Eq. (2.22).

With all the static parameters obtained for each component, the Monte Carlo simulation can be performed including parameters variations in each component. The thermal loading on the power devices are dependent on the collector-emitter voltage v_{ce}, provided by manufacturers. In addition, the maximum variation of v_{ce} can be found in the datasheet, given an estimation of how the thermal loading parameters ΔT_j and T_{jm} vary as a response of v_{ce}. Finally, the technology factor A is varied up to 20%, representing manufacturing process uncertainties (Reigosa et al., 2016).

In electrolytic capacitors, the thermal stress is caused by the power dissipation on the ESR. Manufactures usually do not provide the maximum variation of ESR. However, as the maximum variation of the capacitance is easily found in the datasheets, the maximum ESR value can be determined considering a constant dissipation factor DF, as follows (TDK, 2019):

$$ESR = \frac{DF}{2\pi f C}. \tag{2.23}$$

Finally, a variation of 20% in the rated useful life L_0 is considered, representing the manufacturing process uncertainties.

The results of the Monte Carlo simulation are arranged in a histogram fitted with the Weibull Probability Density Function (PDF), given by:

$$f(x) = \frac{\mu}{\eta^\mu} x^{\mu-1} exp\left[-\left(\frac{x}{\eta}\right)^\mu\right], \tag{2.24}$$

where μ is the shape parameter, η is the scale parameter and x is the operation time (Sangwongwanich et al., 2018a). Then, the Weibull Cumulative Density Function (CDF) can be evaluated to compute the unreliability function of each individual component, given by:

$$F_{comp}(x) = \int_0^x f(x)\,dx. \tag{2.25}$$

The unreliability function determined by (2.25) correspond to the failure rates in the component level, mainly focused on the mechanism of failure and the failure criteria. To determine the system-level unreliability,

a reliability block diagram based on associations of the component-level functions must be constructed (Yang; Sangwongwanich; Blaabjerg, 2016). There are several methodologies in the literature to do so, such as part-count models, combinatorial models, and state-space models (Song; Wang, 2013). The part-count model is based on the following assumptions:

- any fault that occurs to each of the components or subsystems will cause the overall system to fail;

- at components level, the failure rates of identical components are assumed equal during useful lifetime;

- the system is treated as a series structure of all components or subsystems.

Therefore, the reliability block diagram of all component-level unreliability functions associated in series is presented in Figure 2.15 and the expression of system-level unreliability function is calculated as:

Figure 2.15: Reliability block diagram of system level with unreliability functions in component level associated in series.

$$F_{sys}\left(x\right) = 1 - \prod_{1}^{p}\left(1 - F_{comp,p}\left(x\right)\right), \qquad (2.26)$$

where p is the number of components (power devices and capacitors) in the PV inverter. From Eq. (2.26), it is possible to determinate a commonly used reliability metric, called B_x, referring to the time when $x\%$ of the samples failed (Reigosa et al., 2016).

2.4   Chapter closure

The objective of this chapter is to present the state-of-art of lifetime prediction in power electronic systems. Furthermore, important concepts in the reliability field, such as Physics-of-Failure and Design for Reliability were introduced. These concepts can identify the dominant failure mechanisms and the most critical stressors in the PV inverter components.

In regard to the most stressed components in the PV inverter, the power semiconductors and capacitors lifetime models most used in the literature were presented. The Bayerer lifetime model will be considered for discrete IGBT lifetime evaluation and the simplified model for medium voltage stress will be addressed for capacitor lifetime prediction.

The next chapters of this thesis will apply the discussed lifetime models and reliability analysis to the PV inverter while compensating reactive power. The stresses in the components will be compared to the conventional operation of the converter.

Sensitivity analysis of meteorological variables on the components lifetime

In this chapter the topology of a three-phase two-stage PV inverter with two stages is discussed. The control strategy and parameters are presented as well. In addition, the PV inverter is employed as a case study to investigate the impacts of meteorological variations (solar irradiance and ambient temperature) on the reliability analysis and lifetime prediction. The effects of PV module thermal dynamics are considered in the lifetime evaluation, such as module temperature and equivalent thermal capacitance.

3.1 System topology and control strategy description

The topology of the grid-connected PV inverter analyzed in this work is presented in Fig. 3.1. As observed, the PV inverter is a three-phase converter composed of two stages. The first stage is composed of four identical dc-dc boost converters that perform independent maximum power point tracking (MPPT) of each correspondent connected PV array. In this case, the Perturb and Observe (P&O) algorithm is used to extract the maximum power from the PV modules (Sera et al., 2013). Additionally, the

dc-ac stage is a two-level three-phase inverter, connected and synchronized to the grid by means of a Synchronous Reference Frame Phase-Locked Loop (SRF-PLL) topology (Golestan; Guerrero; Vasquez, 2017). This stage is responsible for injecting active and reactive power into the grid by means of the dc-link voltage control. The dc-ac stage is connected to the grid through a LCL filter to attenuate high frequency harmonics caused by the switching devices (Zou; Wang; Cheng, 2014; Liserre; Blaabjerg; Hansen, 2005). The resistor R_d is used as a passive damping technique to reduce the filter resonant peak at resonant frequency (Gomes; Cupertino; Pereira, 2018).The control strategies employed are detailed in Fig. 3.2 and described in the following subsections.
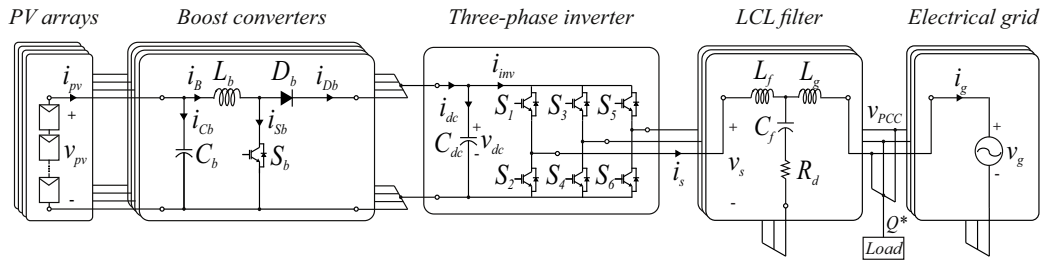
Figure 3.1: Electrical circuit of the investigated two-level three-phase PV inverter with two stages and connected to the grid through a LCL filter. There is a reactive load connected to the point of common coupling (PCC) representing reactive power compensation by the PV inverter.

3.1.1   Dc-dc stage control

The dc-dc stage is composed of four MPPT entries, containing identical boost converters in each input. A phase-shifting strategy is adopted to symmetrically displace angles of the triangular carries in the PWM to reduce the stress on the dc-link capacitor C_{dc} (Pan et al., 2020; Sahu et al., 2016). In addition, the control strategy adopted for all boost converters are the same.

Due to the intermittent characteristic of the solar irradiance, the PV array can work at different voltage levels. Therefore, the P&O algorithm is used to find the maximum power point (MPP) reference voltage v_{pv}^* for every meteorological conditions, i.e., solar irradiance and ambient temperature.

This algorithm has low complexity and computational efforts, being one of the most traditional MPPT methods used in the literature (Drir; Barazane; Loudini, 2014).
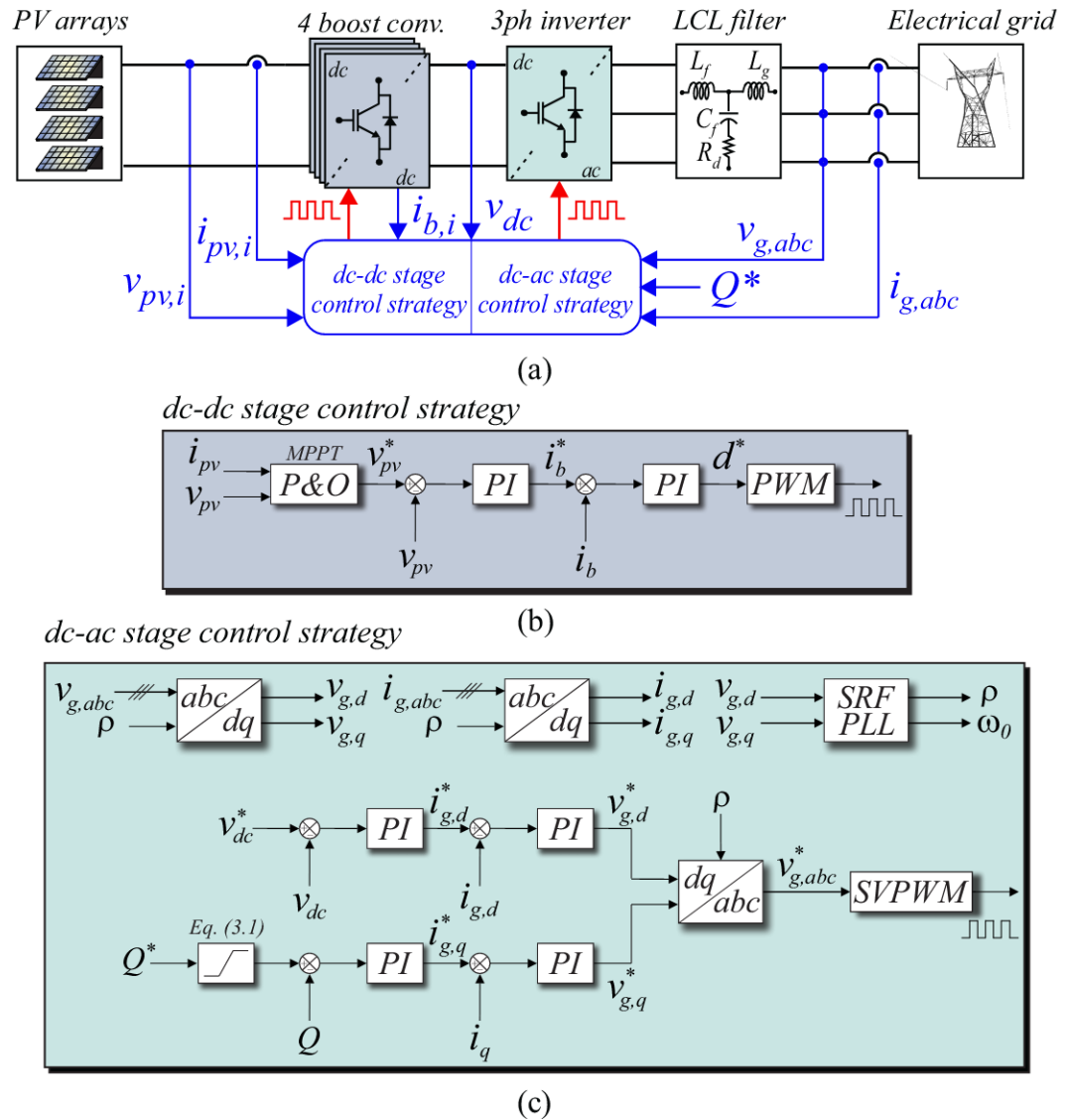
Figure 3.2: Complete control strategy employed to the two stages of the PV inverter: (a) three-phase two-stage inverter topology schematic, (b) dc-dc stage control strategy blocks diagram and (c) dc-ac stage control strategy blocks diagram.

The control strategy of the dc-dc stage converter is composed of two cascade loops: an outer loop to control the voltage v_{pv} on the boost converter input capacitor C_b and an inner loop to control the boost converter inductor current i_b. For each loop, a proportional-integral (PI) controller is applied. The output signal d^* controls the boost converter IGBT S_b state (on or off) by means of a pulse width modulation (PWM).

3.1.2   Dc-ac stage control

The control strategy adopted in this stage is implemented in synchronous reference frame with space vector pulse width modulation (SVPWM). The grid voltage $v_{g,abc}$ in natural reference frame are translated to $v_{g,d}$ and $v_{g,q}$ in rotating reference frame by means of Park's transformation. This strategy allows the use of PI controllers with good accuracy, reduces computational efforts, and allows the PV inverter to independently controls active and reactive power injected to the grid (Bao et al., 2013). In addition, the SVPWM strategy has lower harmonic distortions, wider linear modulation range and better efficiency when compared to sinusoidal PWM (SPWM) (Hava; Kerkman; Lipo, 1999).

The inner loop of grid current in direct axis $i_{g,d}$ determines the injected active power to the grid (assuming inverter operation). This loop is controlled by a voltage outer loop in function of the dc-link voltage reference v_{dc}^*. On the other hand, the inner loop of grid current in quadrature axis $i_{g,q}$ is responsible for injecting/absorbing reactive power depending on the reference Q^* of the reactive power outer loop. It is important to note that the PV inverter cannot process reactive power arbitrarily, due to electrical and thermal constraints. To guarantee a safe operation mode, a dynamic saturation is performed to avoid exceeding the rated power S_n (Xavier; Cupertino; Pereira, 2014). Since the main role of the PV inverter is to inject the active power, determined by the reference P^*, the reactive power reference follows the inequality below:

$$Q^* \leq \sqrt{S_n^2 - P^{*2}}. \tag{3.1}$$

Tab. 3.1 summarizes the calculation of the controller gains based on consolidated methodologies in the literature (Sousa, 2007; Teodorescu;

Liserre; Rodríguez, 2011; Xavier, 2018).

Table 3.1: Controller gains applied to each stage of the PV inverter.

Converter stage	Control loop	Controller gain	Parameter
SRF-PLL	Unique	$k_p = 2\xi\omega_n$ $k_i = \omega_n^2$	$\xi = 0.707$ $\omega_n = \frac{\omega_0}{3}$
dc-dc	Inner	$k_p = -2\pi f_{cib} L_b$ $k_i = -2\pi f_{cib} R_b$	$f_{cib} = \frac{f_{sw}}{20}$
	Outer	$k_p = -2\pi f_{cvb} C_b$ $k_i = -2\pi f_{cvb} \frac{1}{R_{mp}}$	$f_{cvb} = \frac{f_{sw}}{200}$
dc-ac	Inner	$k_p = 2\pi f_{ci} L_t$ $k_i = 2\pi f_{ci} R_t$	$f_{ci} = \frac{f_{sw}}{20}$
	Outer P	$k_p = -2\pi(f_{cv1} + f_{cv2})C_{dc}\frac{v_{dc}^*}{1.5\hat{V}_f}$ $k_i = -4\pi^2(f_{cv1}f_{cv2})C_{dc}\frac{v_{dc}^*}{1.5\hat{V}_f}$	$f_{cv1} = \frac{f_{sw}}{200}$ $f_{cv2} = \frac{f_{sw}}{2000}$
	Outer Q	$k_p = -2\pi\frac{f_{cp}}{f_0}\frac{1}{1.5\hat{V}_f}$ $k_i = -2\pi f_{cp}\frac{1}{1.5\hat{V}_f}$	$f_{cp} = \frac{f_{sw}}{400}$

In this table, ω_0 is the angular fundamental frequency, $R_{mp} = \frac{V_{mp}}{I_{mp}}$ is the equivalent resistance at the point of maximum power, $L_t = L_g + L_f$ and $R_t = R_g + R_f$ are the LCL filter series associated inductance and resistance, $\hat{V}_f$ is the grid phase voltage amplitude and f_c are the cut-off frequencies of each controller pole.

3.2 Impacts of meteorological variables on the PV inverter components lifetime

The most important meteorological variables in PV systems are solar irradiance G and ambient temperature T_{amb}. Besides the ambient temperature, the module operating temperature T_m is another important parameter in PV systems. In certain applications, the wind speed can also be included for a more accurate module temperature estimation (Schwingshackl et al., 2013; Souza; Souza; Pereima, 2018) or for safety purposes in tracker systems (Kray; Markus, 2019). Nevertheless, this last parameter will not be considered in the present thesis.

3.2.1   Static analysis of PV module operating temperature

The exposition of the PV module surface to solar radiation increases its operating temperature, which leads to a reduction in the energy conversion efficiency (Zaini et al., 2015). Several challenging aspects are faced while predicting the module temperature, since it depends on the encapsulating material, thermal absorption and dissipation properties, types of cells and configuration of internal associations, local installation and operating points, climatic conditions of locality and so on (Alonso García; Balenzategui, 2004). Therefore, empirical models have been developed over the past decades to improve module temperatures prediction accuracy. There are many works in literature regarding comparative analysis of PV module temperature prediction models (Jakhrani et al., 2011; Olukan; Emziane, 2014). One of the simplest and most used model was proposed by Ross e Smokler (1986) and it is known as Ross' thermal model, described as:

$$T_m = T_{amb} + (T_{m,NOCT} - T_{amb,NOCT}) \frac{G}{G_{NOCT}}, \qquad (3.2)$$

where NOCT stands for Nominal Operating Cell Temperature and represent a more realistic operating condition of the PV modules. The NOCT test conditions are provided by manufacturers, and usually correspond to G_{NOCT} = 800 W/m^2, $T_{m,NOCT}$ = 45 $\pm$ 2 °C and $T_{amb,NOCT}$ = 20-25 °C.

As can be noticed, the operating temperature is always higher than the ambient temperature during sunlight periods (i.e., $G \geq 0$ W/m^2). As a consequence, the PV module generates less power when Ross' expression is considered (Denoix; Sechilariu; Locment, 2014). To illustrate that, a Kyocera KD325GX-LFB PV module under different ambient temperature and solar irradiance conditions is simulated to observe the effects of the module temperature on the output power (Kyocera, 2016). Fig. 3.3 shows the PV module output power when $T_m = T_{amb}$ and when the Ross' expression is applied. The difference is more relevant when higher values of irradiance are used. For example, the difference is about 14% at Standard Test Condition (STC). This difference can affect the reliability analysis due to the difference in the generated power.
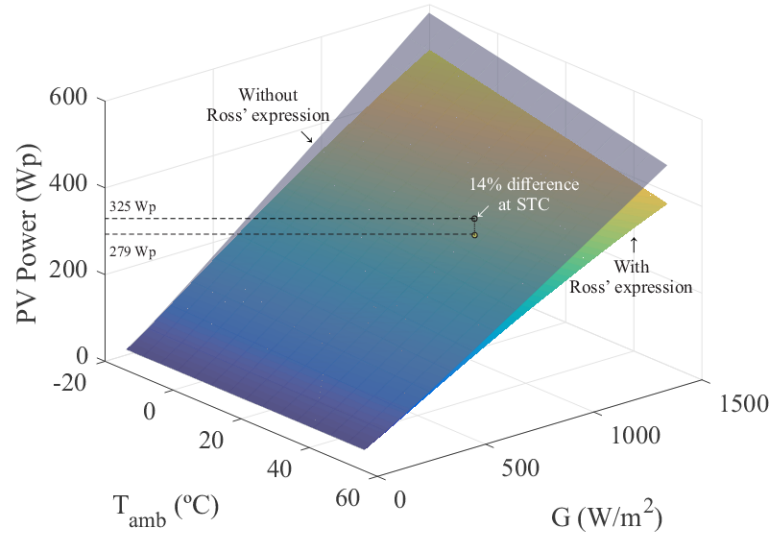
Figure 3.3: Influence of $T_m = T_{amb}$ and when it is computed by Ross' expression on the output power of a Kyocera KD325GX-LFB PV module.

.

The improvement of PV modules thermal performance is a subject of interest for manufacturers, aiming to design models with lower power temperature coefficient γ_p. This coefficient indicates how strongly the output power of a PV module is dependent on its operating temperature (Lopez-Garcia; Pavanello; Sample, 2018). Typically, γ_p is expressed in $\%/K$, with negative effect on the PV module output power. Emerging PV modules technologies, such as PERC (Passivated Emitter Rear Cell), MBB (Multi Bus Bars), tiling ribbon and cutting cells (e.g., half-cells) have, among other advantages, reduced γ_p. This improvement can be explained by the reduction of internal resistances, which reduces the power losses and, consequently, the module operating temperature. For the sake of comparison, Trina Solar TSM-415-DE15M PV module, launched on the market in 2020, has γ_p = -0.36 %/K, against Kyocera KD325GX-LFB, launched in 2016 with γ_p = -0.45%/K (Trina, 2020). At STC condition, this Trina module has around 9% of power reduction in comparison with 14% of that one of Kyocera, presented in Fig. 3.3.

3.2.2 Dynamic analysis of PV module operating temperature

In the Design for Reliability assessment, mission profiles (MP) are used as input in the reliability evaluation process. These MP are usually obtained from real field measurements of solar irradiance and ambient temperature, in the case of PV system applications. During such process, the measured data is acquired with a defined sample time. It is important to note that the lower is the MP sample time, the more accurate is the reliability evaluation. However, short sample times need powerful data acquisition systems and mass storage capability. In Silva et al. (2020), the authors discuss the role of the mission profile resolution on the reliability analysis. effects of considering mission profiles with different resolutions. Additionally, Cupertino et al. (2019) investigates the impact of the mission profile length on the lifetime prediction. Normally, the mission profiles are sampled in the range of seconds/minutes with one year of duration.

The ambient temperature and solar irradiance mission profiles are used as input of Ross' expression defined in (3.2) to estimate the PV module temperature. However, the surface of the PV module does not respond instantly to MP variations. There is a thermal dynamics which describes how the heat flows through the different material layers that compose the PV module. This thermal dynamics is normally modeled as RC thermal networks with specific time constants for each layer, depending on the thickness and the material used (Lobera; Valkealahti, 2013). There are several layers in the composition of the PV module, such as aluminum frame, tempered glass, EVA encapsulant, solar cells and bachsheet. Each layer has its own thermal dynamics. Therefore, one simple approach is to model the entire PV module with an unique RC thermal network with an equivalent thermal time constant τ_{th}, as shown in Fig. 3.4.

The literature presents several experimental works to determine the PV module thermal time constant τ_{th}. In Matsukawa e Kurokawa (2005), a Kyocera 125 Wp PV module was subjected to irradiance step changes leading to a time constant of approximately 10.5 min. In Tina e Abate (2008), some indoor measurements were carried out and the estimated time constants ranged between 5-10 minutes, depending on the PV module size and technology. In Armstrong e Hurley (2010), the authors propose a new thermal model for PV modules under varying atmospheric conditions and
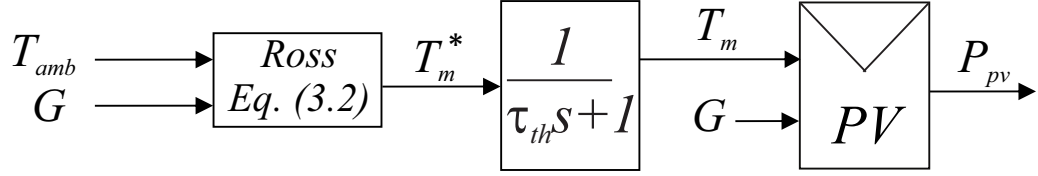
Figure 3.4: Block diagram of PV module output power determination making use of Ross's expression to calculate the PV module operating temperature.

.

found thermal time constants of 3.99-6.38 minutes, depending on the local wind speed. Recently, Osma-Pinto e Ordóñez-Plata (2020) proposed a dynamic thermal modeling of a Canadian Solar CS6P-255W PV array with an integrated cooling systems and found thermal time constants of 8.3 and 7.8 minutes, also depending on the wind speed.

The effects of considering the thermal dynamics of a 250 Wp PV module on the generated output is didactically represented in Fig. 3.5. The PV module thermal time constant τ_{th} is considered as 5 min. Five solar irradiance steps with duration of $5\tau_{th}$ are applied to simulate a daily solar irradiance profile, as shown in Fig. 3.5 (a). The ambient temperature is kept constant and equal to 25 °C while the PV module operating temperature is calculated through Ross' expression, as shown in Fig. 3.5 (b). As can be noticed, there is a PV module heating time, where the reference temperature T_m^* is higher than T_m, and there is the cooling time, where the opposite occurs. Therefore, if the thermal dynamics is considered, the PV module generates more energy in the morning and less energy in the afternoon, as can be seen in Fig. 3.5 (c). However, the energy balance is not zero, due to the temperature delay caused by the PV module thermal capacitance. Therefore, it is expected that the PV module generates more energy over the day, even if it is quite a few amount.

The PV modules thermal dynamics are usually neglected in reliability evaluation processes found in literature. Still, there are missing works to measure the impacts of this consideration in the PV inverter lifetime prediction. Therefore, during the case study in the following section, the effects of the PV module thermal dynamics will be evaluated.
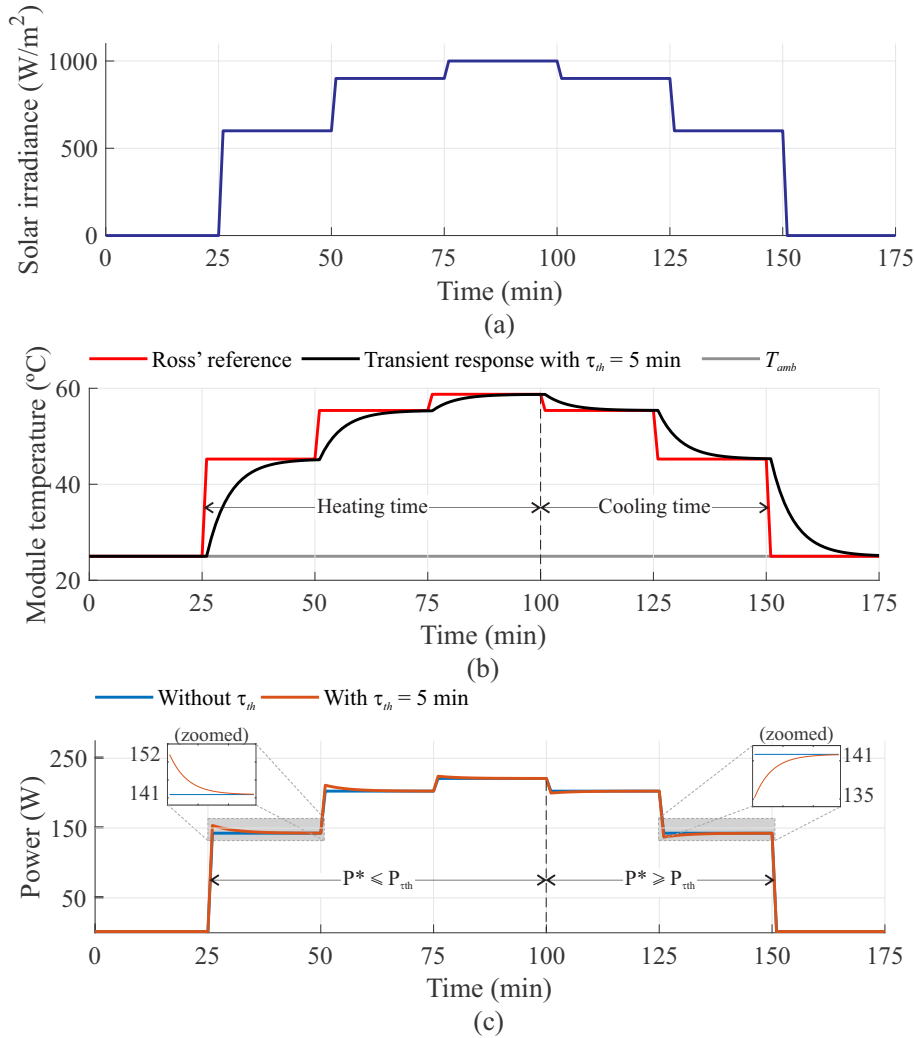
Figure 3.5: Didactic representation of the thermal dynamics effect on a 250 Wp
           PV module output power: (a) solar irradiance steps, (b) PV module
           operating temperature, and (c) PV module output power.

3.3 Case study: Mission profile variations and PV module thermal dynamics

In real applications, the same PV inverter part number can be installed
in several regions around the world, being submitted to different mission
profiles. Therefore, the PV inverters have different lifetime expectations
depending on the local climate and meteorological conditions. To evaluate

that, the following case study considers three mission profiles of solar irradiance and ambient temperature from Aalborg - Denmark, Goiânia - Brazil and Izaña - Spain, as shown in Fig. 3.6. All the three mission profiles are sampled at 1 min during one year of measurements. It is worth noticing that these three locations have very different meteorological characteristics. Aalborg is the colder region, located at the north of Europe, thus it has lower irradiance and temperature profiles. Goiânia is a city from the middle west of Brazil and due to the tropical climate, it has higher irradiance and ambient temperature. Finally, Izaña is a region on Tenerife island and it has high irradiance profile with low ambient temperature, which is ideal for PV system energy generation.
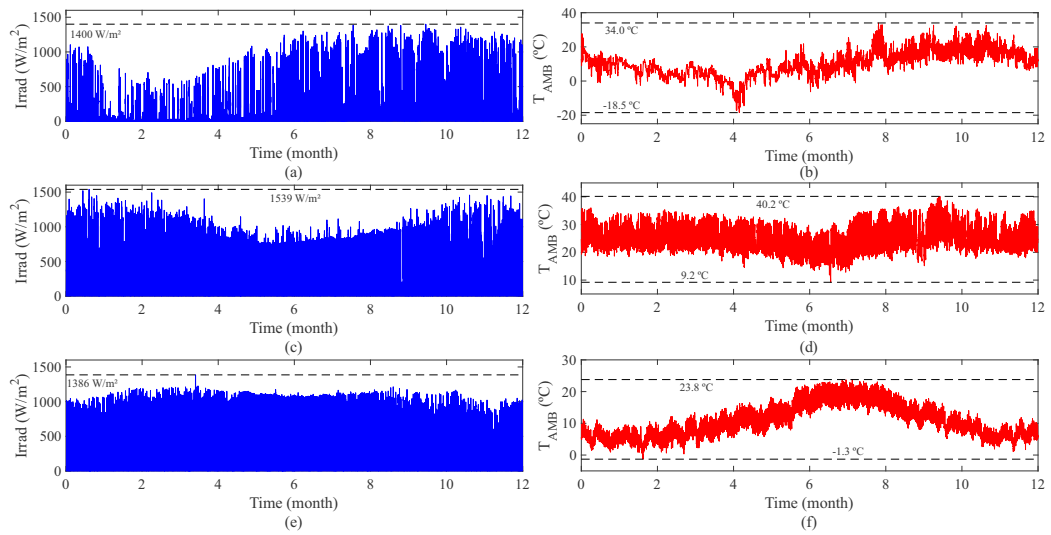
Figure 3.6: Long-term 1-year mission profiles sampled at 1 min: solar irradiance and ambient temperature from (a)-(b) Aalborg - Dinmark, (c)-(d) Goiânia - Brazil and (e)-(f) Izaña - Spain.

3.3.1   PV inverter description

Table 3.2 presents the PV inverter characteristics for this case study. Four PV arrays with 16 series 250 W_p PV modules (part number Jinko Solar JKM250P-60-A) are connected to each MPPT input (Jinko, 2015). The total watt-peak power is 12 kW_p.

Table 3.2: Parameters of the PV inverter.

Parameter	Symbol	Value
Grid voltage (line to line)	v_g	380 V
Grid fundamental frequency	f_0	60 Hz
Rated power	S_n	12 kVA
MPPT installed power	$P_{pv,MPPT}$	3 kWp
Total PV array power	$P_{pv,tot}$	12 kWp
Dc-dc stage switching frequency	f_b	20 kHz
Dc-ac stage switching frequency	f_i	20 kHz
LCL filter inductance	$L_f = L_g$	220 μH
LCL filter resistance	$R_f = R_g$	8.3 $m\Omega$
LCL filter capacitance	C_f	6.8 μF
LCL filter damping resistance	R_d	0.92 Ω
Dc-link Voltage	v_{dc}	620 V
Dc-link capacitance	C_{dc}	300 μF
Boost input capacitance	C_b	100 μF
Boost converter inductance	L_b	5 mH
Boost converter resistance	R_b	47.1 $m\Omega$
Dc-link cap. thermal resistance	$R_{th,dc}$	20.86 K/W
Boost input cap. thermal resistance	$R_{th,b}$	23.10 K/W
IGBT junction-case thermal resistance	$R_{th,j-c,i}$	0.16 K/W
Diode junction-case thermal resistance	$R_{th,j-c,d}$	0.28 K/W
Heatsink thermal resistance	$R_{th,h-a}$	0.06 K/W

The selected power devices used in this work are stated as follows: the
three-phase inverter is composed of six discrete IGBTs with freewheeling
diodes rated at 75 A / 1200 V, manufactured by Infineon, with part number
IKQ75N120CT2 (Infineon, 2019). The boost converters IGBT and diode
are given the same part number as the three-phase inverter. The heat-sink
has forced air-cooling system, with $R_{th,h-a} = 0.06 K/W$, manufactured by
Wakefield-Vette (part number 511-9M) (Wakefield-Vette, 2007). All the
power semiconductor devices are connected to the same heat-sink, sharing a
common thermal network.

Regarding the capacitors, the boost converter input capacitor C_b is
rated at 100 μF / 450 V. The dc-link capacitor bank C_{dc} is composed of
four parallels branches with two series associated 150 μF / 450 V, totalizing
an equivalent 300 μF / 900 V bank. Both components are snap-in
aluminum electrolytic capacitors manufactured by TDK, part number

B43522 (TDK, 2016). The capacitors thermal resistances are 20.86 K/W for C_{dc} and 23.10 K/W for C_b, according to the empirical model developed by (Wang; Blaabjerg, 2014).

The characteristics of the proposed PV system are used in electrical simulations to extract the active power delivered to the grid for each mission profile, shown in Fig. 3.7. The shape of the curves follows the respective solar irradiance profile, as a common characteristic of PV systems. The PV inverter dynamic saturation limits the output power to the inverter S_n. As it can be seen, the three regions generate different amounts of energy over the year. Due to moderate solar irradiance profile and low ambient temperature, Izaña is the region with highest annual generated energy, equal to 30.05 MWh. Goiânia has the highest solar irradiance profile but also the highest ambient temperature profile, generating 20.81 MWh annually. Due to its geolocalization, Aalborg is the colder region and has the lowest solar irradiance and ambient temperature profile, corresponding to 13.69 MWh of annual generated energy. Therefore, the same PV inverter would suffer different stresses if installed in these regions, and these stresses will be converted in lifetime consumption in the next analysis.

3.3.2 Proceedings of lifetime evaluation

In this first moment, a detailed analysis of the static lifetime consumption and Monte Carlo simulations are provided, following the proceedings described in Fig. 2.12. For instance, the PV inverter operates as the conventional mode, without any ancillary service. The PV module operating temperature is determined by the Ross's expression, neglecting its thermal dynamics.

The mission profiles from Fig. 3.6 are translated into thermal loadings in the PV inverter components through the thermal models described in Fig. 2.5 for IGBT and Fig. 2.10 for electrolytic capacitors. The IGBTs mean junction temperature T_{jm}, junction temperature variation ΔT_j and the capacitors hot-spot temperature T_h profiles are presented in Fig. 3.8. It is worth noticing that the junction temperature variation profiles are related to short-term thermal cycles. The long-term thermal cycles are obtained when
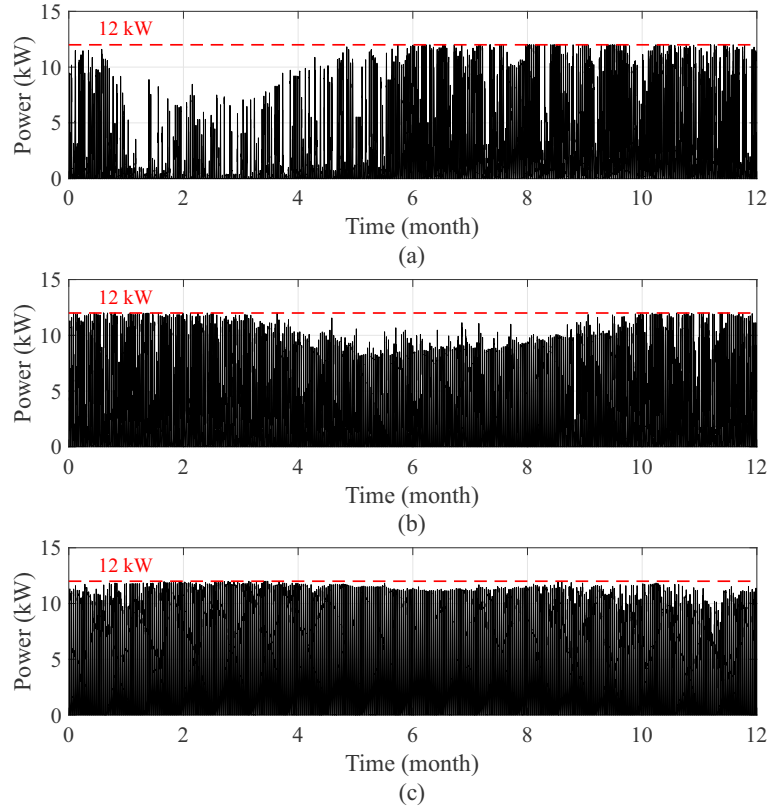
Figure 3.7: PV system output active power delivered to the grid from different regions: (a) Aalborg, generating 13.69 MWh per year, (b) Goiânia, generating 20.81 MWh per year and (c) Izaña, generating 30.05 MWh per year.

the profile T_{jm} is applied to the Rainflow's counting algorithm. Nevertheless, these profiles will not be shown in this work.

The boost converter IGBT S_b does not experience short-term thermal cycles caused by the line frequency, which are more relevant than the long-term thermal cycles in the inverter IGBT. Even so, the mean junction temperature on S_b is higher than S_{1-6} for all the three regions. This fact can be explained by the power losses through the components. In discrete components, as the current specifications rise, the conduction power losses tend to reduce and the switching power losses become more relevant. In the specific case of the investigated IGBT part number, the rated current of 75 A is at the upper limit of the technology and the power losses on this
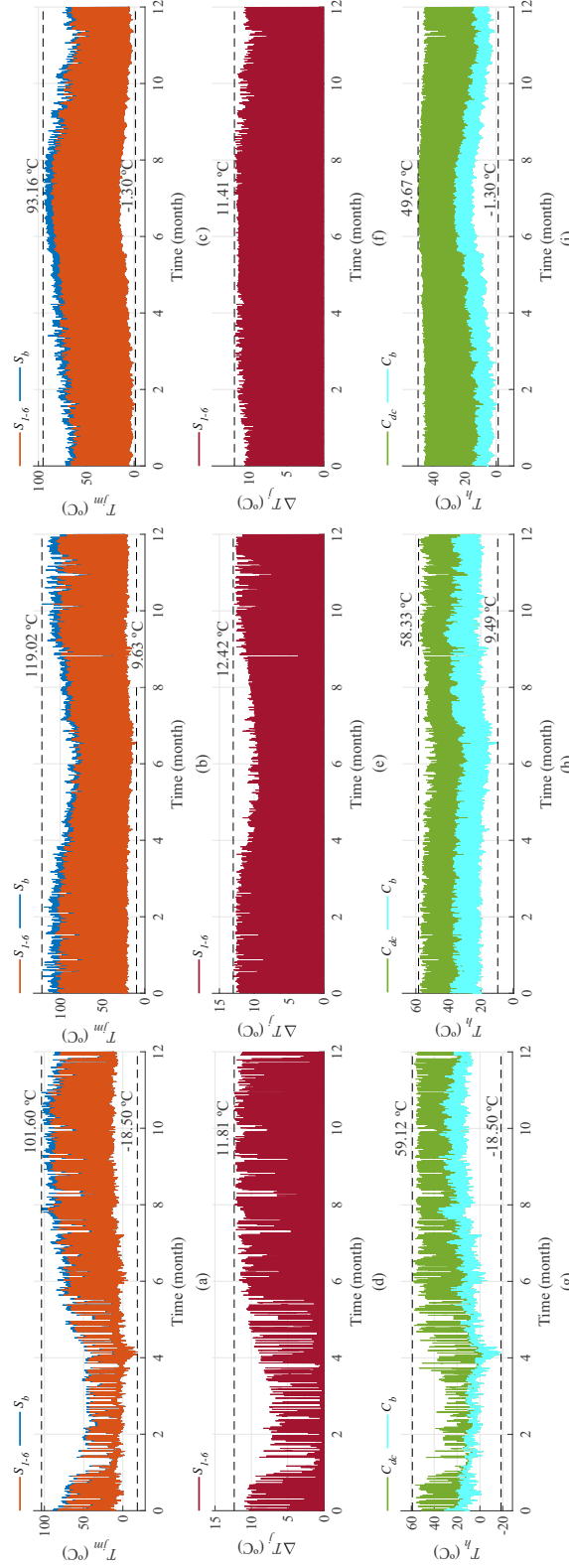
Figure 3.8: Thermal loading profiles: S_{1-6} and S_b mean junction temperature from (a) Aalborg, (b) Goiânia and (c) Izaña; S_{1-6} junction temperature variation from (d) Aalborg, (e) Goiânia and (f) Izaña; C_{dc} and C_b hot-spot temperature from (g) Aalborg, (h) Goiânia and (i) Izaña

component are mainly related to P_{sw}. When comparing the boost converter IGBT with the inverter IGBT, the former has higher number of switching events in the same 60 Hz cycle, as can be seen in Fig. 3.9.
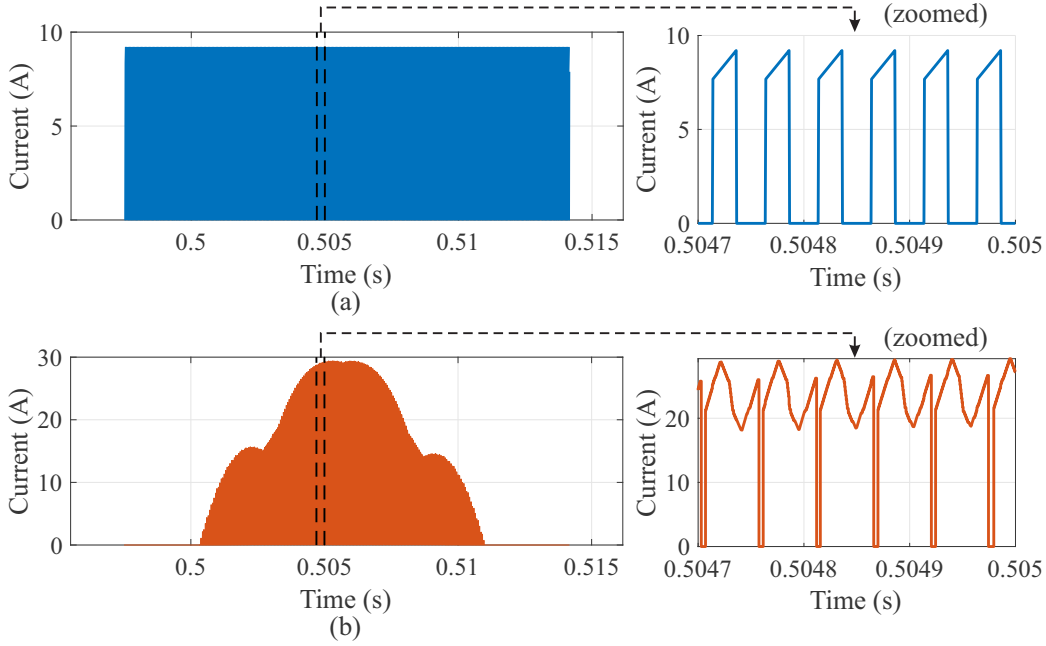
Figure 3.9: IGBT current waveform under one cycle of 60 Hz: (a) boost converter IGBT and (b) inverter IGBT. The waveforms are obtained from simulation environment with P = 12 kW and $T_j = 100$ °C.

Considering the same switching frequency f_{sw}, the boost converter IGBT has around 40% more switching events with current conduction than the inverter IGBT. In terms of power losses, the $P_{sw,IGBT}$ of S_b is around 35% higher than of S_{1-6}, even with the boost converter processing only one quarter of the inverter input power. On the other hand, the $P_{c,IGBT}$ of S_b is around 2.3 times lower than of S_{1-6}, which is expected due to the lower current stress. This value is not 4 times lower (as the number of MPPT entries) because of the higher conduction time, as illustrated in Fig. 3.9.

Other important fact evidenced in Fig. 3.8 is that the C_{dc} temperature is higher than C_b, since the dc-link capacitors are submitted to more power losses. The power losses contribution on T_h of C_b is not relevant and its temperature is mainly dominated by the ambient temperature. In addition, C_{dc} is exposed to both converter switching harmonics, while C_b absorbs only

the boost converter switching harmonic content.

In the sequence, the thermal loadings are applied to lifetime models, described in (2.13) for semiconductors and (2.21) for electrolytic capacitors. The lifetime consumption is determined using Palmgren-Miner's rule of linear cumulative damage, and it is presented in Tab. 3.3.

Table 3.3: Static lifetime consumption from PV inverter components. Values in power of 10^{-3}.

Mission profile	Static LC x 10^{-3}			
	S_b	C_b	S_{1-6}	C_{dc}
Aalborg	1.63	4.53	12.53	10.76
Goiânia	3.33	13.86	31.15	29.95
Izaña	1.21	7.11	36.99	25.11

In all the regions, the inverter IGBT S_{1-6} and dc-link capacitor C_{dc} are the most stressed components. The lifetime consumption in the semiconductors is related to the amount of energy generated from the PV system. Therefore, Izaña has the higher power semiconductor damage, followed by Goiânia and Aalborg, respectively. On the other hand, capacitor lifetime consumption has a strong dependence on the ambient temperature. This fact can explain why the damage in the capacitors from Goiânia are the highest, since this mission profile corresponds to the hottest investigated site.

As expected, the boost IGBT S_b has lower LC than S_{1-6} because of only long-term thermal cycles are accounted. LC of C_b is lower than of C_{dc} since each boost converter processes only one quarter of the dc-link input power. In addition, C_{dc} absorb both dc-dc and dc-ac stage switching harmonics, which makes its LC to be higher. These conclusions are valid for all the three regions.

The static lifetime consumption calculated in Tab. 3.3 must be converted into lifetime estimation, taking B_{10} as a figure of metric for comparison purposes. The Monte Carlo simulations are performed with 50,000 samples. The lifetime model parameters variation inserted in the simulations are performed according to a sensitive analysis as a function of the maximum variation of the IGBT v_{ce} and capacitor C, found in the

datasheet. For the investigated part numbers, v_{ce} has a maximum variation of 22.86% from typical value and ΔC is given as 20% of capacitance tolerance. Tab. 3.4 presents the maximum variation obtained for T_{jm}, ΔT_j and T_h, for the dc-dc and dc-ac stage and for each region. The technology factor A from the IGBT lifetime model and the rated lifetime hours L_0 from capacitors lifetime model are also varied by 20% of the specified value, as well. The other lifetime parameters are not varied.

Table 3.4: Maximum variation of thermal loading parameters to be applied to Monte Carlo simulations.

Mission profile	Dc-dc stage (%)			Dc-ac stage (%)		
	T_{jm}	ΔT_j	T_h	T_{jm}	ΔT_j	T_h
Aalborg	2.88	8.73	1.45	3.99	13.92	32.25
Goiânia	2.34	8.16	1.30	3.06	12.72	12.68
Izaña	4.65	7.89	2.15	6.33	14.79	19.84

The lifetime outputs from Monte Carlo simulations are arranged in histograms, separated for each component, shown in Fig. 3.10. As can be noticed, the samples of S_b and C_b lifetime are distributed in a range of time higher than of S_{1-6} and C_{dc} for all three regions. This fact indicates that S_{1-6} and C_{dc} are the most failure-prone components in the investigated case study. These histograms are fitted with a Weibull PDF and integrated over time to obtain the Weibull CDF, or the unreliability function $F_{comp}(x)$ for each component. Fig. 3.11 (a) shows the most stressed unreliability functions in component level for all three regions. These functions are associated in a series probability block diagram to find the unreliability function in system level, as shown in 3.11 (b).

The component-level unreliability functions contain all similar components arranged. In other words, S_{1-6} $F_{comp}(x)$ is composed of six IGBTs and C_{dc} $F_{comp}(x)$ contains eight capacitors. For this case study, all three regions presented the inverter IGBT as the most stressed components, which have higher probability to fail earlier than the dc-link capacitors. In terms of system-level B_{10}, Izaña is the region with lowest lifetime, 12.2 years, followed by Goiânia and Aalborg, respectively with 16.2 and 37.6 years. These results are consistent with the total processed power and
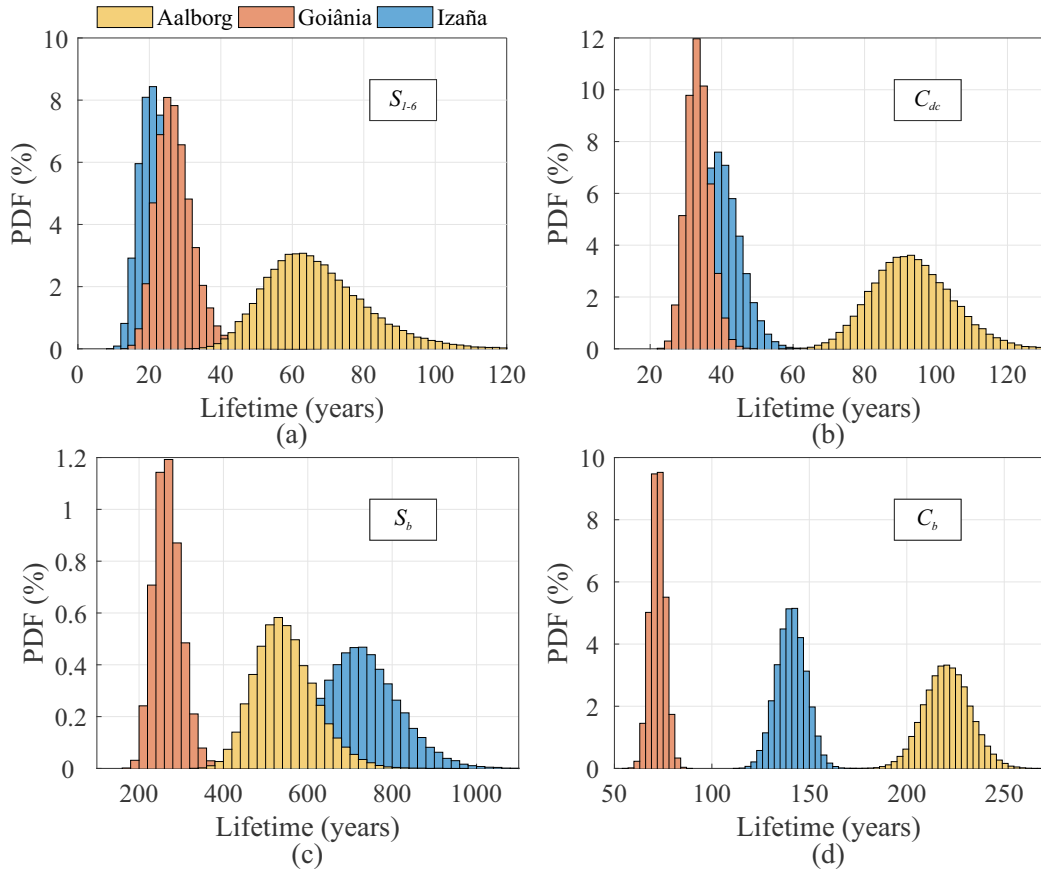
Figure 3.10: Lifetime histogram from Monte Carlo simulations with 50,000 samples: (a) inverter IGBT S_{1-6}, (b) dc-link capacitor bank C_{dc}, (c) boost converter IGBT S_b and (d) boost converter input capacitor C_b.

generated energy previously mentioned.

3.3.3 Impacts of mission profile variations on the PV inverter lifetime

The mission profiles from Fig. 3.6 are considered as the base case of the reliability evaluation process. In this analysis, some percentage variations are inserted in the base case to simulate different meteorological conditions and/or climatic randomness in the PV inverter components. Such variations
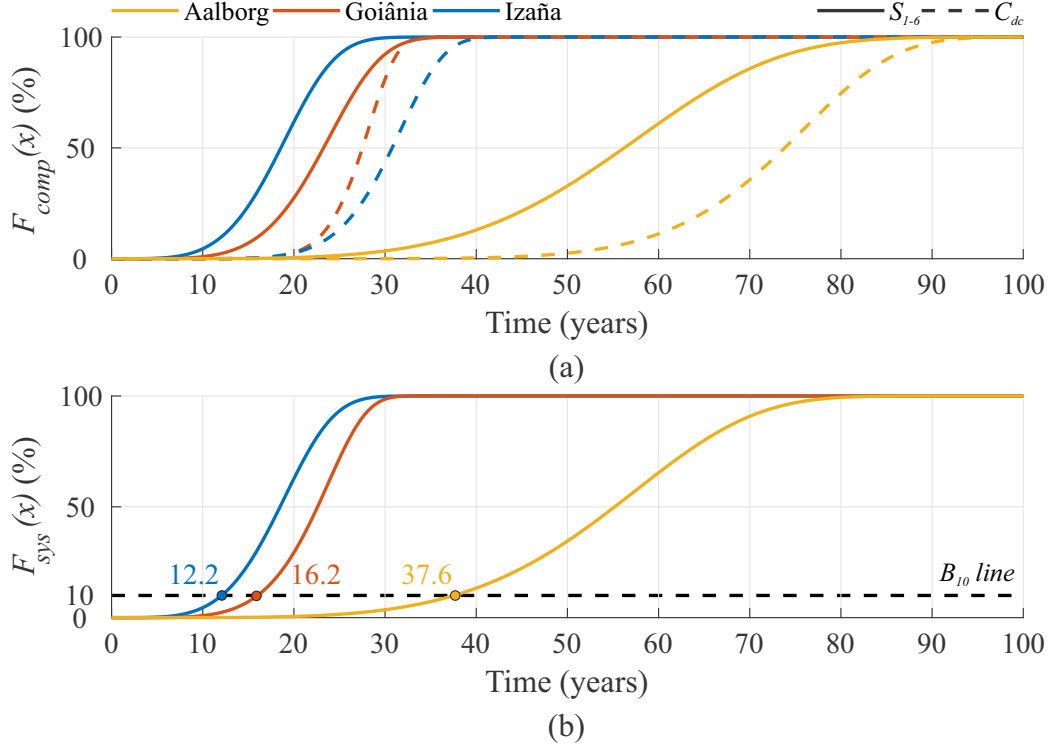
Figure 3.11: Unreliability function for all three regions: (a) component level (with only the most stressed components) and (b) system-level.

are inserted as follows:

$$G_{x\%} = G_b(1 + \Delta G\%), \tag{3.3}$$

$$T_{amb,x\%} = T_{amb,b}(1 + \Delta T\%), \tag{3.4}$$

where $G_{x\%}$ and $T_{amb,x\%}$ are the varied values of the base case G_b and $T_{amb,b}$; $\Delta G\%$ and $\Delta T\%$ are the variation factors ranging from 0-30%. Note that the performed variations are unidirectional, i.e., the varied MP is greater than base case.

Fig. 3.12 shows the lifetime consumption surfaces for the inverter IGBTs S_{1-6} and dc-link capacitors C_{dc} from Goiânia, under mission profile variations. The LC axis is presented in percentage of the base case, which is

100%, i.e., $\Delta G, T = 0\%$. As expected, the effects of increasing the solar irradiance profile increases the power output from the PV modules and accelerates both IGBT and capacitors wear out process. In addition, the IGBT are more sensitive to solar irradiance variations, with 207% of LC when $\Delta G = 30\%$ against 126% from capacitors. The increase in the ambient temperature has two opposite effects on the components, described as follows:

- The increase in the ambient temperature reduces the instantaneous active power extracted from the PV modules. Thereby, the stresses on the components are reduced as well as the lifetime consumption;

- The thermal loading is increased, since the components operate under a hotter ambient. This increase accelerates the wear out processes and increases the lifetime consumption.

The result of the combined effects of the increased ambient temperature is a reduction on the LC. In addition, the capacitors are more sensitive to ambient temperature variations than the semiconductors, with 145% of LC when $\Delta T = 30\%$ against 115% from IGBTs. Finally, the condition of $\Delta G, T = 30\%$ is the most critical in terms of lifetime consumption. Typically, it is very difficult to observe an increase in the solar irradiance profile without increasing the ambient temperature for the same geographical location. In this scenario, both IGBT and capacitor have its lifetime doubly reduced in comparison with the base case.

The component-level unreliability functions for the critical cases are illustrated in Fig. 3.13 (a)-(b) for S_{1-6} and C_{dc}, respectively. As it can be seen, the $\Delta G = 30\%$ condition in the IGBTs are more likely to fail earlier in comparison with $\Delta T = 30\%$. This situation is inverted when the capacitor unreliability curve is analyzed. However, since the IGBT curves is more displaced to the left in time, it limits the system-level unreliability function, presented in Fig. 3.13 (c). It is important to note that other PV applications may present the capacitors as the most stressed component and thus the B_{10} order under mission profiles variations can change.

For simplicity and space saving, only the LC surfaces and unreliability functions from Goiânia were showed. The same behavior discussed above is
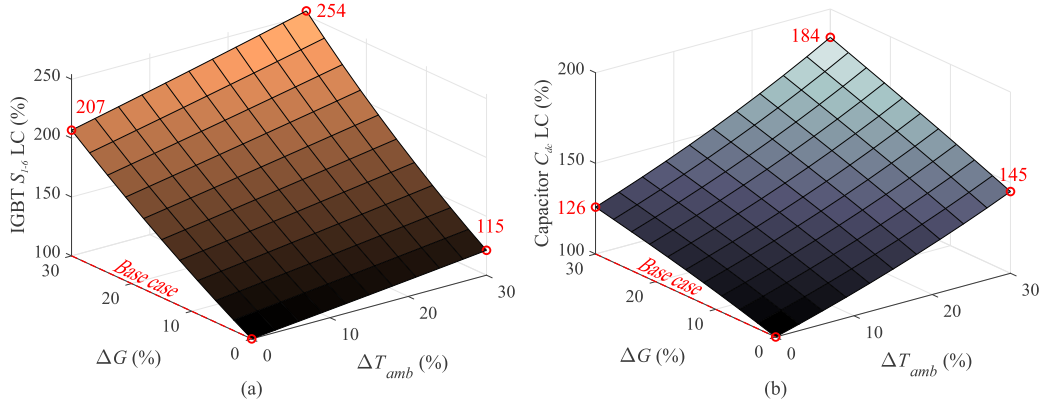
Figure 3.12: Lifetime consumption surface for Goiânia under meteorological variations on solar irradiance and ambient temperature: (a) inverter IGBT S_{1-6} and (b) dc-link capacitor C_{dc}. Base case correspond to LC = 100%.

observed for the other two regions and the B_{10} of the system-level unreliability function is presented in Tab. 3.5.

Table 3.5: Lifetime prediction in years, based on B_{10} for all three regions under mission profile variations, evidencing only the critical points.

Mission profile	Lifetime B_{10} (years)			
	Base case	$\Delta T = 30\%$	$\Delta G = 30\%$	$\Delta G, T = 30\%$
Aalborg	37.6	31.6	18.6	16.0
Goiânia	16.2	12.8	7.8	6.4
Izaña	12.2	10.8	6.4	5.6

3.3.4 Effects of static and dynamic PV module operation temperature on the PV inverter lifetime

The previous analysis did not consider the PV module thermal dynamics, i.e., $\tau_{th} = 0$ min. Therefore, the case study presented in this part describes the effects of τ_{th} on the inverter lifetime. Three cases will be evaluated:

- Case 1: the PV module operating temperature is equal to ambient temperature, neglecting the PV module thermal time constant;
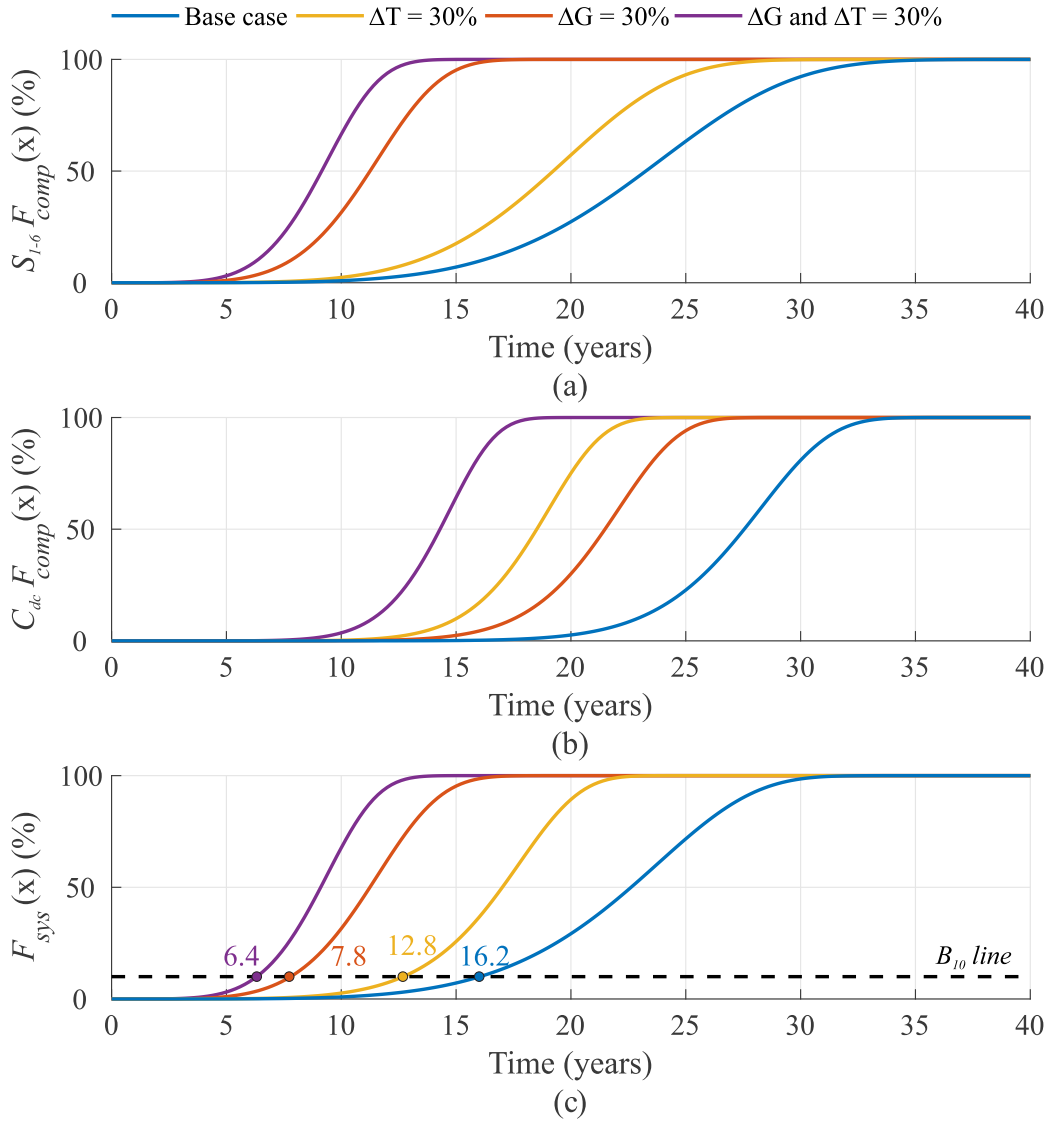
Figure 3.13: Unreliability function for Goiânia under meteorological variations on solar irradiance and ambient temperature: (a) inverter IGBT S_{1-6} component level, (b) dc-link capacitor C_{dc} component level and (c) system level.

- Case 2: the PV module operating temperature is computed by Ross' expression, neglecting the PV module thermal time constant;

- Case 3: the PV module operating temperature is computed by Ross' expression and the effect of PV module thermal time constant is

considered.

According to Fig. 3.14 (a), as the PV model thermal time constant increases from 0 to 20 min, the annual generated energy increases by less than 1% for all regions. This fact can be explained by Fig. 3.14 (b), which represents a temperature profile of a typical sunny day from Goiânia mission profile with $\tau_{th} = 15$ min. During heating times, e.g., in the morning, the PV module operating temperature did not reach steady-state reference and $T_m < T_m^*$. However, during cooling times, e.g., in the afternoon, the opposite situation occurs and $T_m > T_m^*$. Therefore, there is an energy compensation that makes Case 3 generates almost the same energy from Case 2. However, since there is a significant difference between T_{amb} and T_m, Case 1 generates around 10% more energy for all three regions.
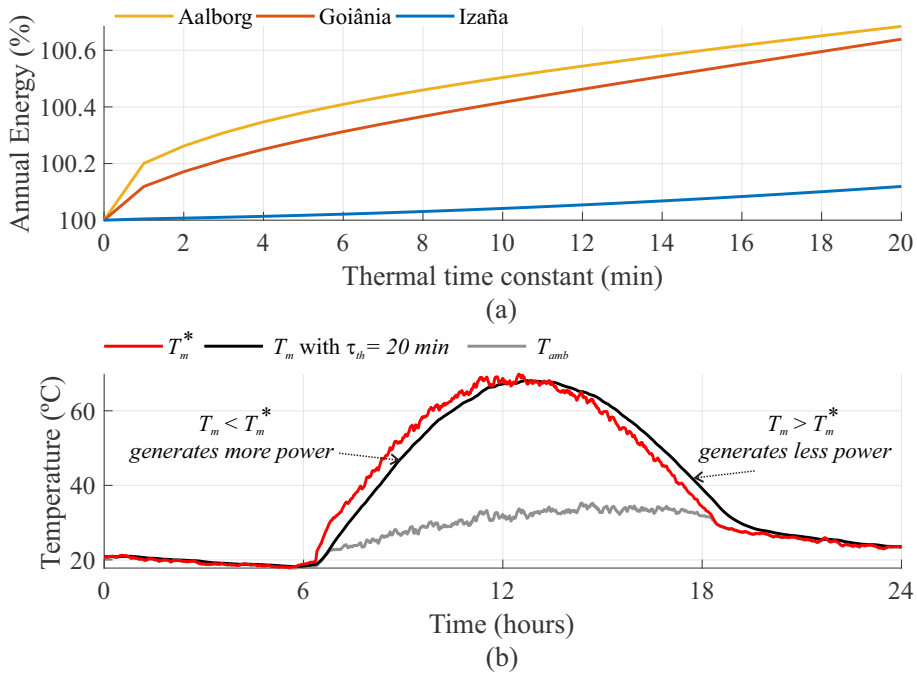
Figure 3.14: Influence of PV module thermal time constant: (a) annual generated energy and (b) temperature profile of a typical sunny day from Goiânia. Annual base values are 13.69 MWh, 20.81 MWh and 30.05 MWh from Aalborg, Goiânia and Izaña, respectively.

Fig. 3.15 shows the lifetime consumption of the inverter IGBT and dc-link capacitors for all regions, as a function of the PV module thermal time

constant. Note that, as the thermal time constant increases, the LC in both components also increases, due to more energy being generated. However, even in the edge situation, i.e., $\tau_{th} = 20$ min, the components LC increases are less than 10% for all regions, being Izaña the less affected one.
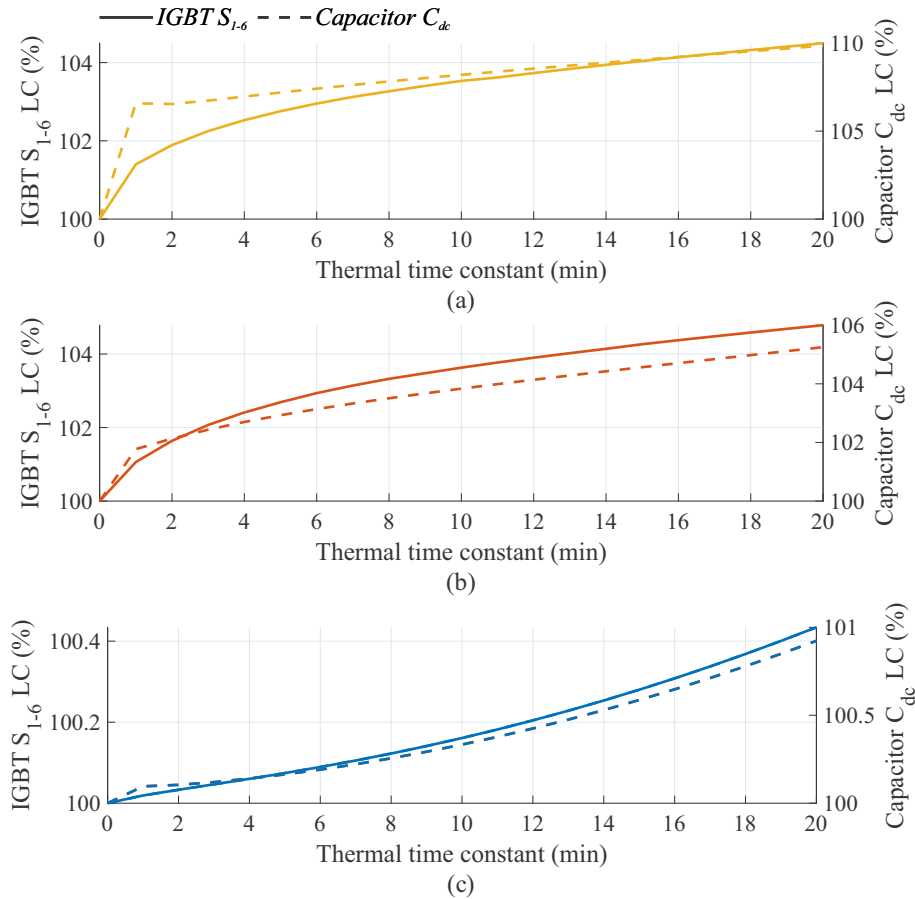
Figure 3.15: IGBT S_{1-6} and capacitor C_{dc} lifetime consumption in function of the PV module thermal time constant for the three mission profiles: (a) Aalborg, (b) Goiânia and (c) Izaña.

In terms of unreliability, Fig. 3.16 compares the three cases and the B_{10} lifetime expectations are stated in Tab. 3.6, considering $\tau_{th} = 15$ min. The most important conclusion is that the ambient temperature cannot be considered as the module operating temperature. This would lead to an underestimated PV inverter lifespan. However, the neglect of the PV module thermal dynamics is not that critical. Still, its consideration may lead the DfR and reliability assessment to be more realistic and accurate.
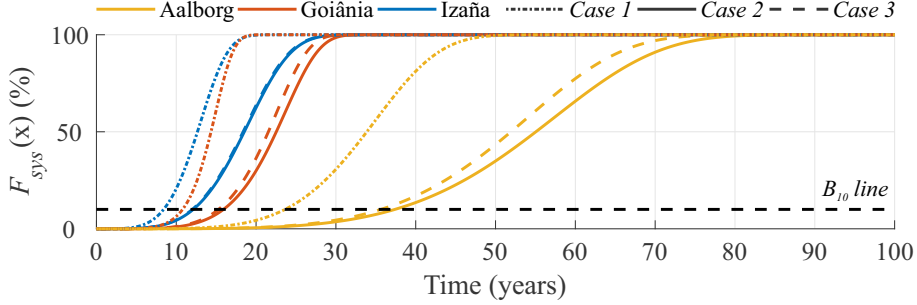
Figure 3.16: Unreliability function for all three regions during cases 1, 2 and 3.

Table 3.6: Lifetime prediction (years) based on B_{10} for the thermal dynamic analysis.

Mission profile	Lifetime B_{10} (years)		
	Case 1	Case 2	Case 3
Aalborg	23.8	37.6	35.8
Goiânia	10.8	16.2	15.6
Izaña	8.6	12.2	12.2

3.4   Chapter closure

The objective of this chapter was to present a reliability analysis of the PV inverter considering meteorological variations and PV module thermal dynamics. The results demonstrate that the mission profile variations directly affect the PV module output power, energy and reliability.

A sensitivity analysis of how the meteorological variables affect the PV inverter lifetime were performed. For such, a 30% variation in the solar irradiance and ambient temperature profile were carried out. The results showed that the inverter IGBTs are more sensitive to the solar irradiance profile, presenting a LC increase of 207% when $\Delta G = 30\%$. On the other hand, the ambient temperature profile has more impact on the dc-link capacitors lifetime consumption, showing an increase of 145% when $\Delta T = 30\%$.

When considering the PV module thermal dynamics, the annual generated energy was slightly higher than base case (less than 1% for all the

regions). Therefore, there were not significant differences in the system-level lifetime B_{10}. On the other hand, when Ross' expression was considered to evaluate the module operating temperature, the lifetime was around 50% greater for all three regions. The use of Ross's expression is of very importance. If this approach is not considered, the reliability analysis may lead to an underestimation of the PV inverter end-of-life.

Multifunctional PV inverter with capability of reactive power support

This chapter details the reactive power support as a multifunctional PV inverter ancillary service. The current standard in Brazil that describes the procedures for PV inverters interconnection with the electrical grid is compared to a well-known international IEEE standard. The relation between the converter components power losses with the processed reactive power is analyzed. Moreover, a reliability-based reactive power compensation is proposed in terms of inverter sizing ratio and reactive power derating for partial compensation. Finally, the reactive power support is applied to an industry-based power factor regulation to investigate its impact on the multifunctional PV inverter lifetime.

4.1 Reactive power compensation to improve grid power quality

Due to the intermittent characteristic and availability of the solar energy, PV systems usually operate below rated power conditions during most part of the day. As can be seen in Fig. 4.1, during a typical clear sky and sunny day, the PV system generates energy equivalent to around 30% of its full capacity (Xavier, 2018). Therefore, PV inverters has a power margin to

provide ancillary services besides the active power generation.
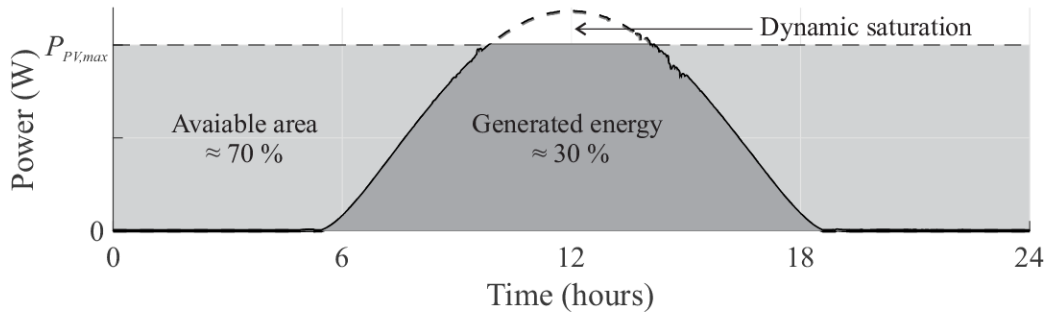
Figure 4.1: Typical active power generation of a PV system during a clear sky and sunny day. Adapted from Sangwongwanich et al. (2018b).

Fig. 4.2 presents a PV inverter with conventional operation and ancillary services, such as harmonic current compensation and reactive power support. The concept of multifunctional PV inverters is well defined in the literature. The advantages of the ancillary services provided to the grid have been thoroughly studied (Weckx; Gonzalez; Driesen, 2014; Xavier et al., 2019; Ku et al., 2020).

Initially, with low penetration of photovoltaic systems to the grid, there were not relevant impacts on the grid stability and reliability (Sarkar; Meegahapola; Datta, 2018). However, with a high increase of distributed generation to the power system, instabilities and disturbances, such as overloading or voltage rises may appear due to the intermittent characteristic of the solar energy and the unbalance between DG and load demands (Yang et al., 2013). Therefore, multifunctional PV inverters are expected to provide dynamic grid support with reactive power injection, in compliance with grid requirements and standards.

The reactive power support provided by PV inverters can be used to improve grid voltage stability by means of power losses reduction, fault ride through capability and voltage sag management (Demirok et al., 2011; Silva et al., 2016; Yang et al., 2019). Similarly, the PV inverters can provide reactive power to regulate local power factor and power management (Yu; Pan; Xiang, 2005; Gusman et al., 2020).
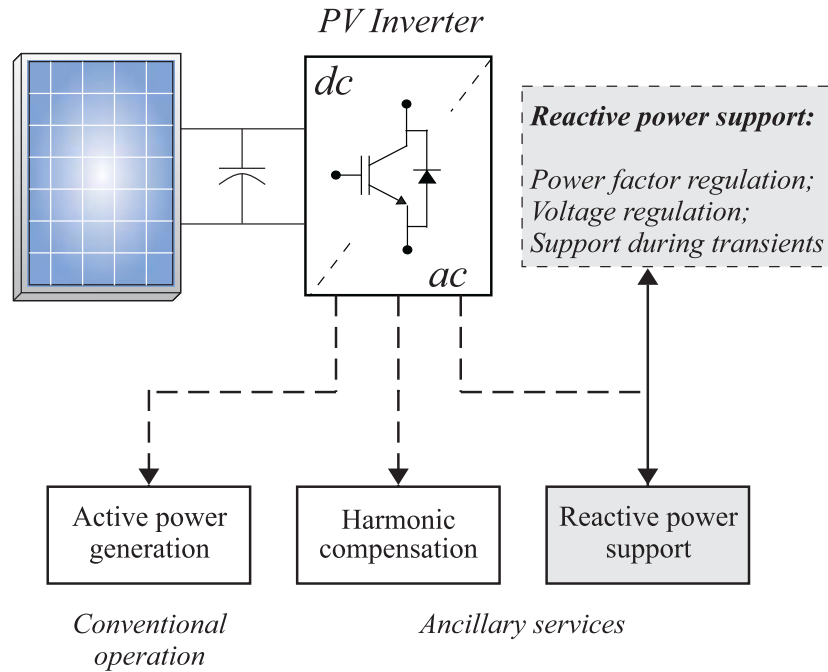
Figure 4.2: PV inverter with conventional operation and ancillary services, focused on reactive power support.

4.1.1 Current standards regarding reactive power as an ancillary service

In Brazil, the standard ABNT NBR 16149:2013 describes the characteristics of interface and connection of photovoltaic inverters with the electrical grid in distribution stage (ABNT, 2013). This standard addresses the main issues about power quality on the PCC as:

- Voltage and frequency levels compatible with the local electrical grid;

- Limitation of voltage fluctuations and flickers;

- Protection against injection of dc component to the grid;

- Voltage and current total harmonic distortion (THD) under safety limits;

- Reactive power injection/absorption and power factor operation range.

If any abnormal situation or operation out of specified limits occur, the PV inverter must disconnect from the grid and cease the energy injection.

The brazilian standard deals with power factor and injection/absorption of reactive power. According to it, if the injected active power is higher than 20% of its rated value, then the PV inverter can operate with a power factor within the range specified in Tab. 4.1. As can be noticed, this represents a very limited operation in terms of reactive power capability. Moreover, the standard does not mention any reactive power usage for voltage regulation or ride through. Despite the great efforts of the academia to show the importance of reactive power support to perform ancillary services, this standard has not been updated yet. It is important to say, that the Brazilian government has opened a public consultation to change the Brazilian standard text and include ancillary services. However, up to the date of this thesis, nothing official was published yet.

Table 4.1: PV inverter power factor operation range in function of its rated power.

Rated power (kW)	Power factor range
$S_n \leq 3$	0.98 inductive to 0.98 capacitive
$3 < S_n \leq 6$	0.95 inductive to 0.95 capacitive
$S_n > 6$	0.90 inductive to 0.90 capacitive

On the other hand, the international standard IEEE 1547 received a massive review in 2018 to include grid support functions, such as reactive power capability (IEEE, 2018). This standard describes the interconnection and interoperability of distributed energy resources with associated electric power system interfaces. The new version of the standard provides the reactive power capability and voltage/power control requirements with certain flexibility in agreement with electric power system (EPS) and distributed energy resource (DER) operators. A summary of the grid support functions related to reactive power capability provided by IEEE 1547:2018 is stated at Tab. 4.2. The Category A covers minimum performance capabilities needed for EPS voltage regulation and are reasonably attainable by all state-of-the-art DER technologies. This level of performance is deemed adequate for applications where the DER penetration in the distribution system is lower, and where the DER power

output is not subject to frequent large variations. The Category B covers all requirements within Category A and specifies supplementary capabilities needed to adequately integrate the DER in local EPS where the DER penetration is higher or where the DER power output is subject to frequent large variations.

Table 4.2: Voltage and reactive/active power control function requirements for DER normal operating performance categories according to IEEE (2018).

DER category	Category A	Category B
Constant power factor mode	Mandatory	Mandatory
Voltage-reactive power mode	Mandatory	Mandatory
Active power-reactive power mode	Not required	Mandatory
Constant reactive power mode	Mandatory	Mandatory

In terms of reactive power capability in constant power factor mode, the IEEE 1547:2018 states that the DER shall be capable of injecting/absorbing reactive power for active power output levels greater than or equal to the minimum steady-state active power capability or 5% of rated active power, whichever is greater. Tab. 4.3 presents the minimum reactive power capability when the active power output is above 20% of rated value. Note that, as the standard refers as minimum capability, the DER may have up to 100% of apparent power rating, which makes the power factor range to be 0 to 1. Moreover, the DER may operate at any power factor, e.g., for the purpose of compensating reactive power demand of local load, as long as the power factor requirements are met with EPS operator.

Table 4.3: Minimum reactive power injection and absorption capability according to IEEE (2018). The percentage values are related to the nameplate apparent power rating (kVA).

Category	Injection capability (%)	Absorption capability (%)
A	44	25
B	44	44

An illustrative comparison of the power factor operation of DER according to ABNT NBR 16149:2013 and IEEE 1547:2018 standards is

shown in Fig. 4.3 (a)-(b). However, this thesis will explore the reliability impact on a PV inverter with full reactive power capability, as shown in Fig 4.3 (c).
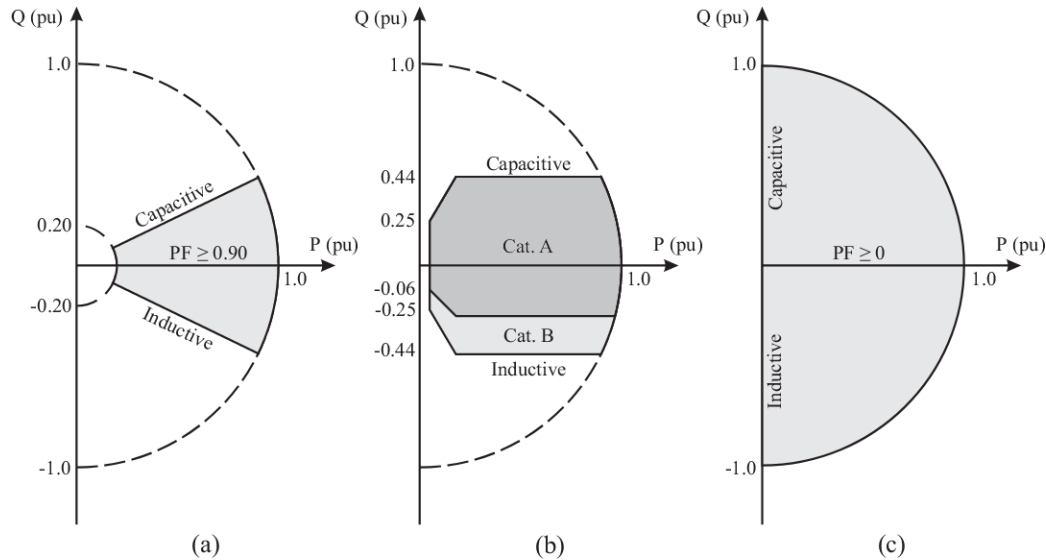
Figure 4.3: Operation limits of injection/absorption of reactive power on PV inverters operating as DER: (a) according to ABNT NBR 16149:2013, (b) IEEE 1547:2018 and (c) investigated in the case studies of this thesis.

4.2 Effects of reactive power processing on the PV inverter components power losses

The reactive power support can be employed in traditional PV inverters with improvements on the control schemes and firmware updates, taking into account safety power limits. A case study performed on a commercial PV inverter from PHB Solar company (part number PHB1500Ns) is shown in Fig. 4.4 (a) (PHBSolar, 2015). Initially, the inverter is processing 500 W as a conventional operation. Then, the inverter was set to compensate 500 var, additionally to the previous 500 W. With use of a thermographic camera, Fig. 4.4 (b)-(c) show the temperature of the inverter components. As expected, the reactive power injection increases the average internal

temperature. Moreover, the hottest points are reported as the power semiconductor terminals, indicated by the white arrows.

(a)

(b)   (c)
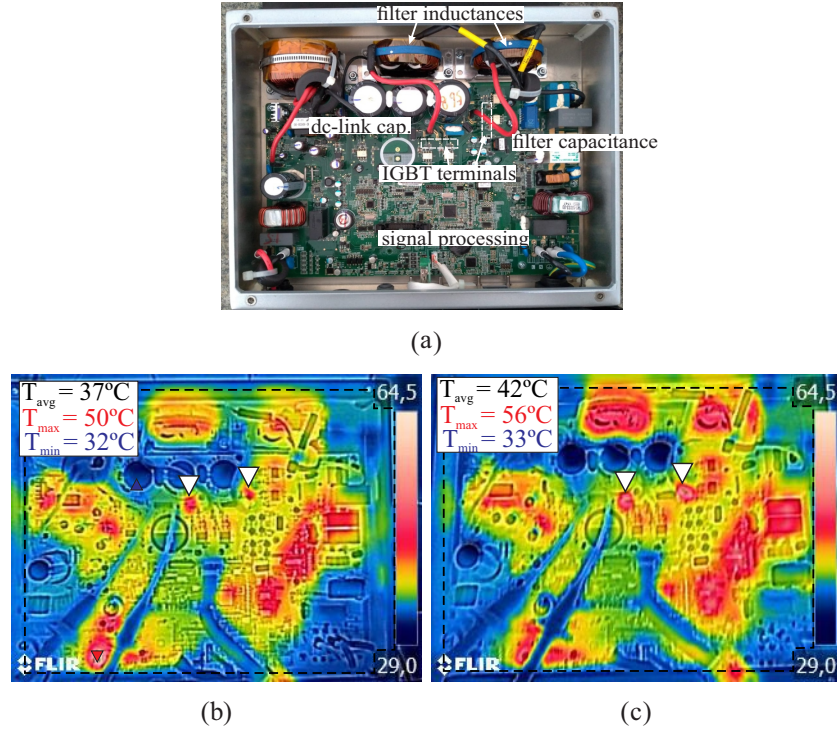
Figure 4.4: Case study of a commercial PHB1500Ns PV inverter: (a) inverter internal structure, (b) thermal loading when the inverter is processing 500 W and (c) thermal loading when the inverter is processing 500 W + 500 var.

The increase in the inverter internal temperature is caused by additional power losses due to reactive power compensation. Therefore, it is important to understand how the displacing angle θ between the inverter output voltage v_g and current i_g affects the PV inverter components power losses. As detailed in Chapter 2, the conduction losses on power semiconductors (IGBT and diodes) are related to the collector current i_c and forward current i_f, respectively. Callegari (2018) demonstrated that the power semiconductors switching power losses are not dependent on θ. The IGBT and diode currents can be divided in a RMS $i_{c,rms}$ and average $i_{c,avg}$ component. Similarly, the power losses on the electrolytic capacitors are related to the RMS value $i_{cap,rms}$. Therefore, the modeling of IGBT, diodes and capacitors current can give an understanding of how the

displacing angle θ may affect the components power losses. The summary of the currents modeling is presented in Tab. 4.4 for the boost converter and inverter components (Kolar; Wolbank; Schrodl, 1999; Grgić et al., 2020; Callegari, 2021). For this modeling, some considerations are made: inverter in steady-state operation with perfect sinusoidal waveform; the SVPWM is approximated by SPWM with zero-sequence injection; the switching harmonics in the output inverter current and voltage are neglected; the boost converters input capacitors are not interleaved; and the boost converters inductors operate in continuous mode.

Table 4.4: Boost converter and inverter components RMS and average current modeling.

Boost converter components current (A)		
Component	Average	RMS
C_b	0	$\frac{\Delta i_L \sqrt{3}}{6}$
S_b	$d i_{pv}$	$\sqrt{d\left(i_{pv}^2 + \frac{\Delta i_L}{12}\right)}$
D_b	$(d-1)i_{pv}$	$\sqrt{(1-d)\left(i_{pv}^2 + \frac{\Delta i_L}{12}\right)}$
Inverter components current (A)		
Component	Average	RMS
C_{dc}	0	$N_b\sqrt{(1-d)\left(i_{pv}^2 + \frac{\Delta i_L}{12}\right) + \hat{I}_s\sqrt{\frac{\sqrt{3}M}{\pi}\left(\frac{1}{4} + \cos^2\theta\right)}}$
S_{1-6}	$\hat{I}_s\left(\frac{1}{2\pi} + \frac{M}{8}\cos\theta\right)$	$\hat{I}_s\sqrt{\frac{1}{8} + \frac{M}{3\pi}\cos\theta - \frac{M}{90\pi}\cos 3\theta}$
D_{1-6}	$\hat{I}_s\left(\frac{1}{2\pi} - \frac{M}{8}\cos\theta\right)$	$\hat{I}_s\sqrt{\frac{1}{8} - \frac{M}{3\pi}\cos\theta + \frac{M}{90\pi}\cos 3\theta}$

Where d is the boost converter duty cycle, v_{pv} and i_{pv} are the PV array output voltage and current, respectively, $\Delta i_L = \frac{v_{pv}d}{f_b L_b}$ is the ripple current in the inductor L_b, f_b is the boost converter switching frequency, N_b is the number of parallel boost converters, $\hat{I}_s$ is the amplitude of the inverter output phase current and $M = 2\hat{I}_s/v_{dc}$ is the inverter modulation index.

The boost converter components do not experience variations in their power losses when the PV inverter processes reactive power. Thus, the components RMS and average current have no dependence with θ. On the other hand, the inverter IGBTs and the dc-link capacitor power losses are dependent on θ. Fig. 4.5 (a) and (b) show the relation of the components

current with the displacing angle, respectively.
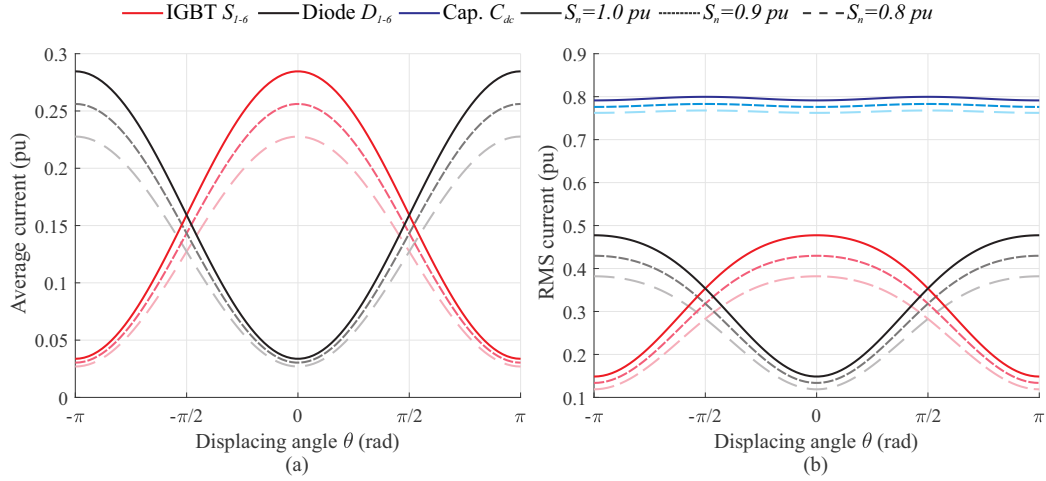
Figure 4.5: Inverter side components current in function of the displacing angle θ:
(a) average current and (b) RMS current. The current base value is
$I_{base} = \hat{I}_f$ when S = 1 pu.

If a constant apparent power is fixed, the IGBT current (average and RMS) decreases with θ. The opposite occurs with the diode, since this component conducts more current with the increase in the reactive power. The dc-link capacitor showed less sensitivity with the displacing angle in comparison with the IGBT and diode. However, the main goal of providing ancillary services is to inject reactive power apart of the existing active power, if there is a margin to do so. In this sense, it is expected that the overall PV inverter apparent power to be increased in multifunctional operation. Thereby, the conduction power losses of these components would be higher, mainly because of the increased $\hat{I}_s$ processed by the inverter. As a conclusion, the components power losses are going to be higher, leading to an increased thermal loading, which accelerates the wear out process. At the end of the day, the reactive power injection affects the PV inverter components reliability, which is the main objective of investigation of this thesis.

4.3 Reliability-oriented reactive power compensation

The DfR approach can make use of the reactive power support capability to address the most suitable components for a more reliable operation of the PV inverter. In this sense, the reactive power demanded by the electrical grid or local load connected to the PCC can be used as reference Q^* for the PV inverter control strategy. However, several works in the literature already showed that the reactive power compensation severally degrades the PV inverter lifetime (Anurag; Yang; Blaabjerg, 2015; Callegari et al., 2019; Zhou; Wang; Blaabjerg, 2020; Gusman et al., 2020). To overcome this reliability issue, the PV inverter can provide a partial reactive power compensation. As a consequence, there is a trade-off related to the amount of not compensated reactive power and the system lifetime. The severity of the trade-off depends on the application of the reactive power. For example, in power factor regulation, there is a trade-off related to the inverter reliability and the charged fees proportional to the exceeded reactive power. In this case, an economic analysis in accordance with the DfR approach can address the most profitable operation in terms of costs, reactive power and lifetime expectation.

4.3.1 Reactive power margin as a function of the inverter sizing ratio

In the converter design stage of the DfR approach, several methodologies can be applied to fulfill reliability requirements. These methodologies are normally divided in stress analysis of a given mission profile and strength modeling of the components in different stress levels (Ma; Wang; Blaabjerg, 2016). A parameter that affects the stress in the PV inverter components is the inverter sizing ratio (ISR), defined as (Mondol; Yohanis; Norton, 2006):

$$ISR = \frac{P_{pv}}{S_n}100\%. \tag{4.1}$$

Typical values of ISR range from 0.6 to 1.5 (Hussin et al., 2017).

Generally, in locals with low irradiance profiles, ISR higher than unity are applied to increase the produced energy. On the other hand, ISR values lower than unity represent an under-sizing inverter condition that can be applied to high irradiance profiles, avoiding energy losses. The optimal system sizing depends on the local climate, inverter performance, PV surface orientation and directly affects the PV energy cost (Ma; Wang; Blaabjerg, 2016). There are several works in the literature regarding the inverter sizing ratio optimization (Wang et al., 2018; Pérez-Higueras et al., 2018; Väisänen et al., 2019).

Usually, the same PV inverter part number can be employed at different sites, being submitted to different mission profiles. Thereby, manufactures provide the maximum dc power allowed to be connected to the inverter, representing the maximum ISR condition for that part number. Tab. 4.5 presents several three-phase PV inverter models in the range of 12 to 20 kVA rated power, manufactured by the most relevant PV brands currently operating in brazilian market. As can be seen, the maximum ISR condition can reach 200%. However, a common technical practice is to limit ISR to around 150% and avoid energy losses. The minimum ISR condition is usually not provided in the datasheets, but it is defined by the minimum voltage to start up the MPPT algorithm.

Table 4.5: Typical inverter sizing ratio found in commercial PV inverters' datasheet.

Manufacturer	Model	Maximum dc power (kW)	Rated ac power (kVA)	Maximum ISR (%)
ABB	PVI-12.5-TL	16,000	12,500	128
Canadian Solar	CSI-15KTL-GI-LFL	22,500	15,000	150
Fronius	Symo 12.5-3-M	12,500	12,500	100
Godwee	GW12KLV-DT	15,600	12,000	130
Huawei	SUN2000-12KTL	24,000	12,000	200
PHB Solar	PHB14K-DT	19,500	14,000	163
REFUsol	20K-2T-850P020	Not informed	20,000	100
Renovigi	Reno 15K	18,000	15,000	120
SMA	15000TL	27,000	15,000	180
Sungrow	SG12KTL-M	14,400	12,000	120
Weg	SIW500H-ST012	Not informed	12,000	100

Since the inverter components can operate under a range of ISR, they would suffer different stress levels. In terms of reliability, reference Sangwongwanich et al. (2018b) discusses the effects of PV array sizing on the inverter lifetime, analyzing the wear out effects on the power semiconductors. However, relevant works matching ISR with reactive power capability are still missing in the literature.

To improve the PV inverter yield, more modules can be connected to the system, increasing the ISR (Notton; Lazarov; Stoyanov, 2010). Under such conditions, the active power processed by the inverter is increased, as shown in Fig. 4.6 (a). As a consequence, there is an increase in the PV inverter components thermal loading, which may lead to earlier failures. On the other hand, with the increase in ISR, the available power margin to compensate reactive power is reduced, as shown in Fig. 4.6 (b).
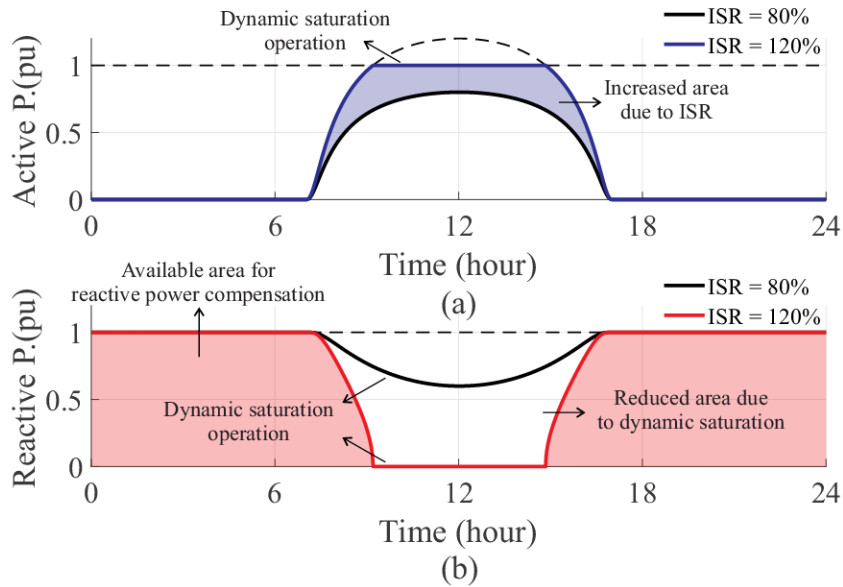
Figure 4.6: Typical PV inverter operation during a sunny day for different ISR conditions: (a) active power and (b) reactive power.

Therefore, the inverter sizing ratio has direct impact on the PV inverter reliability, since it affects both injected active power and the margin to compensate reactive power. The combined effect of ISR variation on the inverter lifetime will be further investigated in the next chapter. It is worthy mentioning that any ISR variation is made changing the number of

connected PV modules, i.e., the PV inverter design and specification is kept the same.

4.3.2 Partial reactive power compensation to improve inverter reliability

A survey carried out by reference Falck et al. (2018) determines that the lifetime target for PV applications, in an industry perspective, spans from 10-20 years. Moreover, previous studies already showed the reactive power compensation shorten the inverter lifetime. As a consequence, a full load reactive power compensation may lead the system to fail prematurely and make this ancillary service economically unfeasible. Therefore, if a desired lifetime is targeted, there is a maximum reactive power specification which the PV inverter can compensate without compromising its lifetime. In addition, this maximum reactive power value is also function of ISR, since it affects the margin of the PV inverter to compensate reactive power, as shown in Fig. 4.7.
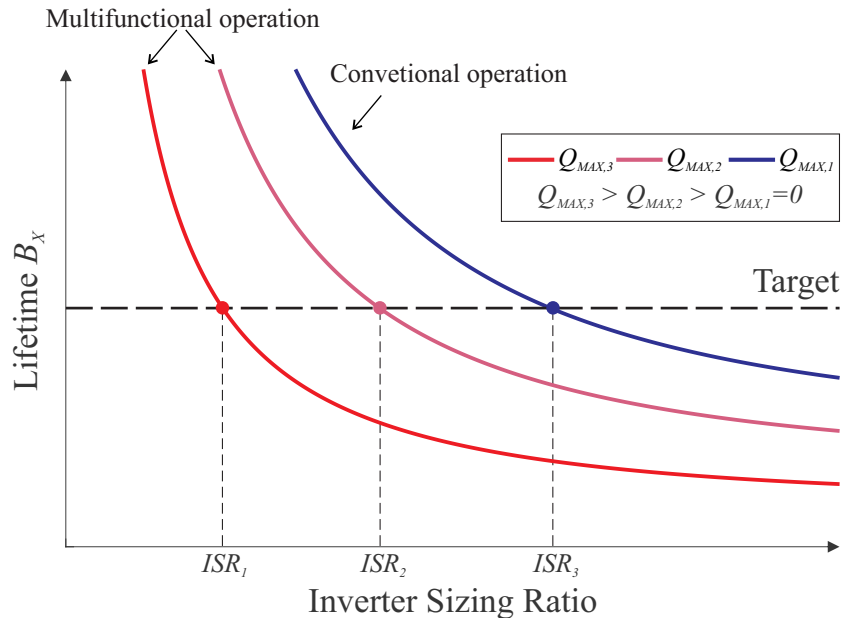
Figure 4.7: Typical PV inverter lifetime B_x curves for different reactive power conditions in function of ISR.

Despite being a more profitable use of the system during idle conditions, the reactive power increases the power losses and accelerates the PV inverter wear out process. To improve the lifetime, the reactive power reference Q^* can be limited by a derating factor Q_R and (3.1) can be rewritten as follows:

$$Q* \leq \frac{Q_R}{100} \sqrt{S_n^2 - P^{*2}}, \tag{4.2}$$

where Q_R ranges from 0 % to 100 %. When a typical reactive power profile is taken, Q_R is applied to the maximum reactive power value, as shown in Fig. 4.8. If $Q_R = 100$ %, the PV inverter can compensate the entire reactive power profile. On the other hand, if $Q_R = 0$ %, the multifunctional operation of the PV inverter is reduced to the conventional case, without reactive power capability. Therefore, ISR and Q_R can be used as degrees of freedom in the reliability analysis to achieve the desired lifetime. Note that, even with high values of Q_R, the total reactive power compensated by the PV inverter is conditioned to the dynamic saturation condition.
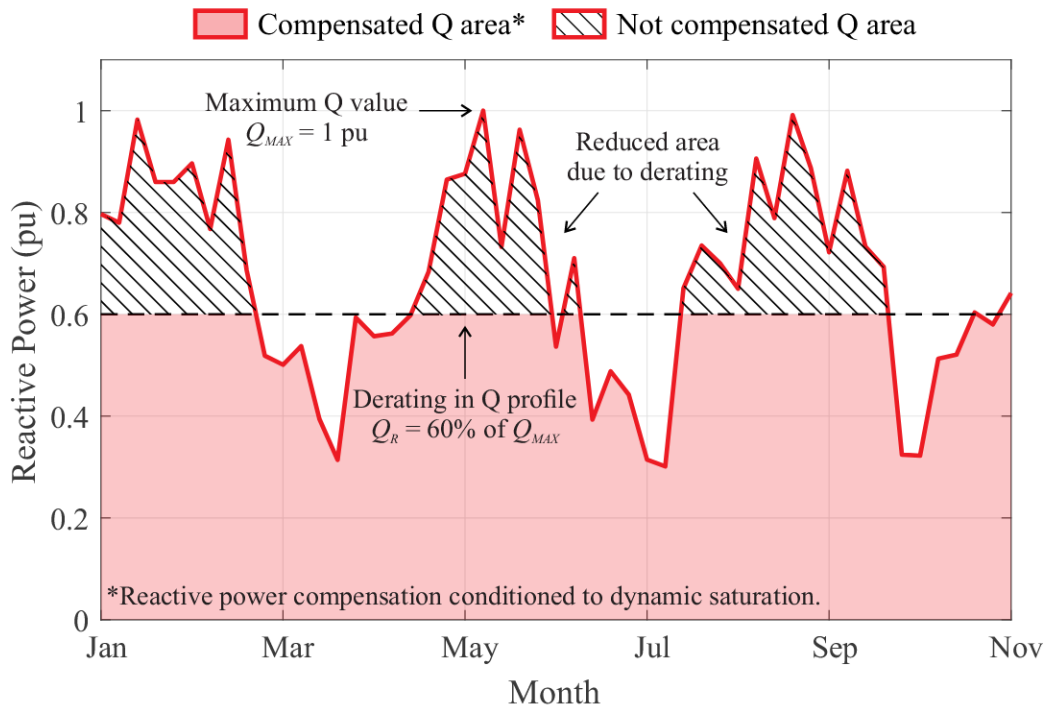
Figure 4.8: Typical reactive power profile derated by Q_R.

The idea of applying Q_R to the reactive power reference is to partially compensate the reactive power profile demanded by the electrical grid or local load. By doing so, the reliability requirements can be achieved giving up an amount of reactive power not compensated. The trade-off related to partial reactive power compensation will be investigated in the next chapter as a case study, exploring a range of ISR conditions.

4.4 Reactive power support applied to power factor regulation

The industry facilities are expected to absorb power from the electrical grid in the range of tens to thousand kVA, as shown in Fig. 4.9 (a). In this scenario, photovoltaic-based distributed generation are of most interest to provide active power and reduce the energy bills (Gusman et al., 2020). However, when conventional PV inverters are applied to supply a local load with active power, as shown in Fig. 4.9 (b), the grid is responsible for providing reactive power with very low power factor. As a consequence, industry owners can be taxed by the power company to operate below minimum power factor requirements. According to ANEEL (2010),

One possible solution to avoid extra fees due to low PF operation is a multifunctional PV inverter with reactive power support, as shown in Fig. 4.9 (c). In this case, the PV inverter supplies both load active and reactive power. The reactive power support as an ancillary service can increase the PV system attractiveness at the cost of reliability shortcomings (Gandhi et al., 2019).

Four different active power load profiles, shown in Fig. 4.10, are used to investigate the impacts on the power factor after a PV system is connected to the electrical grid. These profiles are extracted from a typology campaign for load characterization realized by CEMIG (2012). The profiles are defined as:

- Load profile A: Low energy consumption during the entire day, with peaks around 6 AM, 12 AM and 6 PM;
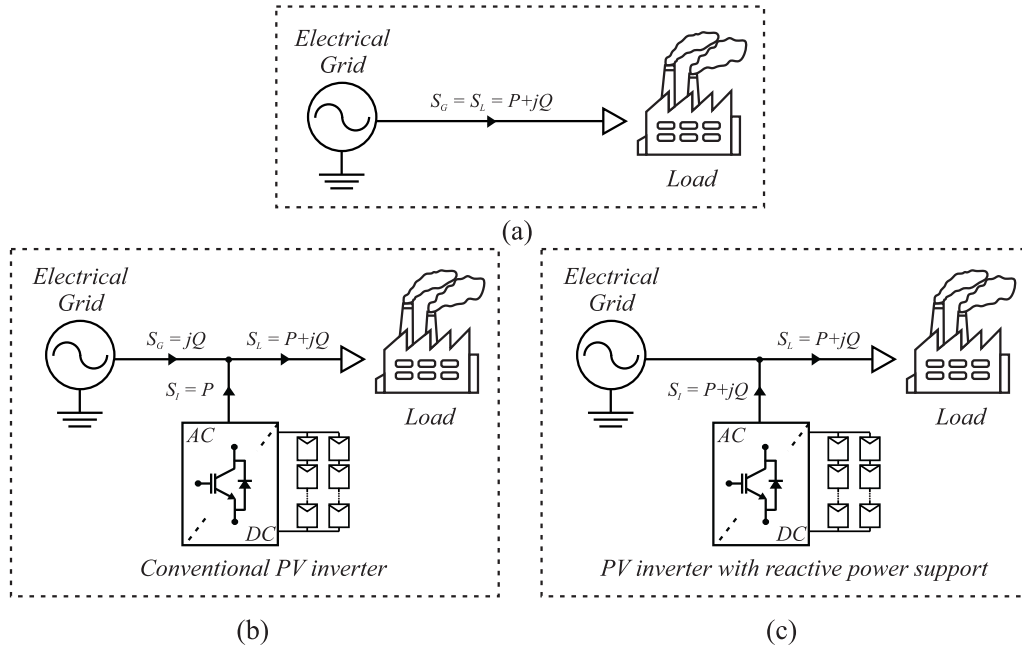
Figure 4.9: Power flow in PV inveter connected to the grid and local load: (a) the grid feeds the load with apparent power; (b) the conventional PV inverter feeds the load with active power and the grid provides reactive power only; (c) the multifunctional PV inverter provides both active and reactive power to the load

.

- Load profile B: Almost constant energy consumption during the day, starting around 6 AM to 9 PM, with low remaining activity at night;

- Load profile C: Daily activity, with energy consumption starting around 6 AM to 6 PM and a small reduction around 1 PM. Almost no energy consumption at night;

- Load profile D: Night activity, with more consumption from 6 PM to 6 AM and low remaining daily activity.

For instance, it is considered that each load profile has power factor regulated to the reference required by the electric utility before the PV system installation. In the case of Brazil, the minimum power factor required is 0.92, which is taken as reference in this thesis (ANEEL, 2010). The reactive power profiles for each load condition that makes the power factor equal to

the reference are shown in Fig. 4.10. A theoretical PV system is designed to generate the exact amount of consumed energy. The rated peak difference Δp_k from the PV system to the load profile during the time interval of active power generation is equal to 1.26, 2.53, 1.52 and 4.38 for load profiles A, B, C and D, respectively.
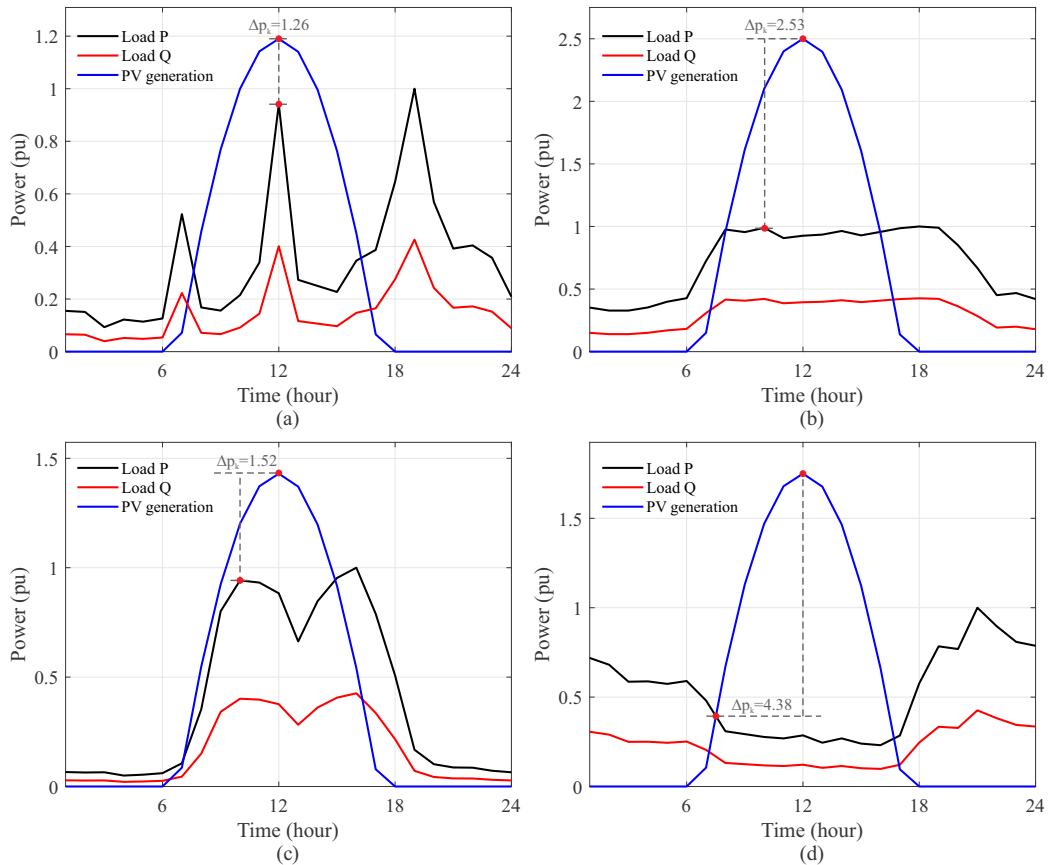
Figure 4.10: PV generation and load active/reactive power profile: (a) load profile A, (b) load profile B, (c) load profile C and (d) load profile D. The PV system is designed to match consumption to generation.

Fig. 4.11 shows the load power factor after the connection of the PV system in conventional mode and with reactive power support to regulate power factor. Additionally, Fig. 4.12 shows the reactive power compensated by the multifunctional PV inverter and the reactive power not compensated due to dynamic saturation. The main issue with low power factor operating occur when the PV system instantaneous active power generation is close to the load instantaneous active power demand, like in load profile A and C.

In this case, the electrical grid provides reactive power to the load with low power factor. On the other hand, if Δp_k is high, like in load profile B and D, the PV system provides active power to the load and injects the exceeding to the grid, increasing the PF. Note that, the greater Δp_k is, the higher is the power margin that the inverter has to compensate reactive power and regulate the power factor. Therefore, in Fig. 4.11 (b) and (d), the PV inverter has margin to keep the PF above reference during all day. However, there are some points in Fig. 4.11 (a) and (c) where the PV inverter cannot regulate the power factor.
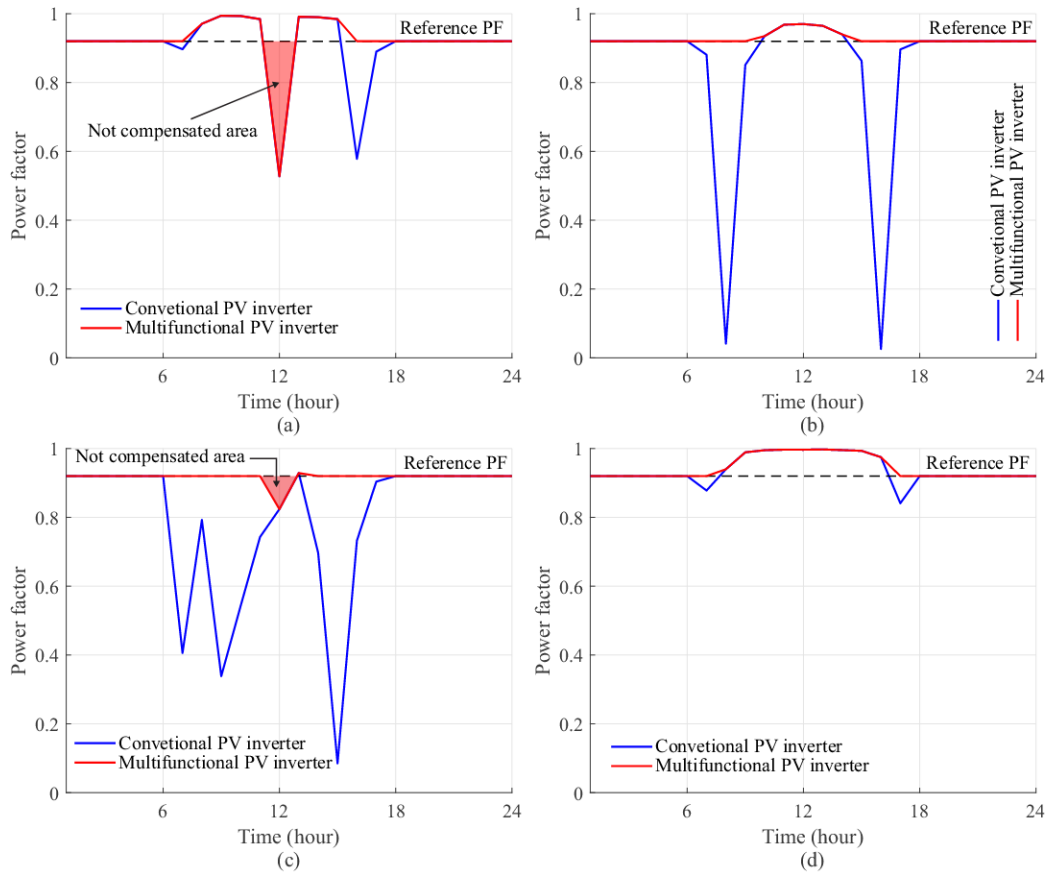
Figure 4.11: Impact of PV system connection to the grid on the power factor as conventional and multifunctional operation: (a) load profile A, (b) load profile B, (c) load profile C and (d), load profile D. Reference power factor is 0.92.

Tab. 4.6 presents the integral of compensated and not compensated reactive power over time for each load profile, in pu per hour. It can be
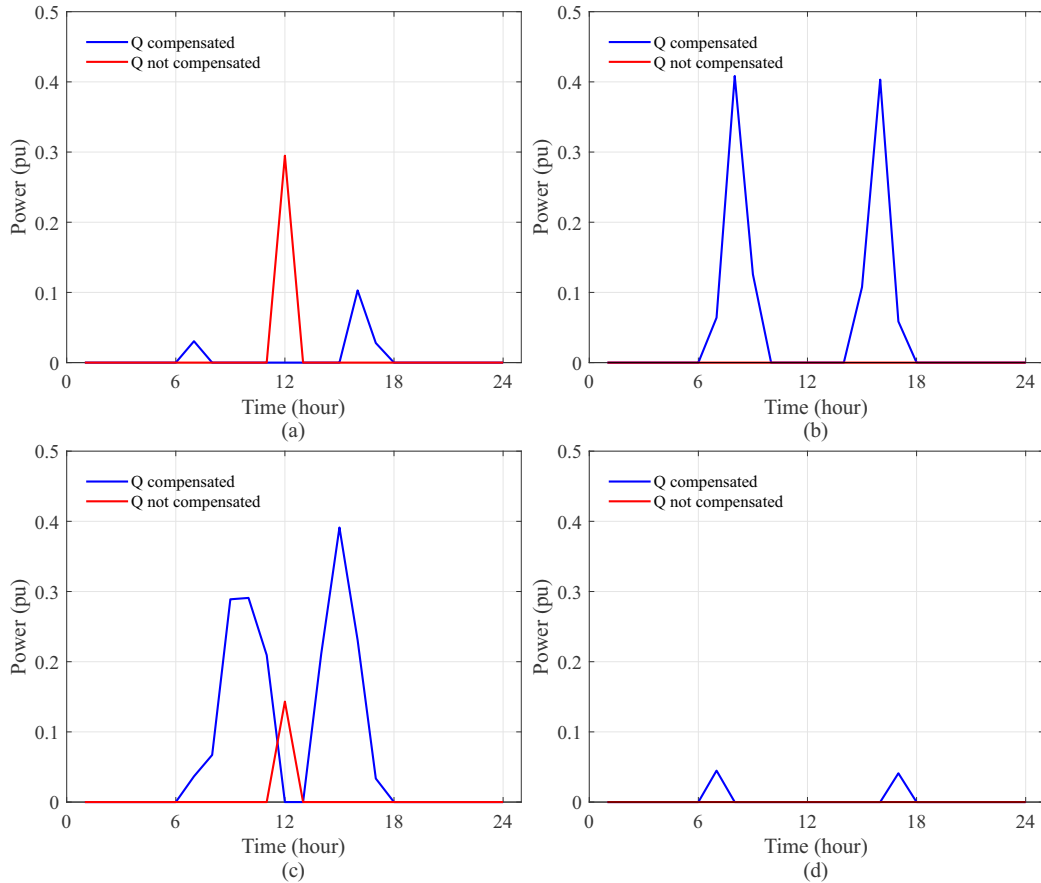
Figure 4.12: Reactive power profile compensated by the multifunctional PV inverter and not compensated due to dynamic saturation: (a) load profile A, (b) load profile B, (c) load profile C and (d), load profile D.

seen that load profile C is the case where the PV inverter compensates more reactive power.

Since the inverter sizing ratio also affects the reactive power margin of multifunctional PV inverters, it also affects the power factor, as shown in Fig. 4.13 for load profile C. In this case, the rated specification of the PV inverter is the same and three cases of ISR are presented. Additionally, Fig. 4.14 shows the reactive power profiles compensated by the multifunctional PV inverter and not compensated due to dynamic saturation. When ISR = 80%, the PV inverter has margin to regulate all points of the PF. On the other hand, with ISR = 120%, there are more points in which the PV inverter cannot regulate the PF, in comparison with ISR = 100%.

Table 4.6: Integral of compensated and not compensated reactive power when the PV inverter operates as multifunctional mode. The non-compensation instances occur when there is no available power margin due to dynamic saturation.

Category	Integral of comp. Q^* (pu.h)	Integral of not comp. Q^* (pu.h)
Load profile A	0.1612	0.2948
Load profile B	1.1675	0
Load profile C	1.7598	0.1431
Load profile D	0.0858	0
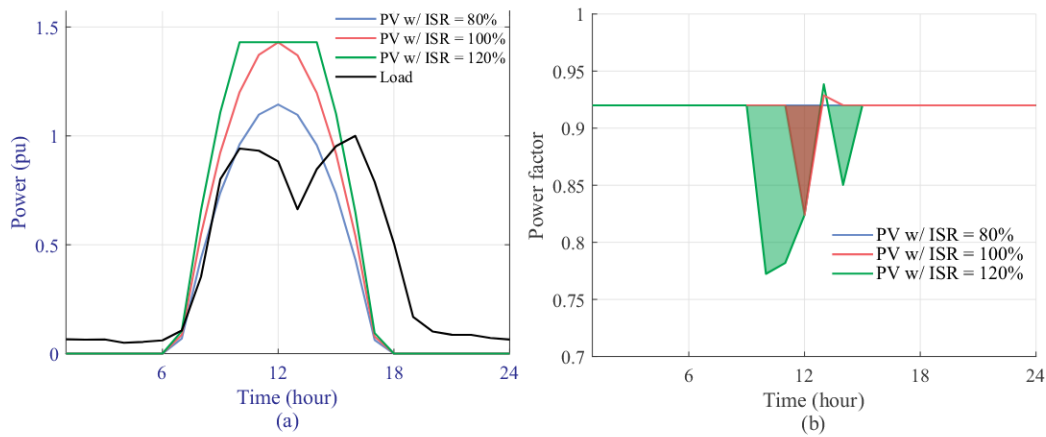
Figure 4.13: Impact of inverter sizing ration on the power factor: (a) PV system and load active power and (b) power factor under different ISR conditions.

Tab. 4.7 presents the integral of compensated and not compensated reactive power over time for each load profile, in pu per hour. For ISR = 80%, since the PV inverter has margin to regulate the entire PF, the integral of compensated reactive power is the highest. As ISR increases, the margin reduces and so as the integral of compensated reactive power, being ISR = 120% the lowest. On the other hand, the integral of not compensated reactive power also increases with ISR.

The reactive power capability of a multifunctional PV inverter can be used to regulate the load power factor. As a drawback, the extra power processed can accelerate the components wear out process and shorten the inverter lifetime. The reliability evaluation of multifunctional PV inverters
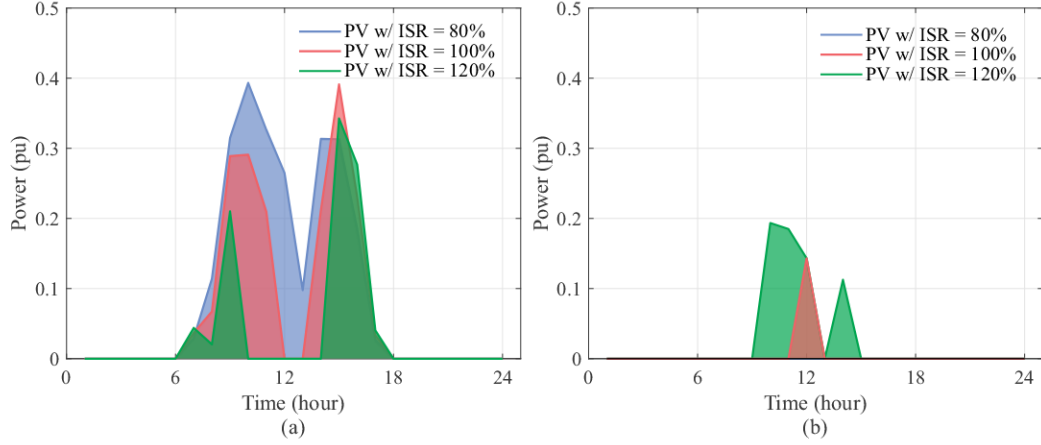
Figure 4.14: Reactive power profiles of the multifunctional PV inverter under three ISR conditions: (a) reactive power compensated by the inverter and (b) reactive power not compensated due to dynamic saturation.

Table 4.7: Integral of compensated and not compensated reactive power when the PV inverter operates as multifunctional mode. The non-compensation instances occur when there is no available power margin due to dynamic saturation.

ISR	Integral of comp. Q^* (pu.h)	Integral of not comp. Q^* (pu.h)
80%	2.3781	0
100%	1.7598	0.1431
120%	0.9340	0.6339

with reactive power support to regulate power factor will be addressed in a case study in the next chapter.

4.5   Chapter closure

This chapter discussed the reactive power as a PV inverter ancillary service. The current brazilian standard ABNT NBR 16149:2013 concerning the proceedings of the inverter interconnection with the electrical grid is not updated yet to provide technical guidance for reactive power support. On the other hand, the international IEEE 1547:2018 is a well established standard that already includes PV inverters reactive power capability to support the

electrical grid. Nevertheless, this thesis proposed to investigate a full reactive power capability, with inverter power factor varying from 0 to 1, apart from what brazilian standard suggests.

However, if a full reactive power capability is explored in a multifunctional PV inverter, it may lead the system to fail prematurely. Therefore, a derating on the reactive power reference is proposed to partially compensated the reactive power. The trade-off between the inverter reliability and the amount of not compensated reactive power will be addressed on the next chapter of this thesis. In addition, a case study will employ the multifunctional PV inverter to regulate an industry load power factor connected to the PCC.

Reliability analysis of a multifunctional PV inverter with reactive power capability

This chapter applies the reliability evaluation process in a case study to investigate the impacts of reactive power compensation on the lifetime of a multifunctional PV inverter. The reactive power support capability is explored in a range of inverter sizing ratio conditions. The trade-off between reactive power and lifetime consumption is economically analyzed by the Levelized Cost of Electricity (LCOE). Finally, the multifunctional PV inverter is applied to an industry power factor regulation case study to evaluate its reliability while performing this ancillary service.

5.1 Case study: Lifetime evaluation applied to reactive power profile compensation

The PV inverter topology and specification used in this case study is the same as defined in Chapter 3. Although the PV module operating temperature is calculated through Ross' expression, no thermal dynamics is considered. Despite being a more realistic estimation, neglecting the PV module thermal capacitance in the range of the time constant found in the literature does not impact the lifetime prediction. On the other hand, this consideration may reduce the computational efforts and result in time

saving while running the simulations.

The results of this case study is divided in three parts. Initially, a conventional PV inverter is taken as base case and its lifetime is compared to a multifunctional PV inverter while compensating a reactive power profile. In the following analysis, the same reactive power profile is submitted to a derating factor and the PV inverter partially compensates the reactive power in order to achieve a reliability requirement. In the final part, an economic analysis based on LCOE is provided to compare the PV inverter operation under inverter sizing ratio and reactive power derating factor variations.

5.1.1 PV inverter lifetime under full reactive power compensation

The profile used as reactive power reference in the control of the PV inverter is presented in Fig. 5.1 (a). This is the load required reactive power profile, measured in a food industry in Brazil during one month with sample time of 1 minute. The data is replicated to have an entire year long profile. Note that the maximum reactive power condition, i.e., 12 kvar, is normalized to the inverter specification. This condition represents a full capacity of the inverter to compensate reactive power with a power factor excursion from 0 to 1. However, since the inverter dynamic saturation limits the total apparent power, eventually the PV inverter would not have margin to compensate the entire profile. Nevertheless, the full reactive power compensation expression refers to the capability of the inverter to provide $Q^* = S_n$ when $P_{pv} = 0$.

The reactive power compensation increases the PV inverter apparent power, as shown in Fig. 5.1 (b) for Goiânia as an example. As a consequence, the inverter components are more stressed. Fig. 5.2 shows the components temperature with the PV inverter operating as conventional and multifunctional mode. The maximum junction temperature on the inverter IGBT S_{1-6} is considered as the upper envelop of the mean junction profile summed with half of the junction temperature variation:

$$T_{j,max} = T_{jm} + \frac{\Delta T_j}{2}. \tag{5.1}$$
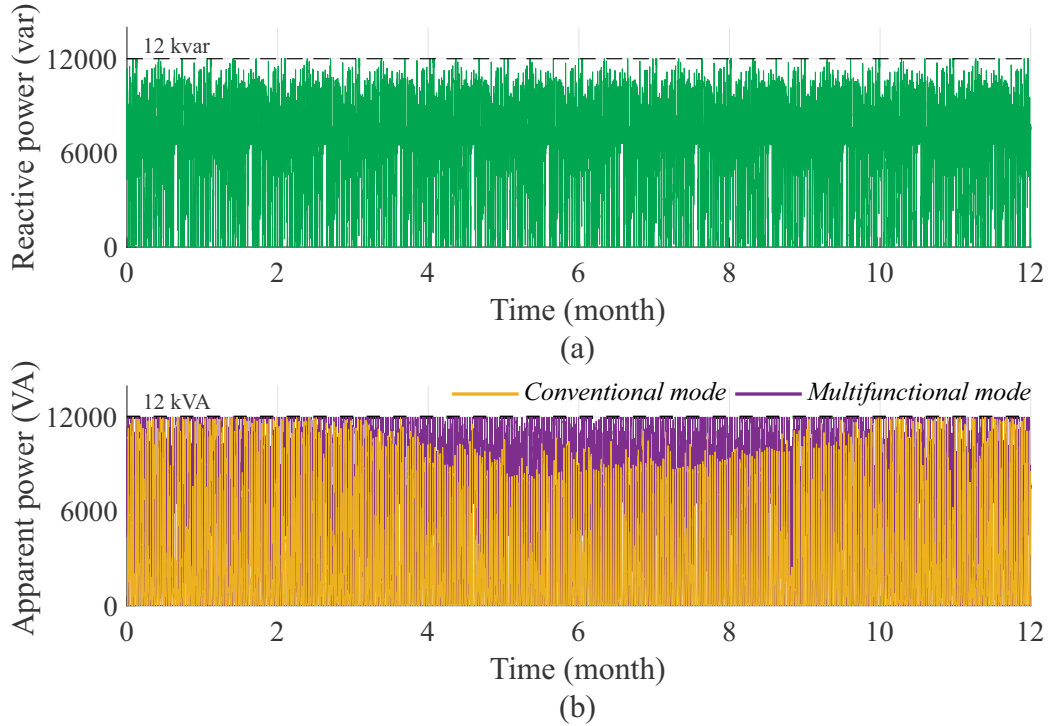
Figure 5.1: (a) Load required reactive power profile, sampled at 1 min during one
year of measurements in a real food industry in Brazil and (b) apparent
power profile of the PV inverter from Goiânia operating as conventional
and multifunctional mode.

Note that the boost converter IGBT S_b junction temperature profile is the
mean value, since there is no cyclic variations caused by the fundamental
frequency, i.e., $T_{j,max} = T_{jm}$.

The histograms show that, under reactive power compensation, the
components temperature are displaced to higher temperature levels, except
C_b, since no extra power losses are processed by the boost converter input
capacitor due to reactive power compensation. However, the boost
converter IGBT S_b is also submitted to higher junction temperature even
having no dependence with the displacing angle θ. This fact is explained by
the shared thermal coupling network with the inverter IGBT, which
elevates the heatsink temperature.

The PV inverter components static lifetime consumption during
conventional and multifunctional operation are presented in Tab. 5.1.
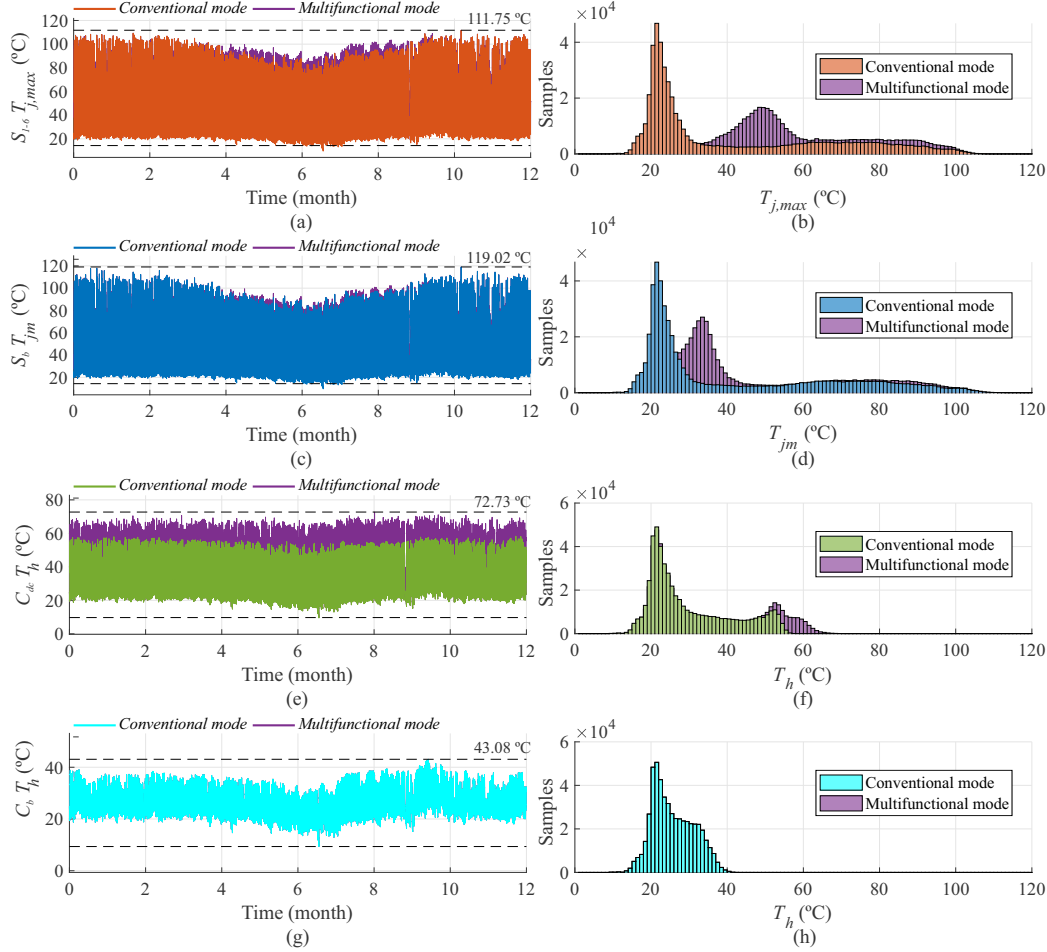
Figure 5.2: Thermal loading of the dc-dc and dc-ac stage components with PV inverter operating as conventional mode and multifuctional mode (with reactive power compensation): (a) S_{1-6} maximum junction temperature profile, (b) histogram of S_{1-6} maximum junction temperature, (c) S_b mean junction temperature profile, (d) histogram of S_b mean junction temperature, (e) C_{dc} hot-spot temperature profile, (f) histogram of C_{dc} hot-spot temperature, (g) C_b hot-spot temperature profile, (f) histogram of C_b hot-spot temperature.

Among the components, the inverter IGBT S_{1-6} is the most stressed during multifunctional case. It is interesting to note that, in conventional case, S_{1-6} from Izaña is the most stressed among the three regions. However, in multifunctional case, the inverter IGBT from Goiânia presents the highest LC. This fact is explained by the amount of compensated reactive power,

which is greater for Goiânia due to more power margin available. Other interesting fact is the reduction of LC from the boost converter IGBT, even operating with higher mean junction temperature. Since the thermal design is made considering the worst power losses condition, the reactive power compensation does not increase the maximum junction temperature. However, since the mean junction temperature is increased, the IGBT are submitted to lower long-term thermal cyclic, which reduces the lifetime consumption.

Table 5.1: Components lifetime consumption under conventional and multifunctional PV inverter operation. LC values in power of 10^{-3}.

Mission	Conventional mode				Multifunctional mode			
profile	S_b	C_b	S_{1-6}	C_{dc}	S_b	C_b	S_{1-6}	C_{dc}
Aalborg	1.63	4.53	12.53	10.76	1.34	4.53	32.78	20.05
Goiânia	3.33	13.86	31.15	29.95	2.88	13.86	74.83	58.06
Izaña	1.21	7.11	36.99	25.11	1.18	7.11	62.63	40.44

Fig. 5.3 shows the lifetime histogram of the S_{1-6} and C_{dc} for all three regions, after the Monte Carlo simulations are performed with the same parameter variation stated in Tab. 3.4. Independent of the region, the reactive power compensation lead the components to fail earlier than the base case. In terms of system lifetime, Fig. 5.4 presents the unreliability functions and the B_{10} lifetime are stated in Tab. 5.2. If a lifetime requirement of 10 years is defined, only the PV inverter installed in Aalborg would last longer than the target. As a conclusion, a full reactive power compensation may lead the multifunctional operation of the PV inverter to be less attractive.

Table 5.2: Lifetime B_{10} in years for all three regions, with PV inverter in conventional and multifunctinoal mode.

Mission	Lifetime B_{10} (years)	
profile	Conventional mode	Multifunctional mode
Aalborg	37.6	14.4
Goiânia	16.2	6.8
Izaña	12.2	7.2
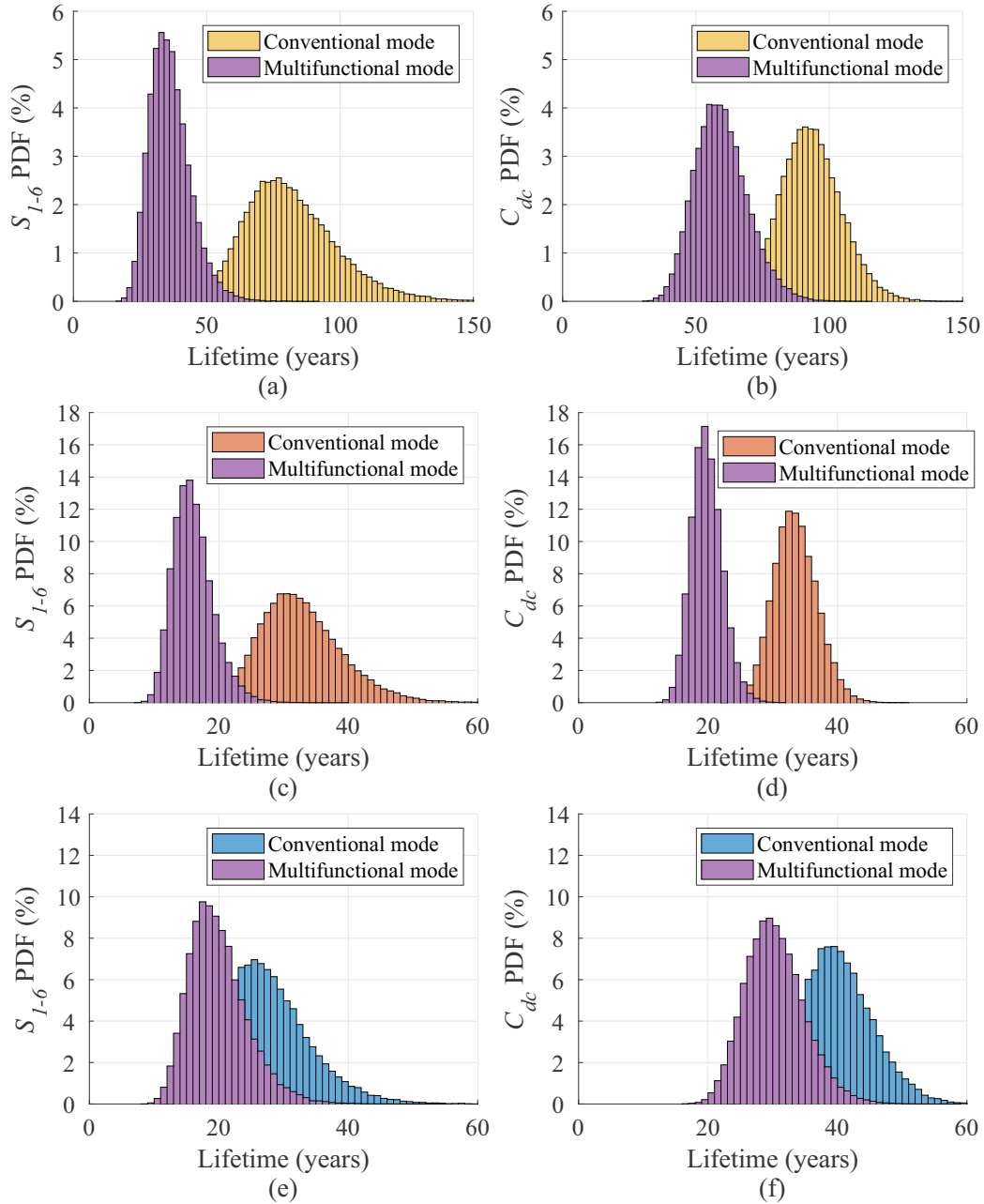
Figure 5.3: Lifetime histogram from Monte Carlo simulations with 50,000 samples: (a) inverter IGBT S_{1-6} and (b) inverter dc-link capacitor C_{dc} from Aalborg; (c) inverter IGBT S_{1-6} and (d) inverter dc-link capacitor C_{dc} from Goiânia; (e) inverter IGBT S_{1-6} and (f) inverter dc-link capacitor C_{dc} from Izaña.
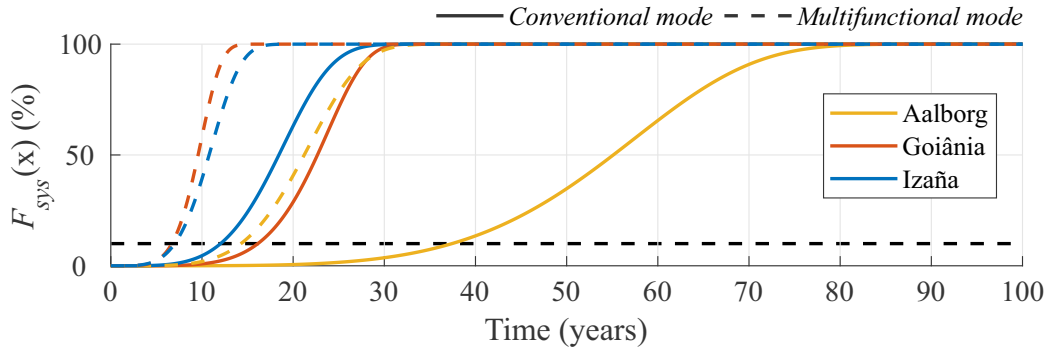
Figure 5.4: System-level unreliability function for all three regions, with PV inverter in conventional and multifunctional mode.

5.1.2 PV inverter lifetime under partial reactive power compensation

The second analysis investigates the variations of the inverter sizing ratio ISR and reactive power derating Q_R to make the reactive power compensation reach the desired lifetime target. In the case of ISR = 100%, there are 12 PV modules connected to each MPPT input, totalizing 48 modules and 12 kWp. The variations on the ISR are performed changing the number of series PV modules in each MPPT input. Therefore, adding/removing 4 PV modules represents 8.33% minimum ISR step change.

The annual generated energy from each mission profile as a function of the inverter sizing ratio is presented in Fig. 5.5 (a). The correct choice of which ISR should be employed in each region is not straightforward. In terms of energy, PV systems installed in Izaña with ISR lower than 100 % can be applied to avoid wasted energy due to dynamic saturation. In the same sense, ISR higher than 100 % can be applied in Aalborg to increase the annual generated energy. However, other important factors must be taken into account, such as reliability and economic metrics. In fact, there is a trade-off related to the total generated energy with the reliability, which impacts the system overall costs. In terms of reactive power, higher ISR conditions also reduces the power margin that the PV inverter has to operate. Fig. 5.5 (b) shows the integral of the compensated reactive power over time for the three regions. Since the increase of ISR reduces the reactive power margin, there is a combined effect on the damage that should be careful

analyzed.
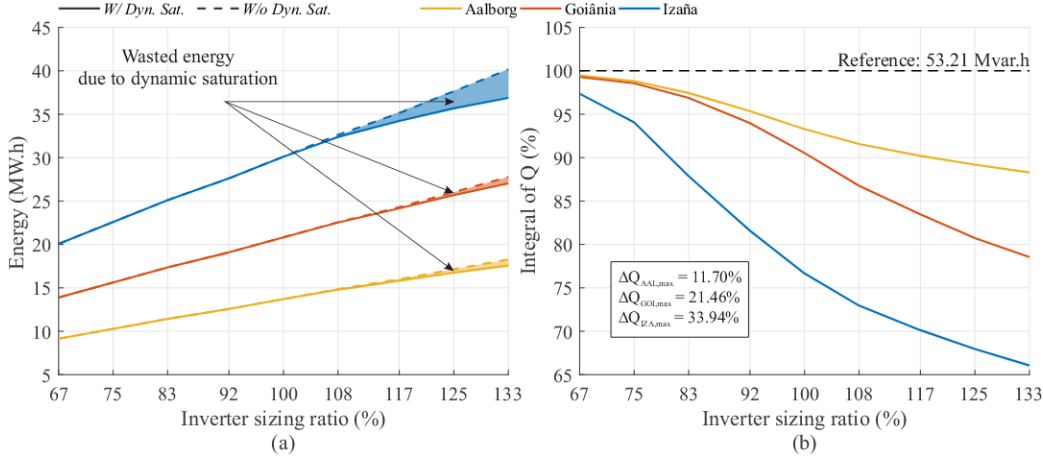
Figure 5.5: Effects of inverter sizing ratio on the PV inverter for all three mission profiles: (a) annual generated energy and (b) integral of compensated reactive power over time. Note that ISR = 100% correspond to the base case, i.e., P_{pv} = 12 kWp.

Fig. 5.6 shows the static lifetime consumption of the inverter IGBT S_{1-6} and the dc-link capacitor C_{dc} as a function of the ISR, for conventional and multifunctional PV inverter operation. As ISR increases, the PV inverter processes more energy and the components are more stressed. In the same way, when the reactive power is compensated, the extra power losses on the components also increases the LC. It is worth noticing that the IGBT are more sensitive to reactive power processing than capacitors, having larger differences between conventional and multifuncitional operation.

In a reliability oriented design, the PV inverter can operate under different combinations of ISR and Q_R to achieve a desired lifetime target, e.g., 10 years. Fig. 5.7 (a) presents the unreliability curves of the PV inverter from Goiânia, compensating the original reactive power profile (Q_R = 100 %). On the other hand, Fig. 5.7 (b) provides the unreliability curves for the same PV inverter when it partially compensates the reactive power profile for ISR = 100 %. As can be seen, there are different conditions of ISR and Q_R where the target lifetime is not respected. Tab. 5.3 and 5.4 details the lifetime B_{10} for all three mission profiles as a function of ISR and Q_R, respectively. As a conclusion, the correct choice of ISR and Q_R can be used to move the system-level B_{10} back and forth from the conventional
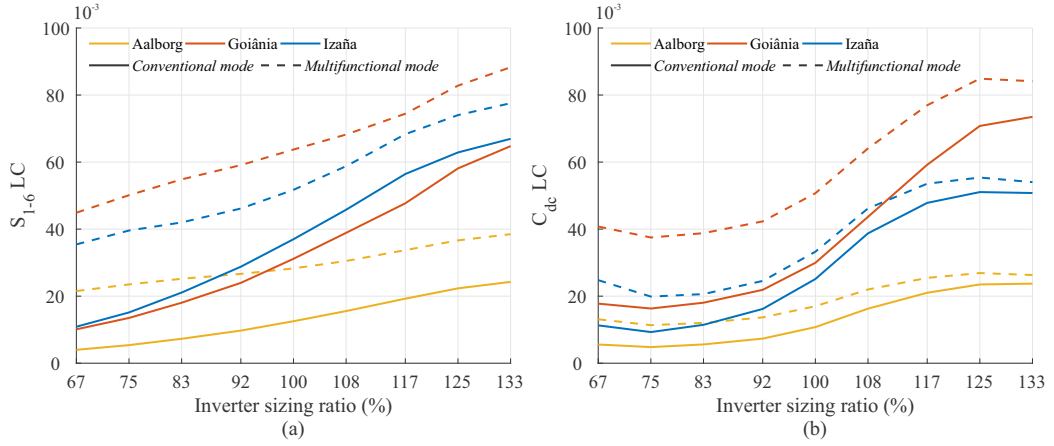
Figure 5.6: Effects of inverter sizing ratio on the PV inverter most stressed components lifetime consumption: (a) inverter IGBT S_{1-6} and (b) dc-link capacitor C_{dc}. The conventional operation of the PV inverter is compared with the multifunctional mode with reactive power capability.
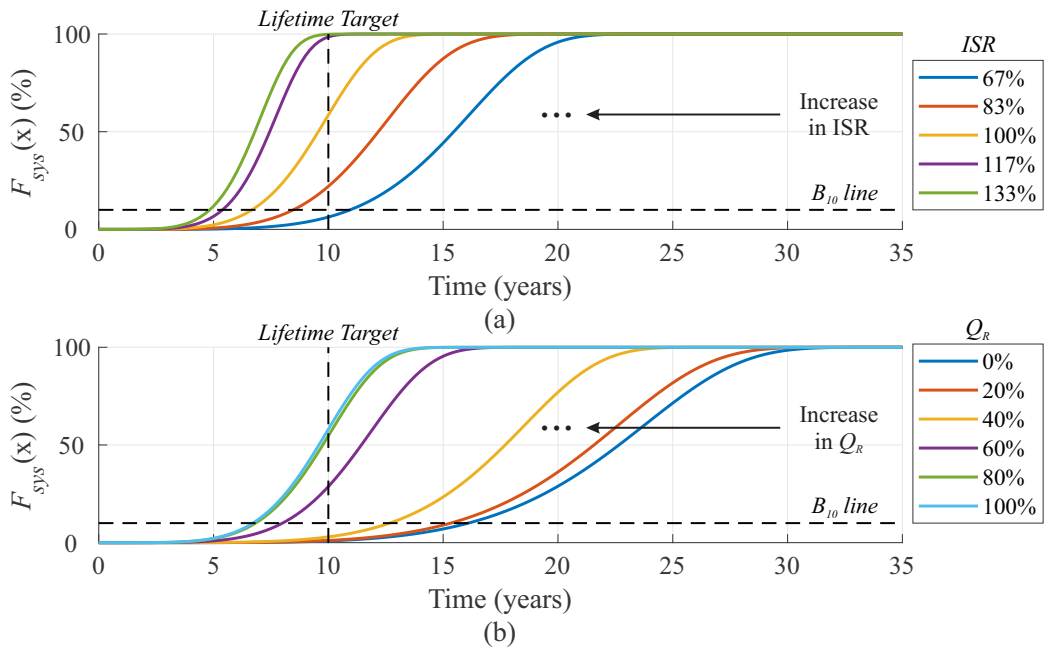
Figure 5.7: PV inverter unreliability function at system-level: (a) different values of ISR when compensating reactive power profile with $Q_R = 100\%$ and (b) different reactive power derating factors for ISR $= 100\%$.

operation to partial or full reactive power compensation.

Table 5.3: Lifetime B_{10} in years for all three regions, with PV inverter under inverter sizing ratio variations. The PV inverter is operating as multifunctional with $Q_R = 100\%$.

Mission profile	B_{10} lifetime (years) for ISR variation.								
	67%	75%	83%	92%	100%	108%	117%	125%	133%
Aalborg	21.4	19.4	17.2	15.6	14.4	12.8	11.6	11.4	11.0
Goiânia	11.0	9.8	8.6	7.6	6.8	6.2	5.4	5.2	5.0
Izaña	12.0	10.0	8.6	7.8	7.2	6.6	5.8	5.6	5.4

Table 5.4: Lifetime B_{10} in years for all three regions, with PV inverter under partial reactive power compensation. The PV inverter is operating with ISR = 100%.

Mission profile	B_{10} lifetime (years) for Q_R variation.										
	0%	10%	20%	30%	40%	50%	60%	70%	80%	90%	100%
Aalborg	37.6	37.2	35.0	31.4	27.8	21.4	17.4	15.2	14.8	14.6	14.4
Goiânia	16.2	16.0	15.4	14.0	12.8	10.0	8.2	7.4	7.2	7.0	6.8
Izaña	12.2	12.0	11.6	10.6	10.0	8.6	7.8	7.4	7.2	7.2	7.2

An alternative way to evaluate the reliability of the PV inverter under different operating conditions is to target both lifetime and unreliability. Fig. 5.8 presents an unreliability map from Goiânia, where $U(x)$ represents the percentage of samples that fail in the targeted lifetime. Considering the conventional operation with ISR = 100%, around 1% of the samples would fail in 10 years. On the other hand, when the full reactive power profile is employed, i.e., $Q_R = 100\%$, more than 50 % of the samples would have failed in that time, making this kind of operation unfeasible and unrealistic.

An unreliability target U_x can be used to define the PV inverter feasibility for a specific lifetime target. In the case study, if a conservative approach is considered, i.e., $U_1 = 1\%$, the PV inverter in conventional case cannot operate with ISR greater than 100%. In addition, none of the ISR values in the investigated range would present unreliability below 1% in the multifunctional operation with $Q_R = 100\%$. If a broader approach is applied, i.e., $U_{10} = 10\%$, the PV inverter should operate below ISR = 115% in conventional mode and 73% in multifunctional mode with $Q_R = 100\%$.
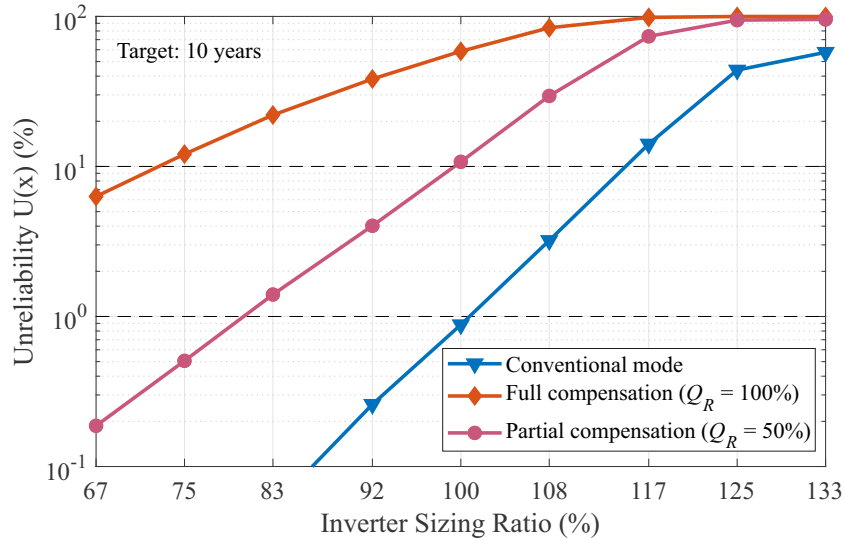
Figure 5.8: Unreliability map as function of ISR for a lifetime target of 10 years.

However, one of the advantages of the unreliability map is to find an intermediary condition where the PV inverter can partially compensates the reactive power, as well as achieve both lifetime and unreliability requirements. In this case study, for ISR = 100%, and considering U_{10}, the PV inverter would meet the targeted lifetime under partial reactive power compensation with $Q_R = 50$ %. Thus, the unreliability map can be an important tool to determine the reactive power margin as a function of ISR, in agreement with unreliability and lifetime targets.

As a conclusion, a conventional PV inverter with a defined power specification, i.e., 12 kVA for the case study, would have a lower reactive power specification if multifunctional operation is employed. In other words, the analyzed 12 kVA PV inverter had only 6 kvar specification, if the desired reliability target is 10 % in 10 years. This conclusion is a function of the employed mission profile. Nevertheless, the possibility of reducing the PV inverter reactive power margin to reduce the trade-off with lifetime reduction is an important solution to improve multifunctional operation attractiveness and feasibility.

The unreliability map can be expanded to an unreliability surface that carries a more complete analysis in function of ISR and Q_R. Fig. 5.9 shows the unreliability surface from Goiânia. The two $U(x)$ targets are marked as

white dashed lines. It is important to note that this map can be extrapolated to different unreliability and lifetime targets. Therefore, the reliability designers and PV inverter manufacturers can make use of this map to define feasible and cost-efficient operation with full or partial reactive power compensation. Furthermore, the definition of the unreliability target depends on how reliable the manufacturer wants to do their converters. Thereby, the reliability engineer can define the reliability target in function of system design, converter specifications, mission profiles and reactive power capability.
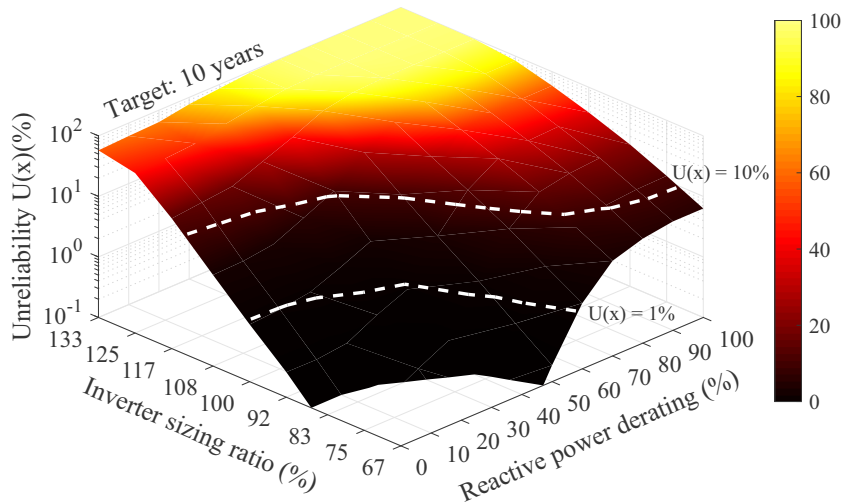
Figure 5.9: Unreliability map surface in function of ISR and Q_R for a lifetime target of 10 years.

5.1.3 LCOE applied to multifunctional PV inverter under variations of ISR and Q_R

The Levelized Cost of Electricity (LCOE) is a common approach to compare different electrical energy sources in a fair and normalized index (Moradi-Shahrbabak; Tabesh; Yousefi, 2014). The unit of LCOE is \$/Wh, which relates the sum of the costs with the total generated energy over the system useful life. From Gandhi et al. (2019), a generic and simplified method to calculate LCOE is given by:

$$LCOE = \frac{EPCI + \sum_{n=1}^{N} \frac{OM}{(1+DR)^n} + \sum_{n=1}^{N} \frac{IRI_n}{(1+DR)^n}}{\sum_{n=1}^{N} \frac{EP_n(1-SDR)^n}{(1+DR)^n}}, \tag{5.2}$$

where EPCI is the equity project cost investment with the PV system, N is the PV system expected useful life, OM is the operational maintenance, DR is the discount rate, IRI is the inverter replacement investment, EP is the energy produced over each year and SDR is the system degradation rate. Tab. 5.5 presents the values used in this LCOE analysis. For simplicity, other variables such as interest during construction, insurance costs, loan payments and residual value are not considered. More information about a more complete LCOE calculation can be found in (Gandhi et al., 2019).

Table 5.5: LCOE parameters applied to the case study. Note that EPCI = 1 pu represents the case of ISR = 100%. The variations on ISR change the number of PV modules, which also impacts EPCI.

Parameters	Value
EPCI	1 pu*
N	20 years
OM	4% of EPCI per year
DR	3.75% per year
IRI	0.30 discounted by DR over time
EP	calculated in function of MP
SDR	1% per year

*1 pu: modules (0.40 pu) + inverter (0.30 pu) + structure (0.10 pu) + installation (0.10 pu) + additional costs (0.10 pu).

First of all, it is important to differ N and IRI, since both of them are related to lifetime expectations. N is the entire PV system expected useful life (including modules), i.e., the total years of energy production. On the other hand, IRI represents the inverter replacement investment due to failure. Therefore, if the PV inverter lifetime is lower than N, IRI count as additional costs in LCOE due to inverter replacement (IR). The lower is the PV inverter lifetime, the higher is the number of IR, corresponding to higher IRI. In addition, for PV inverter lifetime between 10 and 20 years, there will be only one replacement over the system useful life (N = 20). However, since the investment is discounted by DR over time, the higher is the PV inverter lifetime, the lower is the cost with replacements.

The LCOE index is used in this analysis to economically compare the costs of the PV system under different operational conditions, i.e., ISR and Q_R. Both ISR and Q_R may impact the PV system LCOE. Initially, since the ISR variation is performed changing the number of installed PV modules, the EPCI would change. In addition, ISR varies the produced energy, which also affects the LCOE. On the other hand, when variations on Q_R are performed keeping ISR constant, the only effect on LCOE is in IRI. If the PV inverter lifetime is reduced, either by ISR or Q_R, LCOE should increase and make the system less competitive when compared to the conventional operation.

Fig. 5.10 shows the LCOE curves for the PV system installed in Goiânia under conventional operation, i.e., $Q_R = 0$ % and with full reactive power compensation, i.e., $Q_R = 100$ %. The ISR increase has a negative effect on LCOE by inserting extra costs due to additional PV modules and a positive effect by also increasing the produced energy. The effect of generating more energy overcomes the additional costs with PV modules. However, since the increase of ISR reduces the inverter lifetime, eventually the number of inverter replacements would increase, as can be seen in the bars on the bottom of Fig. 5.10. Moreover, when IR increases, the LCOE increases in relation to the previous point of the curve. If the number of inverter replacements does not change from two consecutive ISR conditions, LCOE reduces, making the system economically more attractive. It is important to note that the LCOE of the PV system with reactive power compensation is higher than the conventional system for every ISR condition. As expected, there is an increase in the system costs when the reactive power is provided by the PV inverter. In comparison with the reference value, this increase is 18.7% for ISR = 100%.

The costs with reactive power support can be reduced if the reactive power profile is partially compensated. In Fig. 5.11, the LCOE curves of ISR = 100% and 110% are presented for Q_R varying from 0 to 100%. In these curves, the LCOE are only affected by the increase in IR due to PV inverter lifetime reduction. As expected, as Q_R increases, the LCOE of the PV inverter also increases. When comparing two ISR conditions, if the number of inverter replacements are the same, the curve with higher ISR has lower LCOE due to more energy generated. However, as can be seen, the curve with higher ISR is also more likely to present higher IR, and thus, higher LCOE.
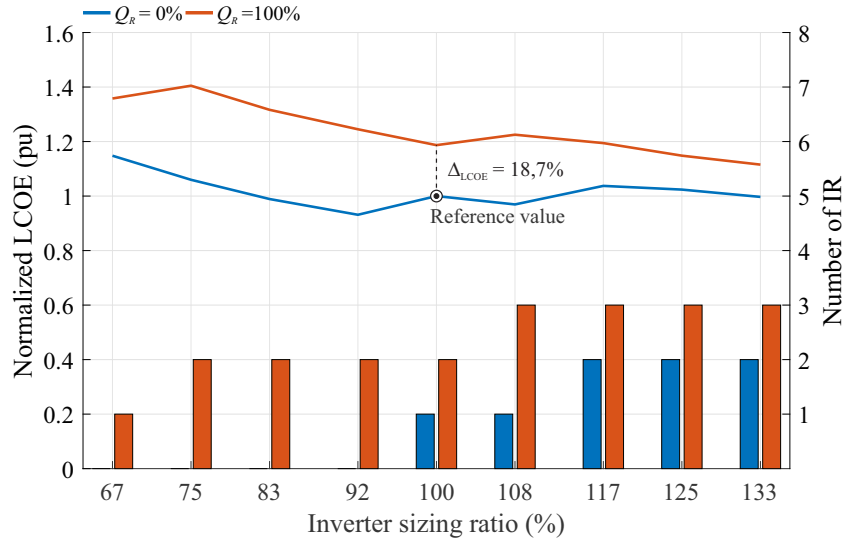
Figure 5.10: Normalized LCOE (left axes) and number of inverter replacements (right axes) from Goiânia as a function of ISR. Two Q_R conditions are presented (0% and 100%). The curves are normalized by the reference value, which is the LCOE for conventional PV inverter operation (ISR = 100% and Q_R = 0%).

As expected, the inverter lifetime reduction represents economic losses, reducing the system attractiveness and competitiveness. Therefore, economic incentives must be provided to overcome the reduction of lifetime when the PV inverter compensates reactive power. Furthermore, when the reactive power profile is partially compensated, there is also another trade-off related to the amount of not compensated reactive power. This amount is dependent of either ISR or Q_R and should be included in a more complete economic analysis.

5.2 Case study: Lifetime evaluation applied to power factor regulation

The reactive power capability of a multifunctional PV inverter is now applied to a case study to regulate the power factor of a local industry load. Once again, the PV inverter topology and specification used in this case study is defined in Chapter 3. Moreover, since a deep analysis of the reactive power
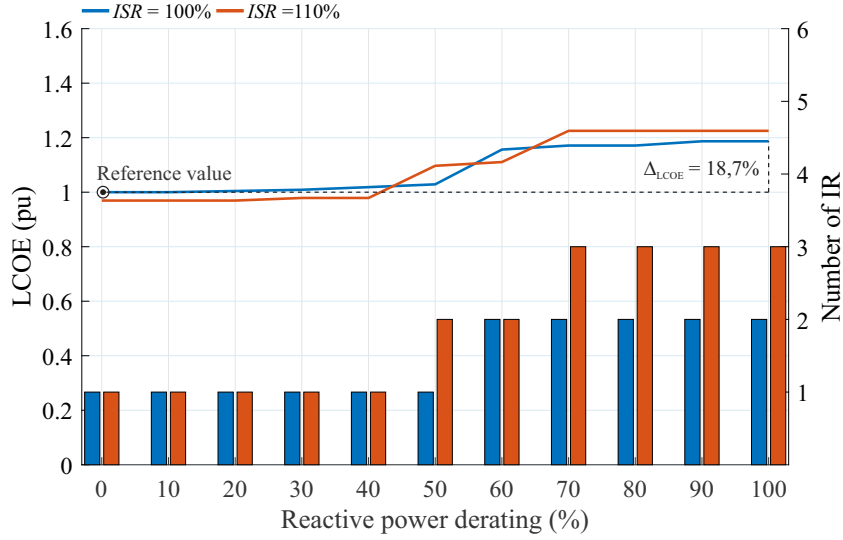
Figure 5.11: Normalized LCOE (left axes) and number of inverter replacements (right axes) for Goiânia - Brazil and Q_R varying from 0 to 100 %. Two ISR conditions are presented (100 % and 110 %). The curves are normalized by the reference value, which is the LCOE for ISR = 100 % and Q_R = 0 %.

capability from different regions was developed in the previous section, only the mission profile from Goiânia will be investigated in this case study.

The load profile is obtained from seven days of measurements with sample time of 1 minute, at a food processing industry in Brazil. The data is then replicated to obtain an one-year long profile. In addition, there is only industry activity between 5:30 AM and 5:30 PM, representing a commercial worktime. The active and reactive power profiles of the local industry load are shown in Fig. 5.12 (a). These profiles represent a poor power factor operation, as shown in Fig. 5.12 (b). As can be seen, all the points are below the reference required by the electric power system operator. Moreover, this industry does not have any other reactive power compensator to regulate its power factor, such as capacitor banks.

The PV inverter in this application is connected to the low-voltage electrical grid. According to the Brazilian standard, industrial loads connected to low voltage systems are not charged by excessive reactive power consumption. However, this industrial load is part of a bigger

system, fed with medium voltage, and it should regulate its power factor. Therefore, the PV inverter operating as multifunctional with reactive power compensation can support this system with reactive power.
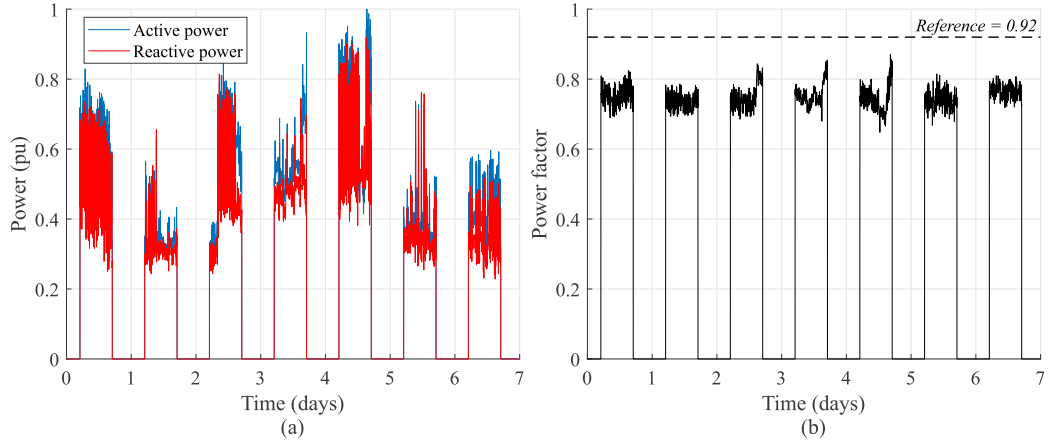
Figure 5.12: Industrial local load containing seven days with daily working time starting from 5 AM to 5 PM: (a) active and reactive power profile and (b) power factor profile. Data sampled at 1 min.

The multifunctional PV inverter is connected to the grid on the PCC aside with the load, to regulate its power factor above the reference or close to it, avoiding the facility owner to be charged due to lower PF operation. The PV system is initially sized with ISR = 100% of the inverter apparent power, i.e., 12 kWp. The load power profiles are scaled as follows:

$$P_{load} = \left(Ek_L \frac{E_{pv}}{E_{load,pu}} \right) P_{load,pu}, \tag{5.3}$$

$$Q_{load} = \left(Ek_L \frac{E_{pv}}{E_{load,pu}} \right) Q_{load,pu}, \tag{5.4}$$

where E_{pv} and $E_{load,pu}$ are the annual generated energy by the PV system and the annual energy consumed by the load profile (in pu), respectively. P_{load} and Q_{load} represent the active and reactive power points that are scaled by the factor Ek_L. In this scenario, three case studies are considered:

- $Ek_L = 0.5$, meaning that the load consumes half of the total energy produced by the PV system over the year;

- $Ek_L = 1.0$, meaning that all the energy generated by the PV system over the year is consumed by the load;

- $Ek_L = 1.5$, meaning that the load energy consumption is 50% higher than the energy generated by the PV system over the year.

The three cases are illustrated in Fig. 5.13.
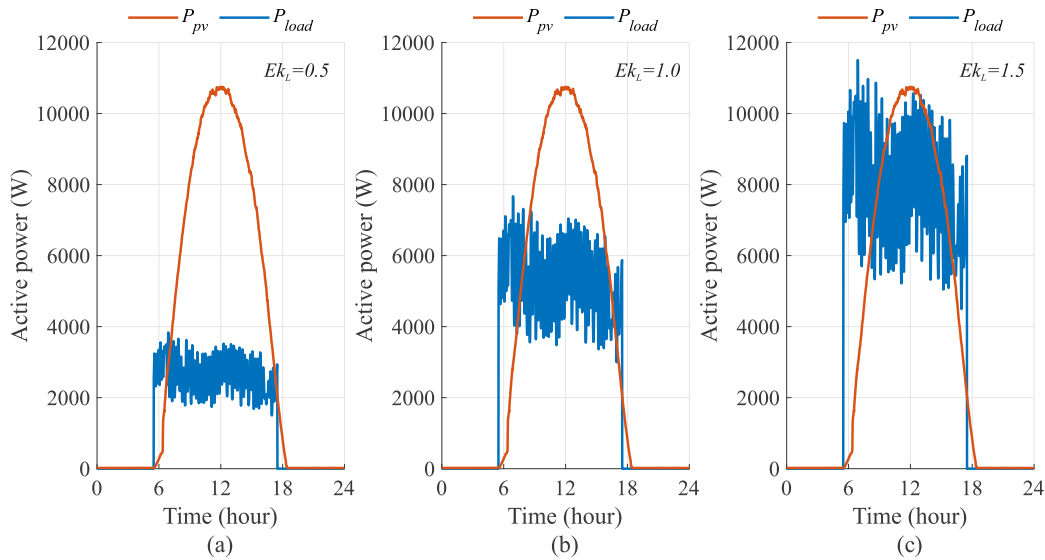
Figure 5.13: Typical daily PV generation and load consumption for the case studies: (a) $Ek_L = 0.5$, (b) $Ek_L = 1.0$, (c) $Ek_L = 1.5$.

5.2.1   Effects of the PV system connection on the grid power factor

Fig. 5.14 (a)-(c) show the power factor of a typical day of the mission profile to illustrate what happens when the PV system is connected to the grid, for all three cases of Ek_L. The active power that flows to/from the grid is the difference between the PV system generation and the load consumption. Therefore, the higher is the liquid active power, the higher is the power factor. However, if the instantaneous P_{pv} is close to P_{load}, the liquid active power becomes close to zero and the power factor tends to zero.

The histogram in Fig. 5.14 (d) shows the percentage distribution of the PF from the annual mission profile. Before the connection of the PV inverter, the maximum power factor point was around 0.8. However, for Ek_L = 0.5, 31.48% of the samples are above the reference after the PV system connection. This occurs because of the large difference between the PV generation and the load consumption, which increases the grid active power. On the other hand, for Ek_L = 1.0 and 1.5, the load active power becomes closer to the PV generation and the grid liquid active power is reduced. For all three cases, the amount of reactive power that must be compensated to ideally regulate the PF above the reference is 4.14, 12.60 and 20.40 Mvar.h, respectively for Ek_L = 0.5, 1.0 and 1.5.

Fig. 5.15 (a)-(c) show the same typical day power factor, but now with the PV inverter compensating the reactive power to regulate it. As can be seen, for low Ek_L condition, the PV inverter has more margin to compensate reactive power and the power factor can be better regulated. However, when Ek_L = 1.5 for example, there are several points below PF reference and they occur specifically when P_{pv} is high and the grid liquid active power is very low. In this case, the PV inverter must have to compensate almost the entire load reactive power profile, but with low margin due to high PV active power generation. The histogram in Fig. 5.15 (d) shows the percentage of not compensated reactive power over the mission profile. As expected, the PV inverter is capable of compensating 100% of the 4.14 Mvar.h needed for Ek_L = 0.5 and it leaves only 0.17% of that 12.60 Mvar.h from Ek_L = 1.0 without compensation. Finally, when Ek_L = 1.5, the PV inverter cannot compensate 2.15% from a total of 20.40 Mvar.h.

5.2.2 Lifetime evaluation and economical analysis of the PV inverter regulating the power factor

The unreliability curves of the multifunctional PV inverter regulating the power factor of the proposed case studies are presented in Fig. 5.16. The higher Ek_L, the lower the systel-level lifetime based on B_{10}, which makes sense as the PV inverter processes more reactive power. It is interesting to note that for Ek_L = 0.5, the lifetime prediction (16.0 years) is nearly equal to the conventional operation (16.2 years) of the PV inverter. This
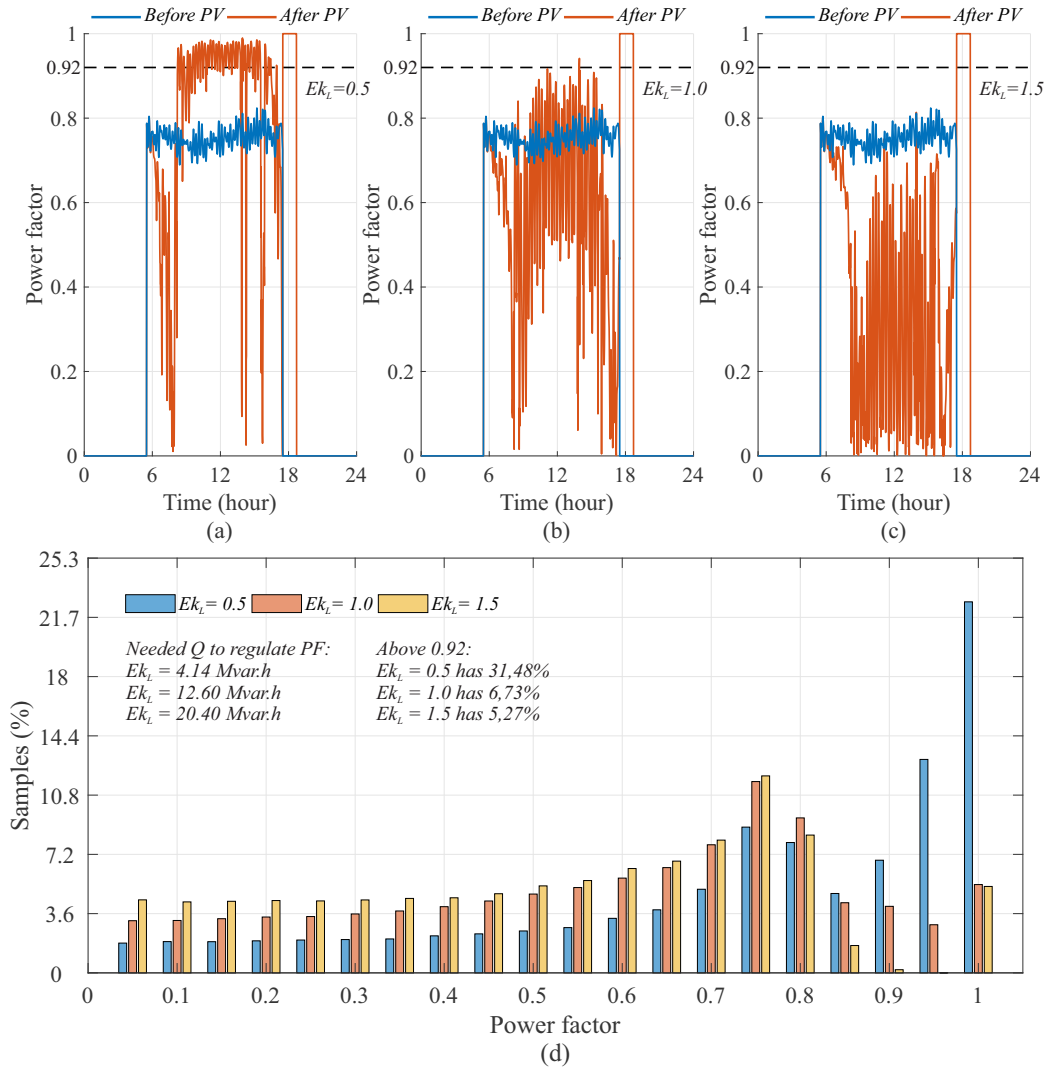
Figure 5.14: Impact of the PV system connection to the grid on the power factor as a conventional operation: (a) PF of a typical day with load profile and $Ek_L = 0.5$, (b) PF of a typical day with load profile and $Ek_L = 1.0$, (c) PF of a typical day with load profile and (d) annual power factor histogram.

means the PV inverter suffer very low extra damage while compensating that 4.14 Mvar.h needed to regulate the power factor for this case. However, the lifetime expectation for $Ek_L = 1.0$ and 1.5 is 14.2 and 10.6 years, respectively, which already reflects a relevant reduction on the system life span.

The capability of the PV inverter to regulate the power factor is also
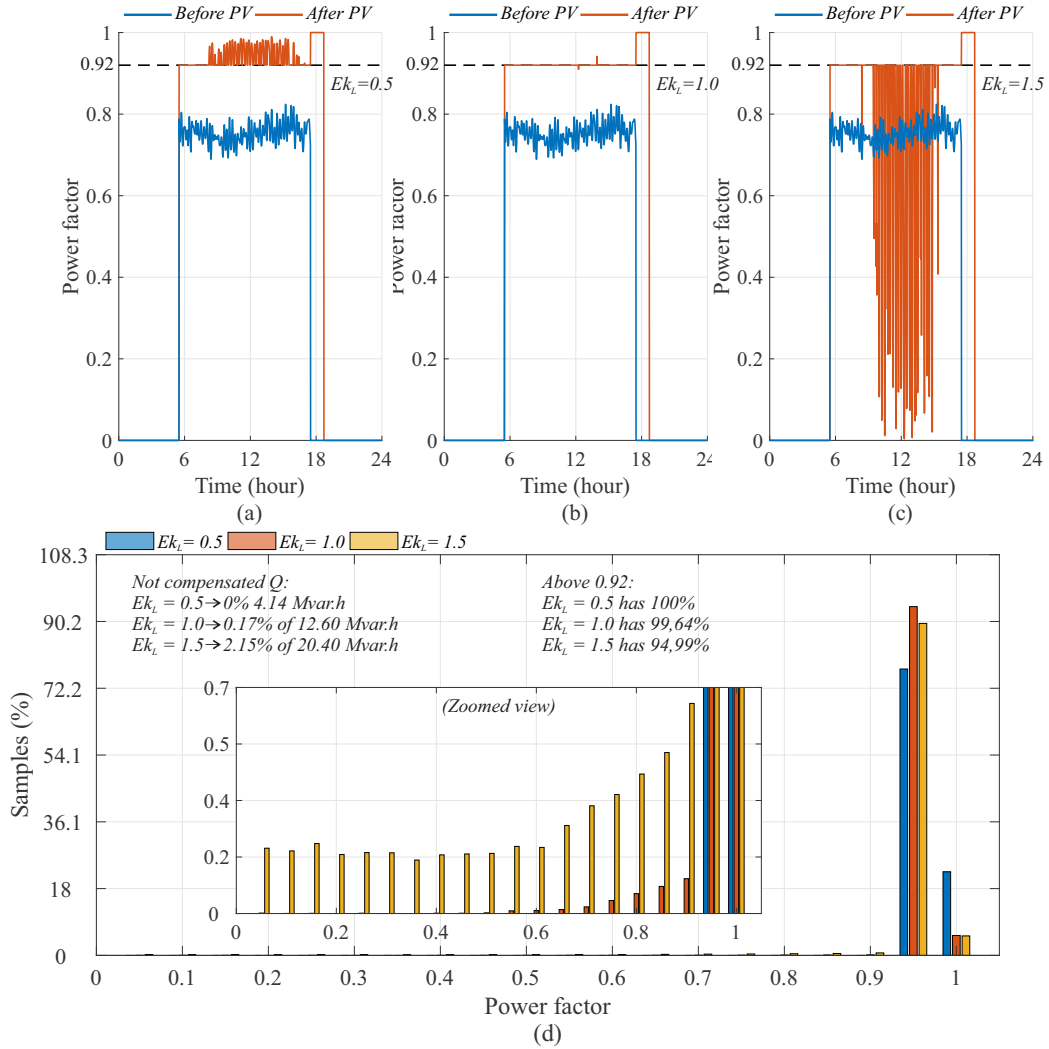
Figure 5.15: Impact of PV system connection to the grid on the power factor as multifunctional operation with reactive power support to regulate PF: (a) PF of a typical day with load profile with $Ek_L = 0.5$, (b) PF of a typical day with load profile with $Ek_L = 1.0$, (c) PF of a typical day with load profile with and (d) annual power factor histogram.

affected by the inverter sizing ratio, since it directly impacts the reactive power margin to be compensated. Fig. 5.17 (a) shows the integral of compensated and not compensated reactive power over time as function of ISR. The integral of compensated reactive power increases with the inverter sizing ratio because of E_{pv}, which also increases with ISR. For ISR lower
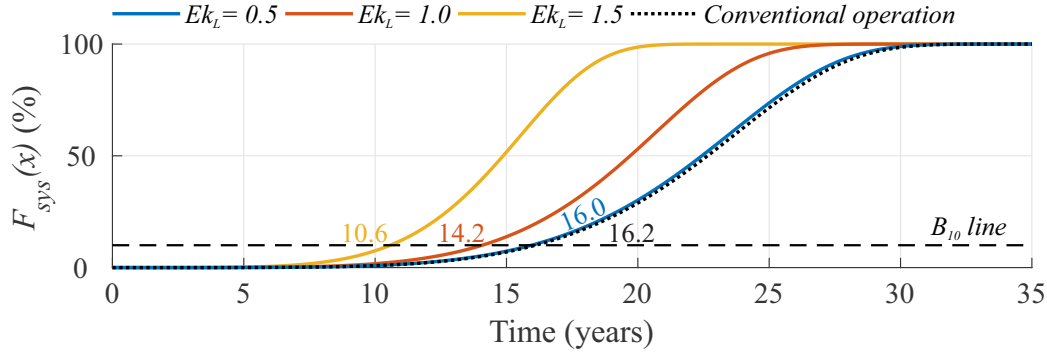
Figure 5.16: PV inverter unreliability function in system-level with multifunctional operation to regulate power factor with different load Ek_L.

than 83%, all three cases of Ek_L can compensate the total amount of reactive power needed to regulate the power factor. However, above this value, $Ek_L = 1.0$ and 1.5 start to show differences, with the last one being more accentuated. It is interesting to observe that for $Ek_L = 0.5$, the PV inverter can compensate practically most of the required reactive power for all ISR conditions. Moreover, Fig. 5.17 (b) shows the inverter lifetime expectation based on B_{10} for all three cases of Ek_L, as a function of ISR. The curves sharply decreases with ISR, showing the impact of the increased compensated reactive power by the inverter.

Finally, Fig. 5.18 shows the normalized LCOE for all three cases of Ek_L. As expected, the higher is Ek_L, the higher is LCOE, since more reactive power is compensated. Thereby, the PV inverter tends to last shorter and more inverter replacements are needed, increasing the costs. It is important to note that the extra costs with fees charged by low PF operation during not compensated reactive power points are not considered in the LCOE.

A partial reactive power compensation can also be applied on power factor regulation to improve the multifunctional PV inverter reliability. However, it is important to keep in mind that this reliability-oriented strategy can increase the amount of reactive power without compensation as a trade-off. Therefore, the partial reactive power compensation can reflect in extra costs due to lower PF operation. On the other hand, this solution can be interesting if another reactive power compensator (such as SVC or SC) would be used to help the multifunctional PV inverter to
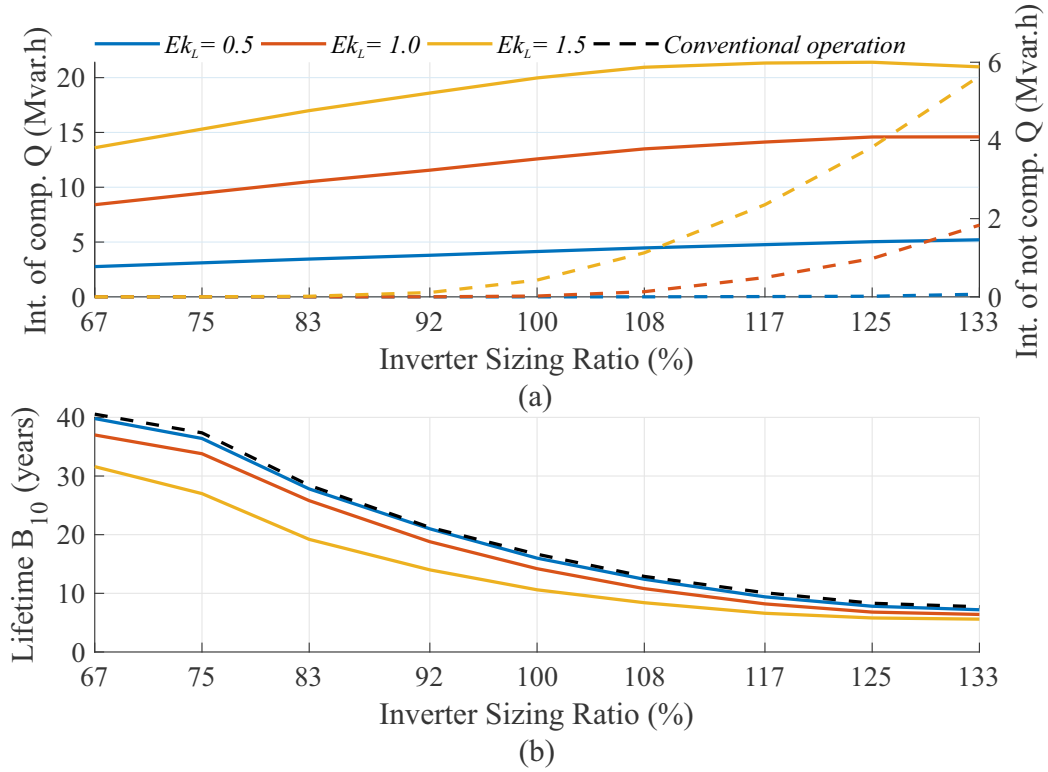
Figure 5.17: Effects of inverter sizing ratio on the multifunctional PV inverter with power regulation in function of load Ek_L: (a) integral of compensated (left) and not compensated (right) reactive power over time and (b) lifetime B_{10}.

regulate the PF. Therfore, the multifunctional PV inverter can partially compensates the reactive power, reducing the size of the other compensator. Nevertheless, a more complete economic analysis must be provided to take all these parameters into account and make the better choice of using the multifunctional PV inverter with reactive power as an ancillary service.

5.3 Chapter closure

In this chapter, the reactive power capability of a multifunctional PV inverter was applied in some case studies to evaluate the impacts on the system lifetime. Due to the increase in the components thermal loading, the
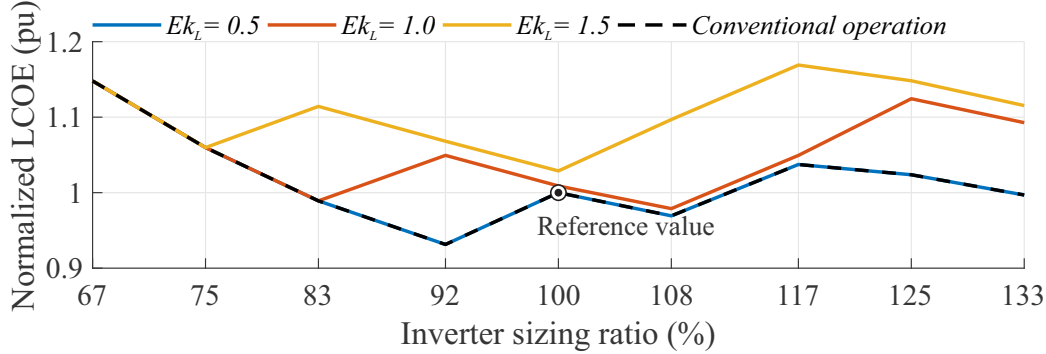
Figure 5.18: Normalized LCOE of a multifunctional PV inverter from Goiânia with power factor regulation in function of load Ek_L. The curves are normalized by the reference value, which is the LCOE for conventional PV inverter operation (ISR = 100%).

reactive power compensation can severally degrade the inverter and significantly reduce its lifetime, independent of investigated mission profiles. In this case, the multifunctional operation can become less attractive or even unfeasible due to the increased costs with inverter replacements. One possible solution is to partially provide reactive power, making the PV inverter to have a reactive power specification lower than its rated apparent power. Therefore, the presented unreliability map and its extended surface can be a very important tools to address the most suitable operation of the multifunctional PV inverter.

The multifunctional PV inverter was also used to regulate a local industry load profile, with a previous poor power factor operation. The PV inverter proved to be efficient while regulating the load PF with low energy consumption when compared to the PV system size. However, as the load energy consumption increases, the liquid active power flowing in the electrical grid is reduced, leading to a low power factor operation. In this case, the PV inverter cannot regulate the entire power factor profile due to constraints in the power margin caused by the dynamic saturation. In terms of reliability, the higher the load reactive power, the lower the PV inverter lifetime, due to the increase in the components thermal stresses.

Final conclusions

The present Ph.D thesis investigated the reliability of a multifunctional three-phase two-stage photovoltaic inverter with reactive power capability. The aim of this study is to identify the most stressed components in the PV inverter and use lifetime models to estimate the wear out during reactive power compensation. This chapter summarizes the main findings and provide possible future researches as a continuation of this work.

6.1 Thesis summary

The most important points investigated in this Ph.D thesis can be divided in three parts: sensitive analysis of meteorological conditions on the PV inverter components lifetime, reliability of PV inverters with reactive power capability and lifetime evaluation applied to power factor regulation. The most relevant conclusions of each part are stated below:

6.1.1 Sensitive analysis of meteorological conditions on the PV inverter components lifetime

- The most stressed components in the PV inverter are the dc-ac stage IGBT and dc-link capacitors. The dc-dc stage components present lower damage in comparison with the dc-ac stage ones. Therefore, their wear out process have almost no influence on the system lifetime prediction;

- The inverter IGBT are more sensitive to solar irradiance variations, while the dc-link capacitors are more impacted by the ambient temperature variations;

- The use of Ross' expression to calculate the PV module operating temperature is crucial to a more accurate lifetime prediction. Otherwise, the results may lead to an underestimated lifetime if the ambient temperature is considered as the module operating temperature;

- Modules thermal dynamics did not show significant influences in the lifetime prediction. Therefore, the negligence of this variable did not compromise the accuracy of the PV inverter lifetime.

6.1.2 Reliability of PV inverters with reactive power capability

- Multifunctional PV inverters with reactive power capability increases the components thermal loading, since more apparent power is processed;

- When the PV inverter is used to compensate reactive power with full capability of rated apparent power, the system lifetime is significantly reduced, for all three regions investigated;

- The inverter sizing ratio affects the PV modules generated energy and, consequently, the reactive power margin. For the investigated case studies, the PV inverters are expected to last longer in lower ISR conditions, even with more margin to compensate reactive power;

- Partial reactive power compensation can be an interesting reliability-oriented strategy to improve the multifunctional PV inverter lifetime and reduce the costs with inverter replacements. In this sense, the unreliability map is a very useful tool to address the most suitable conditions of the multifunctional PV inverter for a defined lifetime and unreliability target;

- The economic analysis based on LCOE showed that the extra energy generated by higher ISR conditions reduces the system costs. However,

every time that another inverter replacement is required in the system operating life, the costs increase. Additionally, the LCOE is higher when the multifunctional operation is considered. Therefore, there is an optimum solution in terms of ISR, reactive power capability and costs.

6.1.3   Lifetime evaluation applied to power factor regulation

- When the PV inverter is connected to the grid with a determined load on the PCC, it affects the power factor by reducing the liquid active power that flows to the grid;

- Multifunctional PV inverters can be used to provide reactive power to the load and regulate the power factor. This ancillary service can avoid extra costs with the use of another reactive power compensator (such as SVC or SC), or reduce its size, depending on the load energy consumption;

- For low load energy consumption, the multifunctional PV inverter can regulate the power factor. Additionally, depending on the size of the load, the PV inverter lifetime is not significantly impacted. However, as the load active power becomes closer to the PV inverter generation, there will be an amount of not compensated reactive power due to the dynamic saturation. Moreover, the lifetime of the PV inverter is more impacted, due to more reactive power being compensated;

- The partial reactive power strategy can be also used in the power factor regulation application. However, there is a trade-off involving the PV inverter lifetime and the amount of not compensated reactive power, reflecting on extra costs with another reactive power compensator or fees charged due to low PF operation.

6.2   Research perspectives

Although many aspects were studied and documented in this Ph.D thesis, there are still a lot of improvements which can be implemented.

From the author point of view, the following topics can be addressed in future researches:

- Application and reliability analysis of multifunctional PV inverters with reactive power capability applied to other case studies, such as voltage regulation and support during transient faults;

- Investigation of the lifetime evaluation of multifunctional PV inverters performing other ancillary services, such as harmonic current compensation and frequency regulation;

- Improvement on the reliability evaluation process, to include early failure and catastrophic random events rates;

- Experimental power losses validation and real temperature measurements to improve the reliability estimation accuracy;

- Development of a more complete economic analysis to include the costs with not compensated reactive power, that must be either charged due to low power factor operation or provided by another reactive power compensator;

- Proposal of economic incentives for multifunctional PV inverter owner while providing reactive power to improve grid power quality.

In view of these and many other possibilities of future works, the author really expected that this research project can be continued and not stop in the present Ph.D thesis.

References

ABNT. NBR 16149 - Sistemas fotovoltaicos (FV) - Características da interface de conexão com a rede elétrica de distribuição. *Associação Brasileira de Normas Técnicas*, 2013.

ABSOLAR. *O avanço da energia solar*. 2019. Disponível em: <http://www.absolar.org.br/>.

Agarwal, N.; Arya, A.; Ahmad, M. W.; Anand, S. Lifetime monitoring of electrolytic capacitor to maximize earnings from grid-feeding pv system. *IEEE Trans. on Ind. Electron.*, v. 63, n. 11, p. 7049–7058, Nov 2016.

AGREE. Reliability of military electronic equipment. In: *Report by Advisory Group on Reliability of Electronic Equipment*. [S.l.: s.n.], 1957.

Ahmad, M. W.; Agarwal, N.; Anand, S. Online monitoring technique for aluminum electrolytic capacitor in solar pv-based dc system. *IEEE Transactions on Industrial Electronics*, v. 63, n. 11, p. 7059–7066, Nov 2016.

Alonso García, M.; Balenzategui, J. Estimation of photovoltaic module yearly temperature and performance based on nominal operation cell temperature calculations. *Renewable Energy*, v. 29, n. 12, p. 1997–2010, 2004.

ANEEL. Resolução Normativa no 414. *Agência Nacional de Energia Elétrica*, 2010.

ANEEL. Nota Técnica n 0056/2017-SRD/ANEEL: Atualização das projeções de consumidores residenciais e comerciais com microgeração solar fotovoltaicos no horizonte 2017-2024. *Agência Nacional de Energia Elétrica*, 2017.

Anurag, A.; Yang, Y.; Blaabjerg, F. Thermal performance and reliability analysis of single-phase pv inverters with reactive power injection outside feed-in operating hours. *IEEE Journal of Emerg. and Sel. Topics in Power Electron.*, v. 3, n. 4, p. 870–880, Dec 2015.

Armstrong, S.; Hurley, W. A thermal model for photovoltaic panels under varying atmospheric conditions. *Applied Thermal Engineering*, v. 30, n. 11, p. 1488–1495, 2010.

ASTM. American Society for Testing and Materials. In: *Standard Practices for Cycle Counting in Fatigue Analysis*. [S.l.: s.n.], 2017.

Bao, X.; Zhuo, F.; Tian, Y.; Tan, P. Simplified feedback linearization control of three-phase photovoltaic inverter with an lcl filter. *IEEE Transactions on Power Electronics*, v. 28, n. 6, p. 2739–2752, 2013.

Barros, R. C.; Brito, E. M. S.; Boaventura, W. C.; Pereira, H. A.; Cupertino, A. F. Methodology for bondwire lifetime evaluation of multifunctional PV inverter during harmonic current compensation. *International Journal of Electrical Power & Energy Systems*, v. 128, p. 106711, 2021.

Bayerer, R.; Herrmann, T.; Licht, T.; Lutz, J.; Feller, M. Model for power cycling lifetime of igbt modules - various factors influencing lifetime. In: *5th International Conference on Integrated Power Electronics Systems*. [S.l.: s.n.], 2008. p. 1–6.

Bouguerra, S.; Yaiche, M. R.; Gassab, O.; Sangwongwanich, A.; Blaabjerg, F. The impact of pv panel positioning and degradation on the pv inverter lifetime and reliability. *IEEE Journal of Emerging and Selected Topics in Power Electronics*, p. 1–1, 2020.

Brown, R. W. Linking corrosion and catastrophic failure in low-power metallized polypropylene capacitors. *IEEE Transactions on Device and Materials Reliability*, v. 6, n. 2, p. 326–333, 2006.

Callegari, J.; Silva, M.; Barros, R. de; Brito, E.; Cupertino, A.; Pereira, H. Lifetime evaluation of three-phase multifunctional pv inverters with reactive power compensation. *Electric Power Systems Research*, v. 175, p. 105873, 2019.

Callegari, J. M. S. *Lifetime evaluation of three-phase multifunctional PV inverters with reactive power compensation*. 2018. Final paper (Undergraduate) - UFV (Universidade Federal de Viçosa, Viçosa, Brazil.

Callegari, J. M. S. *Minimum DC-link voltage control strategy for efficiency and reliability improvement in two-stage photovoltaic inverters*. Dissertação (Mestrado) — Centro Federal de Educação Tecnológica de Minas Gerais, Belo Horizonte, 2021.

Callegari, J. M. S.; Cupertino, A. F.; Ferreira, V. d. N.; Pereira, H. A. Minimum dc-link voltage control for efficiency and reliability improvement in pv inverters. *IEEE Transactions on Power Electronics*, v. 36, n. 5, p. 5512–5520, 2021.

CEMIG. *Campanha de tipologia - O comportamento da carga dos consumidores e do sistema elétrico da CEMIG*. [S.l.], 2012.

Choi, U.; Blaabjerg, F. Separation of wear-out failure modes of igbt modules in grid-connected inverter systems. *IEEE Transactions on Power Electronics*, v. 33, n. 7, p. 6217–6223, 2018.

Choi, U.; Blaabjerg, F.; Jørgensen, S. Power cycling test methods for reliability assessment of power device modules in respect to temperature stress. *IEEE Transactions on Power Electronics*, v. 33, n. 3, p. 2531–2551, 2018.

Choi, U.; Jørgensen, S.; Blaabjerg, F. Advanced accelerated power cycling test for reliability investigation of power device modules. *IEEE Transactions on Power Electronics*, v. 31, n. 12, p. 8371–8386, 2016.

Christen, D.; Stojadinovic, M.; Biela, J. Energy efficient heat sink design: Natural versus forced convection cooling. *IEEE Transactions on Power Electronics*, v. 32, n. 11, p. 8693–8704, 2017.

Chung, H. S. hung; Wang, H.; Blaabjerg, F.; Pecht, M. *Reliability of Power Electronic Converter Systems*. [S.l.]: The Institution of Engineering and Technology, 2015.

Chunlin, L.; Liu, J.; Zhang, Y.; Lei, W.; Cao, R.; Lv, G. Reliability modeling for metallized film capacitors based on time-varying stress mission profile and aging of esr. *IEEE Journal of Emerging and Selected Topics in Power Electronics*, p. 1–1, 2020.

Ciappa, M. Selected failure mechanisms of modern power modules. *Microelectronics Reliability*, v. 42, n. 4, p. 653 – 667, 2002.

Cui, H. Accelerated temperature cycle test and coffin-manson model for electronic packaging. In: *Annual Reliability and Maintainability Symposium, 2005. Proceedings.* [S.l.: s.n.], 2005. p. 556–560.

Cupertino, A. F. *Modeling, Design and Fault-Tolerant Strategies for Modular Multilevel Cascaded Converter-based STATCOMs*. Tese (Doutorado) — Universidade Federal de Minas Gerais, 2019.

CUPERTINO, A. F.; LENZ, J. M.; BRITO, E. M.; PEREIRA, H. A.; PINHEIRO, J. R.; SELEME, S. I. Impact of the mission profile length on lifetime prediction of pv inverters. *Microelectronics Reliability*, v. 100-101, p. 113427, 2019. 30th European Symposium on Reliability of Electron Devices, Failure Physics and Analysis.

Dagdelen, T.; Abdel-Rahman, E.; Yavuz, M. Reliability criteria for thick bonding wire. *Materials*, v. 11, n. 4, 2018.

Demirok, E.; González, P. C.; Frederiksen, K. H. B.; Sera, D.; Rodriguez, P.; Teodorescu, R. Local reactive power control methods for overvoltage prevention of distributed solar inverters in low-voltage grids. *IEEE Journal of Photovoltaics*, v. 1, n. 2, p. 174–182, 2011.

Denoix, T.; Sechilariu, M.; Locment, F. Experimental comparison of photovoltaic panel operating cell temperature models. In: *IECON 2014 - 40th Annual Conference of the IEEE Industrial Electronics Society*. [S.l.: s.n.], 2014. p. 2089–2095.

Dixon, J.; Moran, L.; Rodriguez, J.; Domke, R. Reactive power compensation technologies: State-of-the-art review. *Proceedings of the IEEE*, v. 93, n. 12, p. 2144–2164, 2005.

Drir, N.; Barazane, L.; Loudini, M. Comparative study of maximum power point tracking methods of photovoltaic systems. In: *2014 International Conference on Electrical Sciences and Technologies in Maghreb (CISTEM)*. [S.l.: s.n.], 2014. p. 1–5.

Drofenik, U.; Kolar, J. W. Teaching thermal design of power electronic systems with web-based interactive educational software. In: *Eighteenth Annual IEEE Applied Power Electronics Conference and Exposition, 2002. APEC '02*. [S.l.: s.n.], 2003. v. 2, p. 1029–1036 vol.2.

Edwards, P. R. Cumulative damage in fatigue with particular reference to the effects of residual stresses. In: *Royal Aircraft Establishment RAE*. [S.l.: s.n.], 1969.

Falck, J.; Felgemacher, C.; Rojko, A.; Liserre, M.; Zacharias, P. Reliability of power electronic systems: An industry perspective. *IEEE Industrial Electronics Magazine*, v. 12, n. 2, p. 24–35, June 2018.

FIDES. *FIDES-Reliability*. 2018. <https://www.fides-reliability.org/>.

Gandhi, O.; Rodríguez-Gallegos, C. D.; Gorla, N. B. Y.; Bieri, M.; Reindl, T.; Srinivasan, D. Reactive power cost from pv inverters considering inverter lifetime assessment. *IEEE Trans. on Sustainable Energy*, v. 10, n. 2, p. 738–747, April 2019.

Golestan, S.; Guerrero, J. M.; Vasquez, J. C. Three-phase plls: A review of recent advances. *IEEE Transactions on Power Electronics*, v. 32, n. 3, p. 1894–1907, 2017.

Gomes, C. C.; Cupertino, A. F.; Pereira, H. A. Damping techniques for grid-connected voltage source converters based on lcl filter: An overview. *Renewable and Sustainable Energy Reviews*, v. 81, p. 116–135, 2018.

GopiReddy, L. R.; Tolbert, L. M.; Ozpineci, B.; Pinto, J. O. P. Rainflow algorithm-based lifetime estimation of power semiconductors in utility applications. *IEEE Transactions on Industry Applications*, v. 51, n. 4, 7 2015.

Grgić, I.; Vukadinović, D.; Basić, M.; Bubalo, M. Calculation of semiconductor power losses of a three-phase quasi-z-source inverter. *Electronics*, v. 9, n. 10, 2020.

Gupta, A.; Yadav, O. P.; DeVoto, D.; Major, J. A Review of Degradation Behavior and Modeling of Capacitors. *ASME 2018 International Technical Conference and Exhibition on Packaging and Integration of Electronic and Photonic Microsystems*, 2018.

Gusman, L.; Pereira, H.; Callegari, J.; Cupertino, A. Design for reliability of multifunctional pv inverters used in industrial power factor regulation. *International Journal of Electrical Power & Energy Systems*, v. 119, p. 105932, 2020.

Guth, K.; Siepe, D.; Goerlich, J. R.; Torwesten, H.; Roth, R.; Hille, F.; Umbach, F. New assembly and interconnects beyond sintering methods. In: . [S.l.: s.n.], 2010.

Hartmann, S.; Bayer, M.; Schneider, D.; Feller, L. Observation of chip solder degradation by electrical measurements during power cycling. In: *2010 6th International Conference on Integrated Power Electronics Systems*. [S.l.: s.n.], 2010. p. 1–6.

Hava, A.; Kerkman, R.; Lipo, T. Simple analytical and graphical methods for carrier-based pwm-vsi drives. *IEEE Transactions on Power Electronics*, v. 14, n. 1, p. 49–61, 1999.

Hu, G. Comparison of copper, silver and gold wire bonding on interconnect metallization. In: *2012 13th International Conference on Electronic Packaging Technology High Density Packaging*. [S.l.: s.n.], 2012. p. 529–533.

Hu, Z.; Du, M.; Wei, K. Online calculation of the increase in thermal resistance caused by solder fatigue for igbt modules. *IEEE Transactions on Device and Materials Reliability*, v. 17, n. 4, p. 785–794, 2017.

Huang, H.; Mawby, P. A. A lifetime estimation technique for voltage source inverters. *IEEE Transactions on Power Electronics*, v. 28, n. 8, p. 4113–4119, 2013.

Hussin, M.; Omar, A.; Shaari, S.; Sin, N. M. Review of state-of-the-art: Inverter-to-array power ratio for thin - film sizing technique. *Renewable and Sustainable Energy Reviews*, v. 74, p. 265 – 277, 2017.

IEC 60747-34. *Semiconductor devices-Mechanical and climatic test methods-Part 34: Power cycling*. [S.l.], 2004.

IEC 60747-9. *Semiconductor devices-Discrete devices-Part 9: Insulated-gate bipolar transistors (IGBTs)*. [S.l.], 2019.

IEC 61709. *Electric Components - Reliability - Reference Conditions for Failure Rates and Stress Models for Conversion*. [S.l.], 2017.

IEC TR 62380. *Reliability Data Handbook-Universal Model for Reliability Prediction of Electronics Components, PCBs and Equipment*. [S.l.], 2006.

IEEE. Recommended practice on software reliability. *IEEE Std 1633-2016 (Revision of IEEE Std 1633-2008)*, p. 1–261, 2017.

IEEE. Standard for interconnection and interoperability of distributed energy resources with associated electric power systems interfaces. *IEEE Std 1547-2018 (Revision of IEEE Std 1547-2003)*, 2018.

Igbinovia, F. O.; Fandi, G.; ŠVEC, J.; Müller, Z.; Tlusty, J. Comparative review of reactive power compensation technologies. In: *2015 16th International Scientific Conference on Electric Power Engineering (EPE)*. [S.l.: s.n.], 2015. p. 2–7.

Infineon, T. IKQ75N120CT2. In: *Low Vce(sat) IGBT in TRENCHSTOP 2 technology copacked with soft, fast recovery full current rated anti-parallel Emitter Controlled Diode*. [S.l.: s.n.], 2019.

Jakhrani, A. Q.; Othman, A.; Rigit, A.; Samo, S. R. Comparison of solar photovoltaic module temperature models. In: . [S.l.: s.n.], 2011.

Jinko, S. JKM265P-60-A. In: *Poly crystalline module 245-265 Watt (Australian Market Use Only)*. [S.l.: s.n.], 2015.

Johnson, D.; Hartmann, S. ABB Power Transistors: Increasing lifespans of high-power electrical systems. *COMSOL Multiphysics*, v. 31, n. 10, p. 7171–7182, Oct 2015.

Kolar, J.; Wolbank, T.; Schrodl, M. Analytical calculation of the rms current stress on the dc link capacitor of voltage dc link pwm converter systems. In: *1999. Ninth International Conference on Electrical Machines and Drives (Conf. Publ. No. 468)*. [S.l.: s.n.], 1999. p. 81–89.

Kovačević, I. F.; Drofenik, U.; Kolar, J. W. New physical model for lifetime estimation of power modules. In: *The 2010 International Power Electronics Conference - ECCE ASIA -*. [S.l.: s.n.], 2010. p. 2106–2114.

Kray, T.; Markus, D. Peak wind loads on single-axis pv tracking systems. In: *15th International Conference on Wind Engineering*. [S.l.: s.n.], 2019.

Ku, T.; Lin, C.; Hsu, C.; Chen, C.; Liao, Z.; Wang, S.; Chen, F. Enhancement of power system operation by renewable ancillary service. *IEEE Transactions on Industry Applications*, p. 1–1, 2020.

Kyocera, S. Kd 300-80 f series. In: *High Efficiency Multicrystal Photovoltaic Module Datasheet*. [S.l.: s.n.], 2016.

Lazzaroni, M.; Cristaldi, L.; Peretto, L.; Rinaldi, P.; Catelani, M. *Reliability Engineering Basic Concepts and Applications in ICT*. [S.l.]: Springer, 2011.

Lenz, J. M.; Cupertino, A. F.; Pereira, H. A.; Zhou, D.; Wang, H.; Pinheiro, J. R. Benchmarking of capacitor power loss calculation methods for wear-out failure prediction in pv inverters. *Microelectronics Reliability*, v. 100-101, p. 113491, 2019. 30th European Symposium on Reliability of Electron Devices, Failure Physics and Analysis.

Liserre, M.; Blaabjerg, F.; Hansen, S. Design and control of an lcl-filter-based three-phase active rectifier. *IEEE Transactions on Industry Applications*, v. 41, n. 5, p. 1281–1291, 2005.

Liu, D.; Sampson, M. J. Some aspects of the failure mechanisms in batio3-based multilayer ceramic capacitors. In: . [S.l.: s.n.], 2012.

Lledó-Ponsati, T.; Bahman, A. S.; Iannuzzo, F.; Montesinos-Miracle, D.; Arellano, S. G. Reliability analysis of a 3-leg 4-wire inverter under unbalanced loads and harmonic injection. In: *2019 20th Workshop on Control and Modeling for Power Electronics (COMPEL)*. [S.l.: s.n.], 2019. p. 1–8.

Lobera, D. T.; Valkealahti, S. Dynamic thermal model of solar pv systems under varying climatic conditions. *Solar Energy*, v. 93, p. 183 – 194, 2013.

Lopez-Garcia, J.; Pavanello, D.; Sample, T. Analysis of temperature coefficients of bifacial crystalline silicon pv modules. *IEEE Journal of Photovoltaics*, v. 8, n. 4, p. 960–968, 2018.

Lutz, J.; Schwabe, C.; Zeng, G.; Hein, L. Validity of power cycling lifetime models for modules and extension to low temperature swings. In: *2020 22nd European Conference on Power Electronics and Applications (EPE'20 ECCE Europe)*. [S.l.: s.n.], 2020. p. P.1–P.9.

Ma, K.; Blaabjerg, F. Reliability-cost models for the power switching devices of wind power converters. In: *2012 3rd IEEE International Symposium on Power Electronics for Distributed Generation Systems (PEDG)*. [S.l.: s.n.], 2012. p. 820–827.

Ma, K.; Liserre, M.; Blaabjerg, F.; Kerekes, T. Thermal loading and lifetime estimation for power device considering mission profiles in wind power converter. *IEEE Trans. on Power Electron.*, v. 30, n. 2, p. 590–602, Feb 2015.

Ma, K.; Wang, H.; Blaabjerg, F. New approaches to reliability assessment: Using physics-of-failure for prediction and design in power electronics systems. *IEEE Power Electronics Magazine*, v. 3, n. 4, p. 28–41, Dec 2016.

Mainka, K.; Thoben, M.; Schilling, O. Lifetime calculation for power modules, application and theory of models and counting methods. In: *Proceedings of the 2011 14th European Conference on Power Electronics and Applications*. [S.l.: s.n.], 2011. p. 1–8.

Mantilla, M. A.; Petit, J. F.; Ordóñez, G. Control of multi-functional grid-connected pv systems with load compensation under distorted and unbalanced grid voltages. *Electric Power Systems Research*, v. 192, p. 106918, 2021.

Martin, C. Procedure and data for estimating reliability and maintainability. In: *Report No M-M-P-59-21*. [S.l.: s.n.], 1959.

Matsukawa, H.; Kurokawa, K. Temperature fluctuation analysis of photovoltaic modules at short time interval. In: *IEEE PV Spec. Conf.* [S.l.: s.n.], 2005. p. 1816–1819.

Menzi, D.; Heller, M.; Kolar, J. W. iGSE-Cx - a new normalized steinmetz model for class ii multilayer ceramic capacitors. *IEEE Open Journal of Power Electronics*, v. 2, p. 138–144, 2021.

Military Handbook. *Reliability prediction of electronic equipment, MILHDBK-217A*. Washington, DC, 1965.

Military Handbook. *Reliability prediction of electronic equipment, MILHDBK-217F*. Washington, DC, 1991.

Military Handbook. *Reliability prediction of electronic equipment, MILHDBK-217F Notice 2*. Washington, DC, 1995.

Miner, A. M. Cumulative damage in fatigue. *Journal of Applied Mechanics*, v. 67, p. A159–A164, 1945.

Minford, W. Accelerated life testing and reliability of high k multilayer ceramic capacitors. *IEEE Transactions on Components, Hybrids, and Manufacturing Technology*, v. 5, n. 3, p. 297–300, 1982.

MINTS, P. *SPV Market Research: The Solar Flare*. 2020. Disponível em: <http://www.spvmarketresearch.com/>.

Mondol, J. D.; Yohanis, Y. G.; Norton, B. Optimal sizing of array and inverter for grid-connected photovoltaic systems. *Solar Energy*, v. 80, n. 12, p. 1517 – 1539, 2006.

Moore, L. M.; Post, H. N. Five years of operating experience at a large utility-scale photovoltaic generating plant. *Progress Photovolt., Res. Appl.*, v. 16, p. 249–259, 2008.

Moradi-Shahrbabak, Z.; Tabesh, A.; Yousefi, G. R. Economical design of utility-scale photovoltaic power plants with optimum availability. *IEEE Transactions on Industrial Electronics*, v. 61, n. 7, p. 3399–3406, 2014.

Morozumi, A.; Yamada, K.; Miyasaka, T.; Seki, Y. Reliability of power cycling for igbt power semiconductor modules. In: *Conference Record of the 2001 IEEE Industry Applications Conference. 36th IAS Annual Meeting (Cat. No.01CH37248)*. [S.l.: s.n.], 2001. v. 3, p. 1912–1918 vol.3.

Musallam, M.; Yin, C.; Bailey, C.; Johnson, M. Mission profile-based reliability design and real-time life consumption estimation in power electronics. *IEEE Trans. on Power Electronics*, v. 30, n. 5, p. 2601–2613, May 2015.

Norris, K. C.; Landzberg, A. H. Reliability of controlled collapse interconnections. *IBM Journal of Research and Development*, v. 13, n. 3, p. 266–271, 1969.

Notton, G.; Lazarov, V.; Stoyanov, L. Optimal sizing of a grid-connected pv system for various pv module technologies and inclinations, inverter efficiency characteristics and locations. *Renewable Energy*, v. 35, n. 2, p. 541 – 554, 2010.

O'Connor, P.; Kleyner, A. *Practical Reliability Engineering*. [S.l.]: Wiley-Blackwell, 2012.

Olukan, T. A.; Emziane, M. A comparative analysis of pv module temperature models. *Energy Procedia*, v. 62, p. 694 – 703, 2014. 6th International Conference on Sustainability in Energy and Buildings, SEB-14.

Osma-Pinto, G.; Ordóñez-Plata, G. Dynamic thermal modelling for the prediction of the operating temperature of a pv panel with an integrated cooling system. *Renewable Energy*, v. 152, p. 1041–1054, 2020.

Palmgren, A. Die lebensdauer von kugellagern. *Zeitschrift des Vereines Deutscher Ingenieure*, v. 14, p. 339–341, 1924.

Pan, Y.; Sangwongwanich, A.; Yang, Y.; Blaabjerg, F. A phase-shifting MPPT method to mitigate interharmonics from cascaded h-bridge pv inverters. In: *2020 IEEE Applied Power Electronics Conference and Exposition (APEC)*. [S.l.: s.n.], 2020. p. 157–163.

Pecht, M.; Dasgupta, A. Physics-of-failure: an approach to reliable product development. In: *IEEE 1995 International Integrated Reliability Workshop. Final Report*. [S.l.: s.n.], 1995. p. 1–4.

Pecht, M. G.; Nash, F. R. Predicting the reliability of electronic equipment. *Proceedings of the IEEE*, v. 82, n. 7, p. 992–1004, 1994.

Pedersen, K. B.; Pedersen, K. Bond wire lift-off in igbt modules due to thermomechanical induced stress. In: *2012 3rd IEEE International Symposium on Power Electronics for Distributed Generation Systems (PEDG)*. [S.l.: s.n.], 2012. p. 519–526.

Pérez-Higueras, P. J.; Almonacid, F. M.; Rodrigo, P. M.; Fernández, E. F. Optimum sizing of the inverter for maximizing the energy yield in state-of-the-art high-concentrator photovoltaic systems. *Solar Energy*, v. 171, p. 728 – 739, 2018.

Peyghami, S.; Wang, Z.; Blaabjerg, F. A guideline for reliability prediction in power electronic converters. *IEEE Transactions on Power Electronics*, p. 1–1, 2020.

PHBSolar. PHB1500-SS. In: *Inversor Solar Fotovoltaico certificado pelo INMETRO*. [S.l.: s.n.], 2015.

Pinto, A.; Zilles, R. Reactive power excess charging in grid-connected pv systems in brazil. *Renewable Energy*, v. 62, p. 47 – 52, 2014.

Ramminger, S.; Türkes, P.; Wachutka, G. Crack mechanism in wire bonding joints. *Microelectronics Reliability*, v. 38, n. 6, p. 1301 – 1305, 1998. Reliability of Electron Devices, Failure Physics and Analysis.

Rashed, A.; Forest, F.; Huselstein, J. .; Martiré, T.; Enrici, P. On-line [tj, vce] monitoring of igbts stressed by fast power cycling tests. In: *2013 15th European Conference on Power Electronics and Applications (EPE)*. [S.l.: s.n.], 2013. p. 1–9.

Reigosa, P. D.; Wang, H.; Yang, Y.; Blaabjerg, F. Prediction of bond wire fatigue of igbts in a pv inverter under a long-term operation. *IEEE Trans. on Power Electron.*, v. 31, n. 10, p. 7171–7182, Oct 2016.

REN21. *Renewables 2020: Global Status Report*. 2020. Disponível em: <http://www.ren21.net/reports/global-status-report/>.

Ross, R. Semiconductor performance in terms of distributions, bath tub curves and similarity index. In: *2018 15th China International Forum on Solid State Lighting: International Forum on Wide Bandgap Semiconductors China (SSLChina: IFWS)*. [S.l.: s.n.], 2018. p. 1–5.

Ross, R. G.; Smokler, M. I. Flat-plate solar array project: Final report: Volume 6. *Engineering sciences and reliability, Report DOE/JPL-I012–125*, v. 6, 1986.

Sahu, P. K.; Mohanty, A.; Ganthia, B. P.; Panda, A. K. A multiphase interleaved boost converter for grid-connected pv system. In: *2016 International Conference on Microelectronics, Computing and Communications (MicroCom)*. [S.l.: s.n.], 2016. p. 1–6.

SANDIA. DOE/EPRI electricity storage handbook in collaboration with nreca. In: *National Laboratories*. [S.l.: s.n.], 2015.

Sangwongwanich, A.; Yang, Y.; Sera, D.; Blaabjerg, F. Lifetime evaluation of grid-connected pv inverters considering panel degradation rates and installation sites. *IEEE Trans. on Power Elec.*, v. 33, n. 2, p. 1225–1236, Feb 2018.

Sangwongwanich, A.; Yang, Y.; Sera, D.; Blaabjerg, F.; Zhou, D. On the impacts of pv array sizing on the inverter reliability and lifetime. *IEEE Trans. on Ind. App.*, v. 54, n. 4, p. 3656–3667, July 2018.

Sangwongwanich, A.; Yang, Y.; Sera, D.; Blaabjerg, F. Mission profile-oriented control for reliability and lifetime of photovoltaic inverters. *IEEE Transactions on Industry Applications*, v. 56, n. 1, p. 601–610, 2020.

Sarkar, M. N. I.; Meegahapola, L. G.; Datta, M. Reactive power management in renewable rich power grids: A review of grid-codes, renewable generators, support devices, control strategies and optimization algorithms. *IEEE Access*, v. 6, p. 41458–41489, 2018.

Scheuermann, U.; Beckedahl, P. The road to the next generation power module - 100 % solder free design. In: *5th International Conference on Integrated Power Electronics Systems*. [S.l.: s.n.], 2008. p. 1–10.

Scheuermann, U.; Schmidt, R.; Newman, P. Power cycling testing with different load pulse durations. In: *7th IET International Conference on Power Electronics, Machines and Drives (PEMD 2014)*. [S.l.: s.n.], 2014. p. 1–6.

Schilling, O.; Schäfer, M.; Mainka, K.; Thoben, M.; Sauerland, F. Power cycling testing and fe modelling focussed on al wire bond fatigue in high power igbt modules. *Microelectronics Reliability*, v. 52, n. 9, p. 2347 – 2352, 2012. Special Issue 23rd European Symposium on the Reliability of Electron Devices, Failure Physics and Analysis.

Schmidt, R.; Zeyss, F.; Scheuermann, U. Impact of absolute junction temperature on power cycling lifetime. In: *2013 15th European Conference on Power Electronics and Applications (EPE)*. [S.l.: s.n.], 2013. p. 1–10.

Schwingshackl, C.; Petitta, M.; Wagner, J.; Belluardo, G.; Moser, D.; Castelli, M.; Zebisch, M.; Tetzlaff, A. Wind effect on pv module temperature: Analysis of different techniques for an accurate estimation. *Energy Procedia*,

v. 40, p. 77–86, 2013. European Geosciences Union General Assembly 2013, EGUDivision Energy, Resources & the Environment, ERE.

Sera, D.; Mathe, L.; Kerekes, T.; Spataru, S. V.; Teodorescu, R. On the perturb-and-observe and incremental conductance mppt methods for pv systems. *IEEE Journal of Photovoltaics*, v. 3, n. 3, p. 1070–1078, July 2013.

Shao, J.; Lu, F.; Zeng, C.; Xu, M. The principle and application of physics-of-failure based reliability technology. In: *Prog. and Sys. Health Man. Conf. (PHM Hunan)*. [S.l.: s.n.], 2014. p. 75–78.

Shen, Y.; Chub, A.; Wang, H.; Vinnikov, D.; Liivik, E.; Blaabjerg, F. Wear-out failure analysis of an impedance-source pv microinverter based on system-level electrothermal modeling. *IEEE Transactions on Industrial Electronics*, v. 66, n. 5, p. 3914–3927, May 2019.

Silva, E. L.; Lima, A. M. N.; Corrêa, M. B. R.; Vitorino, M. A.; Barbosa, L. A new centralized active and reactive power control strategy for voltage regulation in power distribution networks with high penetration of photovoltaic generation. In: *2016 17th International Conference on Harmonics and Quality of Power (ICHQP)*. [S.l.: s.n.], 2016. p. 823–828.

Silva, R.; Barros, R.; Brito, E.; Boaventura, W.; Cupertino, A.; Pereira, H. Pursuing computationally efficient wear-out prediction of pv inverters: The role of the mission profile resolution. *Microelectronics Reliability*, v. 110, p. 113679, 2020.

Sintamarean, N.; Blaabjerg, F.; Wang, H.; Iannuzzo, F.; de Place Rimmen, P. Reliability oriented design tool for the new generation of grid connected pv-inverters. *IEEE Trans. on Power Electronics*, v. 30, n. 5, p. 2635–2644, May 2015.

Sommer, J.; Licht, T.; Berg, H.; Appelhoff, K.; Michel, B. Solder fatigue at high-power igbt modules. In: *4th International Conference on Integrated Power Systems*. [S.l.: s.n.], 2006. p. 1–6.

Song, Y.; Wang, B. Survey on reliability of power electronic systems. *IEEE Transactions on Power Electronics*, v. 28, n. 1, p. 591–604, 2013.

Sousa, C. V. de. *Projeto de uma Bancada de Testes para Avaliação do Carregamento de Transformadores Trifásicos de Potência Utilizando Conversores Estáticos*. Dissertação (Mestrado) — Universidade Federal de Minas Gerais, 2007.

Souza, M. A. d.; Souza, J. P. d.; Pereima, A. T. Simplified Methodology for Temperature Calculation of Operation and Photovoltaic Modules Yield in Non-Standardized Environmental Conditions. *Brazilian Archives of Biology and Technology*, scielo, v. 61, 00 2018.

Sreechithra, S. M.; Jirutitijaroen, P.; Rathore, A. K. Impacts of reactive power injections on thermal performances of pv inverters. In: *IECON 2013 - 39th Annual Conference of the IEEE Industrial Electronics Society*. [S.l.: s.n.], 2013. p. 7175–7180.

Steinhorst, P.; Poller, T.; Lutz, J. Approach of a physically based lifetime model for solder layers in power modules. *Microelectronics Reliability*, v. 53, n. 9, p. 1199 – 1202, 2013. European Symposium on Reliability of Electron Devices, Failure Physics and Analysis.

Sun, Q.; Tang, Y.; Feng, J.; Jin, T. Reliability assessment of metallized film capacitors using reduced degradation test sample. *Quality and Reliability Engineering International*, v. 29, n. 2, p. 259–265, 2013.

Syed, A. Limitations of norris-landzberg equation and application of damage accumulation based methodology for estimating acceleration factors for pb free solders. In: *2010 11th International Thermal, Mechanical Multi-Physics Simulation, and Experiments in Microelectronics and Microsystems (EuroSimE)*. [S.l.: s.n.], 2010. p. 1–11.

Takao, K.; Kyogoku, S. Ultra low inductance power module for fast switching sic power devices. In: *2015 IEEE 27th International Symposium on Power Semiconductor Devices IC's (ISPSD)*. [S.l.: s.n.], 2015. p. 313–316.

Tanaka, T. *Control and Optimization of Modular Multilevel Cascaded Statcom Converters for Offshore Wind Application*. Tese (Doutorado) — Aalborg University, Denmark, 2018.

TDK. B43630. In: *Aluminum snap-in electrolytic capacitors*. [S.l.: s.n.], 2016.

TDK. General technical information. In: *Aluminum electrolytic capacitors*. [S.l.: s.n.], 2019.

Teodorescu, R.; Liserre, M.; Rodríguez, P. *Grid converters for photovoltaic and wind power systems*. [S.l.]: John Willey & Sons, Ltd, 2011.

Tina, G. M.; Abate, R. Experimental verification of thermal behaviour of photovoltaic modules. In: *IEEE Med. Elec. Conf. (MELECON)*. [S.l.: s.n.], 2008. p. 579–584.

Trina, S. Tallmax TSM-DE15M(II). In: *High efficient mono-PERC half-cut 144 cells datasheet*. [S.l.: s.n.], 2020.

Tseng, H.; Wu, M. Electro-thermal-mechanical modeling of wire bonding failures in igbt. In: *2013 8th International Microsystems, Packaging, Assembly and Circuits Technology Conference (IMPACT)*. [S.l.: s.n.], 2013. p. 152–157.

Väisänen, J.; Kosonen, A.; Ahola, J.; Sallinen, T.; Hannula, T. Optimal sizing ratio of a solar pv inverter for minimizing the levelized cost of electricity in finnish irradiation conditions. *Solar Energy*, v. 185, p. 350 – 362, 2019.

Wakefield-Vette. 510, 511 & 512 series. In: *Extruded heat sinks for power semiconductors*. [S.l.: s.n.], 2007.

Wang, H.; Blaabjerg, F. Reliability of capacitors for dc-link applications in power electronic converters - an overview. *IEEE Trans. on Ind. App.*, v. 50, n. 5, p. 3569–3578, Sep. 2014.

Wang, H.; Blaabjerg, F.; Ma, K.; Wu, R. Design for reliability in power electronics in renewable energy systems - status and future. In: *4th International Conference on Power Engineering, Energy and Electrical Drives*. [S.l.: s.n.], 2013. p. 1846–1851.

Wang, H.; Davari, P.; Wang, H.; Kumar, D.; Zare, F.; Blaabjerg, F. Lifetime estimation of dc-link capacitors in adjustable speed drives under grid voltage unbalances. *IEEE Transactions on Power Electronics*, v. 34, n. 5, p. 4064–4078, 2019.

Wang, H.; Li, C.; Zhu, G.; Liu, Y.; Wang, H. Model-based design and optimization of hybrid dc-link capacitor banks. *IEEE Transactions on Power Electronics*, v. 35, n. 9, p. 8910–8925, 2020.

Wang, H.; Liserre, M.; Blaabjerg, F.; de Place Rimmen, P.; Jacobsen, J. B.; Kvisgaard, T.; Landkildehus, J. Transitioning to physics-of-failure as a reliability driver in power electronics. *IEEE Journal of Emerging and Selected Topics in Power Electronics*, v. 2, n. 1, p. 97–114, March 2014.

Wang, H.; Ma, K.; Blaabjerg, F. Design for reliability of power electronic systems. In: *IECON 2012 - 38th Annual Conference on IEEE Industrial Electronics Society*. [S.l.: s.n.], 2012. p. 33–44.

Wang, H.; Muñoz-García, M.; Moreda, G.; Alonso-García, M. Optimum inverter sizing of grid-connected photovoltaic systems based on energetic and economic considerations. *Renewable Energy*, v. 118, p. 709 – 717, 2018.

Wang, H.; Wang, H.; Zhu, G.; Blaabjerg, F. Cost assessment of three power decoupling methods in a single-phase power converter with a reliability-oriented design procedure. In: *2016 IEEE 8th International Power Electronics and Motion Control Conference (IPEMC-ECCE Asia)*. [S.l.: s.n.], 2016. p. 3818–3825.

Wang, H.; Zhou, D.; Blaabjerg, F. A reliability-oriented design method for power electronic converters. In: *2013 Twenty-Eighth Annual IEEE Applied Power Electronics Conference and Exposition (APEC)*. [S.l.: s.n.], 2013. p. 2921–2928.

Wang, M.; Zhang, X.; Zhao, T.; Ma, M.; Hu, Y.; Wang, F.; Wang, X. Harmonic compensation strategy for single-phase cascaded h-bridge pv inverter under unbalanced power conditions. *IEEE Transactions on Industrial Electronics*, v. 67, n. 12, p. 10474–10484, 2020.

Weckx, S.; Gonzalez, C.; Driesen, J. Combined central and local active and reactive power control of pv inverters. *IEEE Trans. Sustain. Energy*, v. 5, n. 3, p. 776–784, July 2014.

White, M.; Bernstein, J. B. *Microelectronics reliability: physics-of-failure based modeling and life evaluation*. Pasadena, CA, 2008.

Wu, R.; Blaabjerg, F.; Wang, H.; Liserre, M.; Iannuzzo, F. Catastrophic failure and fault-tolerant design of igbt power electronic converters - an overview. In: *IECON 2013 - 39th Annual Conference of the IEEE Industrial Electronics Society*. [S.l.: s.n.], 2013. p. 507–513.

Xavier, L. S. *Harmonic Current Compensation Applied to Single-Phase Photovoltaic Systems*. Dissertação (Mestrado) — Universidade Federal de Minas Gerais, 2018.

Xavier, L. S.; Cupertino, A. F.; Pereira, H. A. Adaptive saturation scheme for a multifunctional single-phase photovoltaic inverter. In: *2014 11th IEEE/IAS International Conference on Industry Applications*. [S.l.: s.n.], 2014. p. 1–8.

Xavier, L. S.; Cupertino, A. F.; Pereira, H. A.; Mendes, V. F. Partial harmonic current compensation for multifunctional photovoltaic inverters. *IEEE Trans. Power Syst.*, v. 34, n. 12, p. 11868–11879, Dec 2019.

Xue, S.; Zhou, Q.; Li, J.; Xiang, C.; Chen, S. Reliability evaluation for the dc-link capacitor considering mission profiles in wind power converter. In: *2016 IEEE International Conference on High Voltage Engineering and Application (ICHVE)*. [S.l.: s.n.], 2016. p. 1–4.

Yang, D.; Wang, X.; Liu, F.; Xin, K.; Liu, Y.; Blaabjerg, F. Adaptive reactive power control of pv power plants for improved power transfer capability under ultra-weak grid conditions. *IEEE Transactions on Smart Grid*, v. 10, n. 2, p. 1269–1279, 2019.

Yang, L.; Agyakwa, P. A.; Johnson, C. M. Physics-of-failure lifetime prediction models for wire bond interconnects in power electronic modules. *IEEE Transactions on Device and Materials Reliability*, v. 13, n. 1, p. 9–17, 2013.

Yang, S.; Bryant, A.; Mawby, P.; Xiang, D.; Ran, L.; Tavner, P. An industry-based survey of reliability in power electronic converters. *IEEE Trans. on Industry Applications*, v. 47, n. 3, p. 1441–1451, May 2011.

Yang, Y.; Enjeti, P.; Blaabjerg, F.; Wang, H. Suggested grid code modifications to ensure wide-scale adoption of photovoltaic energy in distributed power generation systems. In: *2013 IEEE Industry Applications Society Annual Meeting.* [S.l.: s.n.], 2013. p. 1–8.

Yang, Y.; Ma, K.; Wang, H.; Blaabjerg, F. Instantaneous thermal modeling of the dc-link capacitor in photovoltaic systems. In: *2015 IEEE Applied Power Electronics Conference and Exposition (APEC).* [S.l.: s.n.], 2015. p. 2733–2739.

Yang, Y.; Sangwongwanich, A.; Blaabjerg, F. Design for reliability of power electronics for grid-connected photovoltaic systems. *CPSS Transactions on Power Electronics and Applications*, v. 1, n. 1, p. 92–103, Dec 2016.

Yang, Y.; Sularea, V.; Ma, K.; Blaabjerg, F. Advanced design tools for the reliability of power electronics - case studies on a photovoltaic (pv) system. In: *IECON 2015.* [S.l.: s.n.], 2015. p. 002828–002833.

Yang, Y.; Wang, H.; Blaabjerg, F. Reactive power injection strategies for single-phase photovoltaic systems considering grid requirements. *IEEE Trans. Ind Appl.*, v. 50, n. 6, p. 4065–4076, 2014.

Yu, H.; Pan, J.; Xiang, A. A multi-function grid-connected PV system with reactive power compensation for the grid. *Solar Energy*, v. 79, n. 1, p. 101 – 106, 2005.

Zaini, N. H.; Kadir, M. Z. A.; Izadi, M.; Ahmad, N. I.; Radzi, M. A. M.; Azis, N. The effect of temperature on a mono-crystalline solar pv panel. In: *IEEE Conf. on Energy Conv. (CENCON).* [S.l.: s.n.], 2015. p. 249–253.

Zeng, G.; Alvarez, R.; Künzel, C.; Lutz, J. Power cycling results of high power igbt modules close to 50 hz heating process. In: *2019 21st European Conference on Power Electronics and Applications (EPE '19 ECCE Europe)*. [S.l.: s.n.], 2019. p. 1–10.

Zeng, G.; Borucki, L.; Wenzel, O.; Schilling, O.; Lutz, J. First results of development of a lifetime model for transfer molded discrete power devices. In: *PCIM Europe 2018; International Exhibition and Conference for Power Electronics, Intelligent Motion, Renewable Energy and Energy Management*. [S.l.: s.n.], 2018. p. 1–8.

Zeng, G.; Borucki, L.; Wenzel, O.; Schilling, O.; Lutz, J. First results of development of a lifetime model for transfer molded discrete power devices. In: *PCIM Europe 2018; International Exhibition and Conference for Power Electronics, Intelligent Motion, Renewable Energy and Energy Management*. [S.l.: s.n.], 2018. p. 1–8.

Zeng, G.; Herold, C.; Methfessel, T.; Schäfer, M.; Schilling, O.; Lutz, J. Experimental investigation of linear cumulative damage theory with power cycling test. *IEEE Transactions on Power Electronics*, v. 34, n. 5, p. 4722–4728, 2019.

Zhang, J.; Fu, X.; Lin, J.; Liu, Z.; Liu, N.; Wu, B. Study on damage accumulation and life prediction with loads below fatigue limit based on a modified nonlinear model. *Materials*, v. 11, n. 11, 2018.

Zhang, J.; Wang, H.; Cai, X.; Igarashi, S.; Li, Y.; Wang, Z. Thermal control method based on reactive circulating current for anti-condensation of wind power converter under wind speed variations. In: *2014 International Power Electronics and Application Conference and Exposition*. [S.l.: s.n.], 2014. p. 152–156.

Zhou, D.; Wang, H.; Blaabjerg, F. Reactive power impacts on lcl filter capacitor lifetime in grid-connected inverter. *IEEE Open Journal of Power Electronics*, v. 1, p. 139–148, 2020.

Zhu, S.-P.; Hao, Y.-Z.; Correia, J. A. de O.; Lesiuk, G.; Jesus, A. M. de. Nonlinear fatigue damage accumulation and life prediction of metals: A comparative study. *Fatigue & Fracture of Engineering Materials & Structures*, v. 42, n. 6, p. 1271–1282, 2019.

Zou, Z.; Wang, Z.; Cheng, M. Modeling, analysis, and design of multifunction grid-interfaced inverters with output lcl filter. *IEEE Transactions on Power Electronics*, v. 29, n. 7, p. 3830–3839, 2014.

Biography

Erick Matheus da Silveira Brito was born in Feira de Santana - BA, Brazil in 1990. He received his B.S. degree in Electrical Engineering from Federal University of Viçosa (UFV) in 2014 and the M.S. degree in Agricultural Engineering from the same institution in 2016. Since 2019 he has been with the Institute of Exact and Technological Sciences at Federal University of Viçosa - Florestal, teaching classes of Electric Machines and Industrial Automation for technical courses in Electronics and Electrotechnics. Currently, he is part of the Gerência de Especialistas em Sistemas Elétricos de Potência, working as a senior researcher. His main research interest include renewable power generation, multifunctional photovoltaic inverters, reliability of electronic converters and power quality.

E-mail: erick.brito@ufv.br

Webiste: http://www.gesep.ufv.br/

Research Gate: http://www.researchgate.net/profile/Erick-Brito

ORCID: https://orcid.org/0000-0001-8208-9173